Winter 12-15-2016

The Dynamic Brain in Action: Cortical Oscillations and Coordination Dynamics

Mahmood Hoseini
Washington University in St. Louis

WASHINGTON UNIVERSITY IN ST. LOUIS

Department of Physics

Dissertation Examination Committee:
Ralf Wessel, Chair
Sonya Bahar
Anders Carlson
Zohar Nussinov
Woodrow Shew
Larry Snyder

The Dynamic Brain in Action: Cortical Oscillations and Coordination Dynamics

by

Mahmood Hoseini

A dissertation presented to
The Graduate School
of Washington University in
partial fulfillment of the
requirements for the degree
of Doctor of Philosophy

December 2016
Saint Louis, Missouri

Contents

List of Figures

List of Tables

Acknowledgments

My sincerest thanks goes to my advisor Prof. Ralf Wessel for all of his support during my PhD study. I am so grateful for his exemplary patience, consideration and for all the efforts he put in my training during these years.

My special thanks goes to Prof. Anders Carlson for serving as one of my annual committee members, and more importantly, for all of his valuable advice and comments during these years.

I would also like to thank my defense committee members, Prof. Sonya Bahar, Prof. Zohar Nussinov, and Prof. Woodrow Shew for serving as my committee members, and also for their comments on the preliminary version of this thesis. Their comments were very helpful in editing the thesis.

Finally, I thank my fellow labmates for all the discussions and feedbacks, and also for all the fun we have had during these years.

Mahmood Hoseini

Washington University in Saint Louis

December 2016

I would like to begin by thanking my family. Their unconditional support is largely the reason that this PhD is completed in the United States. No words are sufficient to describe my parents' contribution to my life.

I am particularly grateful to my fiancee for always supporting me. Her encouragement has been instrumental in my overcoming several hurdles in life. I am indeed blessed to have her in my life.

ABSTRACT OF THE DISSERTATION

The Dynamic Brain in Action: Cortical Oscillations and Coordination Dynamics

by

Mahmood Hoseini

Doctor of Philosophy in Physics

Washington University in St. Louis, 2016

Professor Ralf Wessel, Chair

Cortical oscillations are electrical activities with rhythmic and/or repetitive nature generated spontaneously and in response to stimuli. Study of cortical oscillations has become an area of converging interests since the last two decades and has deepened our understanding of its physiological basis across different behavioral states. Experimental and modeling work has taught us that there is a wide diversity of cellular and circuit mechanisms underlying the generation of cortical rhythms. A wildly diverse set of functions has pertained to synchronous oscillations but their significance in cognition should be better appraised in the more general framework of correlation between spike times of neurons. Oscillations are the core mechanism in adjusting neuronal interactions and shaping temporal coordination of neural activity.

In the first part of this thesis, we reviewed essential features of cortical oscillations in membrane potentials and local field potentials recorded from turtle *ex vivo* preparation. Then we developed a simple computational model that reproduces the observed features.

The modeling investigation suggests a plausible underlying mechanism for rhythmogenesis through cellular and circuit properties. The second part of the thesis is on temporal coordination dynamics quantified by ”signal” and ”noise” correlations. Here we presented another computational model to show how temporal coordination and synchronous oscillations can be sewn together. More importantly, identifying the biophysical ingredients that are necessary for a network to reproduce the observed coordination dynamics.

Preface

Cortical oscillations are neuronal activities spontaneous or evoked by stimulus with a rhythmic structure. They were discovered by Hans Berger using first recorded electroencephalogram about 150 years ago. Later on, oscillations were observed throughout different regions of the brain at all spatial resolutions, from single-cell membrane potentials to large-scale neural traces. The recent resurgence of interest in cortical oscillations is a result of our progress in generating them under controlled situations, rather than just monitoring, and invasive and noninvasive studies under physiological and pathological conditions suggested that neural oscillations implement cognitive processes such as sensory representations, attentional selection, and dynamical routing/gating of information. Although much is known about rhythmogenesis mechanisms in archicortex and entrohinal cortex, little evidence is available to suggest a rhythmogenesis mechanism for cortical oscillations. What is known is that specific type of neurons within the cortex are capable of firing tonic spikes and, in addition, interaction of inhibitory neurons with each other or with excitatory neurons cause oscillations to appear. However, it is not obvious how do oscillations change with changes in microcircuit architecture, or to what extent individual neuronal properties impact oscillatory activity.

One functional implication of oscillations is that they may impact neuronal spike times through affecting their synaptic inputs, however, remained to be uncover is the detail of this influence. This question is particularly difficult because of the immense recurrent

connections in the network. Interconnections suggest that neural activity is coordinated across multiple spatial and temporal scales. Moreover, the strength of coordination depends on other factors such as activity level, network state, and so on. Addressing neural coordination is important since it has implications for cortical function; in one hand weak coordination corresponds to a larger degree of freedom while, on the other hand, stronger coordination supports signal propagation. These competing factors set up coordination magnitude in active cortical circuits. Much effort has been into determining coordination level in different preparation using various signal especially recorded spike trains, but little is known about the mechanisms that are responsible for the realized level of cortical coordination and its dynamics. In this draft we try to address these questions especially the one regarding underlying mechanisms.

In the first chapter of this thesis, we attempt to provide a quick introduction to the concept of oscillations, and discuss some major works that have been performed in this area of inquiry. We introduce different frequency bands along with their functional implications, then we review properties of single neurons that influence the emergence of oscillations. Moreover, basic synaptic circuit mechanisms and network architectures underlying the generation of cortical oscillations are presented.

In chapter two we characterize essential features of cortical oscillations in terms of duration and dominant frequency. We will show that they occur by short episodes in time, and each episode has a different dominant frequency, lasts for a variable duration, and its phase doesn't expand linearly with time. Nonetheless, our investigation reveals that oscillations, though variable, are coherent among distant regions in the presence of even weak interconnection and, therefore, can be used as a communication signal.

Chapter three presents a computational model intended to reproduce essential features of synchronous oscillations. Experimental observation has indicated that synchronous oscillations are concomitant with irregular and sparse firing discharges in individual neurons. In addition, they occur intermittently by short episodes in time. We show that interneurons that act on a very slow time scale are responsible in abolishing network oscillations.

Chapters four and five uncover the temporal coordination dynamics in membrane potential and local field potential recordings respectively. Stimulus onset induces a transient increase in noise correlation which subsequently declines to an intermediate, but significantly larger than ongoing, value. Modeling inquires show that two factors are essential in this dynamics; synaptic adaptation and network structure.

Last chapter, six, is a collection of open questions I've came across during my research but I never had time to thoroughly investigate them. Some of those seem very promising and their study might deepen our knowledge about neuronal circuits and their functions. These are presented with the hope that others will pick them up and piece them together.

Chapter 1

Neuronal oscillations in cortical networks

1.1 Introduction

Cortical oscillations are electrical activities with rhythmic and/or repetitive nature generated spontaneously and in response to stimuli. The discovery goes back to Hans Berger (1873-1941), who recorded the first electroencephalogram [1]. A century later, a surge of interest has led to an extensive study of cortical rhythms from various perspectives. This study offers an excellent venue to investigate how collective network dynamics emerge from the interplay between cellular biophysics and synaptic circuits. Coherent oscillations may play a role in spatiotemporal coordination and communication between neuronal populations simultaneously engaged in a cognitive process [2,3].

Cortical oscillations occur intermittently by short episodes in time [4] while confined to a local population of cells [5]. Large amplitude slow oscillations are observed in quiet sleep [6], while awake behaving animals show a desynchronized state [7]. The remained

mystery of network oscillations is that while they are present, spike discharges of cortical cells are highly irregular [8, 9], hence not so obvious how coherent oscillations emerge in network-level activity. Functional implications of rhythms regarding neuronal spike timing should be evaluated, rather than focusing on rhythms per se. In this framework coherent oscillations provide a channel for neurons and neuronal populations to communicate through seemingly random spiking discharges [2, 10].

In this chapter, I attempt to provide a quick and general introduction to the concept of oscillations and review some major works that have been performed in this area of inquiry (For a more detailed review of what has been presented here see Wang, 2010 [11]). In the first part of this review, I introduce different frequency bands commonly used in literature. Then I cover three properties of single neurons–phase response curve, subthreshold membrane oscillations, and resonance–that influence the emergence of oscillations, and may help us in digesting their functional implications. Next section is on the primary synaptic circuit mechanisms and network architectures underlying the generation of cortical network oscillations. Here, I present a theoretical framework for describing weakly synchronous network-level rhythms in which single cells fire action potentials irregularly and sparsely. Finally, the last section summarizes some general insights that we have gained from experimental and theoretical studies.

1.2 Oscillation frequency bands

Recording neuronal activity with a high temporal resolution, such as local field potential (LFP) of electrocorticogram, indicates that a variety of brain rhythms contribute in disparate behavioral states during wakefulness. Here is a very brief description of our major understanding.

1. Slow oscillations (< 1 Hz) Slow oscillations of up and down states are the dominant pattern during non-REM (slow-wave) sleep [12] which might play a role in memory consolidation [13, 14]. Large-amplitude slow rhythms are generated by all cell types repetitively switching between two membrane potential states: an up-state where neurons are depolarized at about ~ 65 mV and fire at a low rate, and a down-state where neurons are hyperpolarized by $10 - 15$ mV [15]. It is worth mentioning that a strong slow-wave oscillation at frequencies below 2 Hz is a striking feature of anesthesia [7].

2. Theta rhythm Theta (4 – 8 Hz) Theta rhythm has been observed in the neocortex [16] and was found to be enhanced during working memory [17]. Hippocampal theta rhythm is believed to play a critical role in the formation and retrieval of episodic and spatial memory [18].

3. Beta rhythm (15 – 30 Hz) Beta rhythm was initially observed in the primary motor cortex during "readiness" but vanished at the initiation of a movement [19]. Further studies confirmed the idea that beta rhythm is associated with preparation and inhibitory control in the motor system [20] and top-down signaling [21].

4. Gamma rhythm (30 – 80 Hz) Gamma rhythm has found to co-occur in temporally inter-nested with theta rhythms in the hippocampus [22] and also in spiking activity of

neurons in the primary visual cortex [23, 24]. These rhythms are a fingerprint of attention [25, 26] and are usually referred to as "hypervigilance rhythms" [27]. Gamma-band synchronization between neural ensembles may play a role in the integration of sensory information [28, 29].

5. Ultrafast oscillations ($>$ 100 Hz) Ultrafast rhythm has been found in the cerebellum, hippocampus, and neocortex [30–32] during wakefulness and non-REM sleep.

1.3 Interplay between neuronal populations

Recent technological advancements have led to the accumulation of a wealth of our knowledge about brain rhythms during behavior. Simultaneously recording of local field potential and single units from wake behaving animals made it possible to evaluate the timing of single-cell spiking activity relative to LFP oscillations. Moreover, optogenetic provides the opportunity to record and, more importantly, selectively manipulate specific cell types (pyramidal cells or different subclasses of GABAergic interneurons) *in vivo* [33, 34]. This yields valuable information about how they interact with each other and also with network-level rhythms. Results indicate that some subclass of cortical cells displays intrinsic oscillations through various sets of voltage-gated and calcium-gated channels. In this journey, mathematical analysis and neuronal network modeling provide complementary tools for understanding the dynamic behavior of cortical circuits.

What are the cellular mechanisms of cortical rhythmogenesis? One prominent hypothesis is that synchronous rhythms emerge through mutual excitatory connections. This idea gained support from accumulating experimental and computational studies on epilepsy,

where synaptic inhibition blockade led to extremely synchronous neural firings [35]. However, Wang and Rinzel [36, 37] showed, in modeling studies, that mutually inhibitory synaptic interactions are capable of synchronizing a population of GABAergic neurons. This complemented our understanding that synchronous oscillations can emerge via the interplay of excitation and inhibition [38]. Both the interneuronal and the excitatory-inhibitory network motifs critically depend on synaptic inhibition, not merely to control the overall network excitability but to temporally shape cortical network activity patterns during behavior.

1.4 Single neuron intrinsic property may affect network rhythms

Due to diverse active ion channels, different cell types display a variety of subthreshold membrane response dynamics and spike firing patterns. In fact synchronization of a neural ensemble greatly depends on the type and dynamics of ionic channels in its constituent cells. Oscillations shared by a neuronal population provide synchronized inputs to individual cells, and the way single neurons adjust the timing of their action potentials in response to periodic synaptic inputs determines whether the network displays persistent stable rhythms or not. Besides, the frequency of network-wide discharges is essentially determined by resonance properties of individual cells. What do we now know about the interplay between single neuron dynamics and network synchronization? Which aspects of cellular responses are relevant to network oscillations? Here I review three of these elements.

1.4.1 Phase response properties

In neuron with "type II" phase response curve, if a depolarizing pulse is applied before it fires a spike, it induces a phase advance (making it fire earlier) [39, 40]. However, a pulse current may delay the phase of the next spike when applied soon after the spike discharge in this type of cells. On the other hand, in a "type I" phase response, regardless of perturbation timing, the induced phase shift is always advanced. However, the amount of phase shift depends on the timing of the pulse perturbation [40, 41]. Type I and type II phase response curves can be produced by the same set of ion channels but with quantitatively different properties [42]. Now different scenarios can be explored by coupling neurons with similar or dissimilar phase properties. For type I neuron coupled with another type I neuron, the cell that fires earlier causes a phase-advance by the other cell that fires later. This acts against reducing the relative phase difference between the two. Hence, it is not straightforward to ascertain intuitively synchronization by mutual excitation between type I neurons. While coupling type II neurons readily can exhibit synchronized spiking.

1.4.2 Subthreshold membrane potential oscillations

In recent years subthreshold oscillations have been observed in many cell types, from hippocampus [43] to neocortex [44] and olfactory bulb [45]. A wealth of literature supports the idea that subthreshold membrane potential oscillations have ionic channel origin which includes a voltage-gated Na^+ and K^+ current interaction. Subthreshold oscillations naturally emerge as a result of interaction between a fast positive feedback (I_{Na}

current) and a slower negative feedback (I_K current). The oscillation frequency is controlled by the activation kinetics of K^+ currents [46]. Selective expression of a subset of these currents provides a powerful means for generating membrane oscillations at distinct frequencies which show itself in large-scale population activity.

1.4.3 Resonance

The interplay of passive and active properties makes a cell to bandpass filter its input currents as respond maximally at a preferred input frequency [47]. Resonance is intuitively expected when single neurons are damped oscillators, or more generally when there are two opposing processes, hence display an intrinsic preferred frequency [48]. It has been shown that pyramidal cells resonate in the theta frequency range while fast-spiking interneurons have a resonance in the gamma-band. Apparently, this suggests differential roles of these two major cell types in theta- versus gamma-frequency network oscillations [49].

1.5 Network mechanisms for rhythmogenesis

Excitatory principal neurons and inhibitory interneurons are the building blocks of any neuronal network. Phase reduction theory provides a general mathematical framework for studying synchrony of neuronal oscillators [39, 50]. The idea is that, if the synaptic coupling is weak enough, their effect can be well captured by the average over the oscillation period. Specifically, consider two oscillatory neurons with an intrinsic period of T_0 (frequency $f = \frac{1}{T_0}$), described by their respective phases ϕ_1 and ϕ_2 varying between 0 and

2π. The equations for describing the dynamics of the two interacting neurons are given by

$$\frac{d\phi_1}{dt} = 2\pi f + H(\phi_1 - \phi_2) \tag{1.1}$$

$$\frac{d\phi_2}{dt} = 2\pi f + H(\phi_2 - \phi_1) \tag{1.2}$$

with $H(\phi_1, \phi_2)$ as the interaction between neurons. The interaction function is given by the average of the product of synaptic current from cell 2 to cell 1, $I_{syn}(\phi_1, \phi_2)$, and phase response curve of cell 1, $Z(\phi_1)$, over an oscillatory period.

$$H(\phi_1, \phi_2) = \frac{1}{2\pi C_m} \int_{-\pi}^{\pi} d\phi . Z(\phi + \phi_1 - \phi_2) I_{syn}(\phi + \phi_1 - \phi_2, \phi) \tag{1.3}$$

Where the synaptic current from cell 2 to cell 1 is defined by

$$I_{syn}(\phi_1, \phi_2) = g_{syn} . s_2(\phi_2) . [V_1(\phi_1) - V_{syn}] \tag{1.4}$$

where V_1 is the voltage of cell 1, s_2 is the gating variable for the synaptic current, and Vsyn is the synaptic reversal potential. Subtracting equs.1.1 and 1.2, and replacing $\Phi = \phi_1 - \phi_2$ results in

$$\frac{d\Phi}{dt} = H(\Phi) - H(-\Phi) = H_{odd}(\Phi) \tag{1.5}$$

where $H_{odd}(\Phi)$ is the odd part of the interaction function. At steady-state phase locking, Φ_{ss}, relative phase should not change over time and, therefore, $H_{odd}(\Phi)$ should be zero. Furthermore, the slope of H_{odd} determines the steady-state stability. Now depending on the synaptic currents and phase response curves, a neuronal network might show stable synchronous dynamics.

In general, three types of synchronization mechanisms are conceivable: i) recurrent excitation between principal neurons, ii) mutual inhibition between interneurons, and iii) feedback inhibition through the excitatory-inhibitory circuits. Here I review each of these mechanisms.

1.5.1 Recurrent excitation between principle neurons

It has been shown that type II neurons are synchronized by sufficiently fast synapses [39] and the presence of voltage-gated K^+ currents enhances synchrony by mutual excitatory connections [51]. For type I neurons, even fast excitation does not generate phase-locking synchrony [39]. Indeed, type I neurons typically show anti-phase behavior with excitatory coupling [39].

A key insight from the theoretical analysis is that the time course of synaptic current is crucial for synchrony to emerge. Therefore, AMPA excitatory currents, with a decay time constant τ_{syn} in the millisecond range, is suitable for synchronizing slow rhythms at low frequencies [39, 52]. Experimental studies confirmed this prediction by showing that AMPA synapses are sufficient for synchronizing 5- to 10-Hz rhythms [53]. However, an excitatory-excitatory mechanism is insufficient for synchronizing at faster rhythms, such as gamma (30 – 80 Hz) oscillations.

1.5.2 Mutual inhibition between interneurons

A network of inhibitory interneurons provides a mechanism for gamma-band synchronization in spiking activity [54, 55]. Moreover, drugs that slowed down the kinetics of

$GABA_A$ receptor-mediated synaptic currents led to lower oscillation frequency [54]. At first glance, it seems paradoxical that reciprocal inhibition can make coupled neurons to fire synchronously, but it is a plausible mechanism for synchrony [56]. Consider a pair of coupled interneurons interacting by a reciprocally fast synaptic inhibition. Depending on the initial condition, if one neuron fires, it effectively suppresses the other and when this inhibition wanes over time, the other neuron becomes active and suppresses the first neuron in turn. In this scenario, coupled inhibitory neurons tend to fire out-of-phase with each other. Under a different initial condition, however, neurons can simultaneously fire action potentials, undergo inhibition together, and escape from it synchronously [56]. Whether an inhibitory neural network displays each of these two behaviors depends on the details of active neural properties and synaptic kinetics [57].

As mentioned above, different synaptic subtypes are suitable for synchronizing circuit rhythms at various frequency ranges. While $GABA_B$ inhibitory synapses ($\tau_{syn} \sim 100$ ms) are suitable to synchronize spike discharges at low frequencies, $GABA_A$ receptors ($\tau_{syn} \sim 5$ ms) can synchronize fast rhythms in the gamma frequency band.

1.5.3 Excitatory-inhibitory circuit

It has been shown that network oscillation emerges naturally in an excitatory-inhibitory circuit if recurrent connections are strong and inhibition is slower or delayed relative to excitation [38]. The mechanism is that when fast excitation depolarizes other neurons in the network, slower inhibition will gradually take off and eventually bring down population activity. Silencing excitatory neurons, the excitatory drive to interneurons wanes, then inhibition gradually decays and the network is ready to start the next cycle

anew [58,59]. In excitatory-inhibitory circuits, two regimes were identified [39,60]. In the first regime, interneurons are sufficiently activated by external inputs and, thus, exhibit a phase advance in reference to excitatory neurons. The dominant frequency of oscillations is comparable to single neuron firing rates. In the other regime, recurrent excitatory inputs mainly excite interneurons and, therefore, interneurons lag behind excitatory cells.

In local cortical circuits of the intact brain, both the interneuronal network mechanism and the excitatory-inhibitory feedback loop mechanism are present, and cause synchronized rhythms synergistically [39,61]. Depending on the strength and topology of the connections, each of these mechanisms can be dominant. For example, a mutual inhibitory circuit is typically dominant against excitatory-inhibitory circuit [39,62]. These mechanisms may be redundant to some extent. But this ensures the robustness of synchronous oscillations and, moreover, they complement each other by generating synchronous oscillations in different frequency bands, which seems to be useful in different brain states/functions.

1.6 Synchronous rhythms with irregular and sparse spiking

As mentioned above, understanding network oscillations is fraught with difficulty in part because of the temporally irregular spiking activity in individual neurons. While synchronous oscillations are present at network-level, individual spiking is highly irregular [63–67], such that it can be approximated with a random Poissonian process. How network-level rhythm appears while its constituent units are randomly spiking? To answer this, we need to understand the physical basis of network-level signals (such as LFP

and EEG) and how they relate to the electrical activity of single cells. LFP appears to reflect the weighted sum of neural synaptic inputs within a narrower spatial extent with a radius of $\sim 200\ \mu m$ [68] rather than spiking output [69–72]. Despite all the progress has been made in this area, the relationship between LFP and spiking activity has remained a controversy in the neuroscience community.

During cortical rhythms, cells fire at much lower rates (~ 5 Hz for pyramidal cells; ~ 30 Hz for interneurons) relative to the frequency of LFP oscillations [65]. Thus, How do LFP rhythms emerge out of random and sparse spiking output of constituent single-cells?

Modeling studies have shown that irregular and sparse neural firing can cause LFP rhythms if the rhythmic modulation of single-cell firing probability is negligible [52]. This has been illustrated experimentally for hippocampal pyramidal cells during gamma oscillations [73]. A series of works [52,74,75] has shown that if cortical neurons are bombarded with a large amount of background synaptic noise, they fire Poisson-like spike trains. Now if a population of such neurons randomly connected by delayed synaptic interactions, a surge of background noise can make pyramidals to fire stronger than usual, generating IPSPs that occur after a delay which hyperpolarizes neurons synchronously. When this inhibition wanes, another depolarizing and hyperpolarizing can happen, leading to a collective oscillation. Given that the transmission latency is of the order of a few milliseconds, this mechanism explains very fast oscillations (~ 200 Hz). However, heterogeneity of the neurons, transmission delays, and synaptic time course and, moreover, distance dependence of synaptic transmission delays can cause rhythms with diverse frequencies to appear [52,76–79]. Furthermore, in a network of coupled excitatory-inhibitory neurons,

rhythms can predominantly emerge from an interneuronal mechanism or an excitatory-inhibitory mechanism [52] and it can be shown that the latter causes slower oscillations than the former one ($\sim$ 40 Hz versus $\sim$ 200 Hz) [52].

It is again worth emphasizing that because the oscillatory component is significantly smaller than the noise, single-cell spikes remain highly irregular, and no sensible correlation is detectable between the mean firing rate of neurons and the network oscillation frequency. Therefore, the presence of LFP oscillation coexists with Poisson-like spike discharges of single cells. Theoretical analysis shows that the frequency of a collective network rhythm is determined by both the synaptic properties and single cell's membrane properties [52]. One important feature that has remained to be answered is the underlying mechanism for the intermittency of the rhythms. In chapter 3 I show that including a second type of inhibitory neurons (LTS interneurons) make this possible. The proposed mechanism is very intuitive, the interaction of excitatory and one of the interneuron types (FS interneurons) makes oscillations to appear, this synchronized inputs feed into LTS neurons and depolarize them, and in turn, they inhibit the whole network. Through this mechanism, oscillations appear and last for a short period of time.

1.7 Concluding Remarks

In this chapter, I started with an elementary introduction to the physiological basis of synchronous oscillations such as gamma and theta rhythms. Over the last two decades, our understanding of mechanisms and functional implications of the rhythms has been remarkably deepened. We have learned that a wide diversity of cellular and circuit mechanisms underlie the generation of rhythms in various frequency bands. A dearth of work

argues about the significance of single neuron properties–such as type I or type II phase response dynamics, resonance, pacemaker properties, voltage-gated sodium and potassium channels–on network oscillations. Years of research indicates the critical role of synaptic inhibition and its time course on circuit synchronization through either mutual inhibition in an interneuronal network or feedback inhibition in a reciprocal loop between excitatory and inhibitory neural populations.

One possibility to reconcile irregular and sparse neural firing with LFP rhythms is that rhythms can emerge from strong feedback synaptic interactions in an asynchronous circuit with a highly stochastic spiking activity of individual cells. Therefore, rhythms produced by a network of cortical circuits can be in the ultrafast band ($\sim$ 100 Hz) while single cells fire irregularly in a sparsely ($<$ 10 Hz) manner. An increasing number of recent studies have documented long-distance coherence as a tool for remote regions to communicate [2, 80–83]. About the source of irregularity, it is worth mentioning that it can be due to a strict balance between excitation and inhibition [84–86].

Last but not least, the advance of new techniques such as high-density multielectrode recording and two-photon calcium imaging has provided a unique opportunity to record simultaneously many single cells. Such data has the potential to uncover the role of input synaptic currents and output spiking on the spatiotemporal patterns of network oscillations. Furthermore, it will inspire more sophisticated mathematical models of neural circuit dynamics. The challenge is not only technical but also conceptual since cortical neural circuits and their dynamics are astonishingly complex, that cannot be described solely in terms of current mathematical tools. Therefore, I believe that new mathematical tools have to be developed to grasp, the inherently high-dimensional, nature of cortical neural circuits.

Chapter 2

Characterizing Evoked Oscillations in Primary Visual Cortex of Turtles

This work is in preparation for the Journal of Neurophysiology:

Mahmood S. Hoseini, Jeff Pobst, Ralf Wessel.

Department of Physics Campus Box 1105 Washington University St. Louis Missouri 63130-4899 USA

2.1 Abstract

Functional roles of oscillations in cognition are still a matter of debate in neuroscience community. Bursts of oscillations are generally thought to be a core mechanism by which remote brain regions can communicate. Using time-frequency analyses of local field potentials (LFPs) and membrane potentials (V_m) recorded from turtle primary visual cortex (V1), we found large variability in spectral and temporal properties of oscillations. Results indicate a broad distribution of durations (ranges up to $\sim$3 s) and peak frequencies with little or no interdependence of these distributions. Furthermore, our results show that, over the time window of a given epoch, oscillations in both LFP and V_m are not autocoherent that means the phase doesn't persist linearly in time. In addition, consistent with previous studies on phase coherency, evoked oscillations are more coherent than ongoing oscillations while in V_m no significant difference between two epochs has been observed. In conclusion, this study supports the possibility of oscillations being used by remote brain regions for communication despite their variable nature.

Keywords: Coherent oscillations, Visual cortex, multi-electrode array (MEA), local field potential (LFP), membrane potential (V_m)

2.2 Introduction

Rhythmic oscillations have been found in many species and brain structures (for a review see [11]). They were discovered in cat neocortex [27], rat hippocampus and auditory

cortex [65, 87], human motor cortex and olfactory bulb [19, 88], and visual and auditory cortices of monkeys [89, 90], to name a few. Furthermore, oscillations exist even in brain slices [55, 64, 91, 92]. Despite being studied extensively, the functional significance of oscillations is unclear and a topic of debate in the neuroscience community. A long-standing hypothesis (communication through coherence) is that oscillations provide temporal windows for long-range communication between multiple distant regions [2, 3, 93–96].

To serve as a communication signal and, moreover, feature binding [28, 97], neuronal oscillations need to be reliable and co-vary among remote regions. The aim of this study is to characterize oscillations in V1 and address whether oscillations in primary visual cortex of turtles are coherent enough to serve as a clock signal. One intriguing question to investigate is the relationship between local filed potential (LFP) and single-cell membrane potential oscillations. This exploration provides clues on the source, and possible functional implications, of oscillations. Although some experimental studies [82, 98–101] have proposed the existence of a consistent LFP-V_m relationship more recent studies [102, 103] rule out this hypothesis.

To address these questions, we recorded ex vivo from primary visual cortex in turtles using extra- and intracellular electrodes. In line with previous works [104, 105], large variability of the duration and peak frequency of oscillatory bursts has been observed. Moreover, a large variation is found between electrodes and preparations. Despite large stimulus-induced and time-dependent variability, oscillations show a strong coherence at the stimulus onset, which justifies their application as a communication signal. Furthermore, qualitative discrepancies between single-cell membrane potential and LFP oscillations are discussed.

2.3 Materials and methods

2.3.1 Ex-vivo eye-attached whole-brain preparation

Adult red-ear turtles (Trachemys scripta elegans) were used in this study. Procedures used in this study were approved by the Washington University Institutional Animal Care and Use Committee and conform to the guidelines of the National Institutes of Health on the Care and Use of Laboratory Animals. Rapid decapitation was performed after anesthetization with Propofol (10 mg/kg) as described in Ziolo and Bertelsen 2009 [106].

The brain was surgically removed from the skull with the right eye attached and continuously perfused with artificial cerebral spinal fluid bubbled with 5% carbogen. The anterior half of the right eye was removed to provide a clear path to project images onto the retina (fig.2.1A). Starting from the left olfactory bulb, a rostral-caudal incision was made along the medial cerebral hemisphere allowing us to unfold the cortex and expose the ventricular surface of the visual cortex. Afferent synapses remain intact in surgery since the geniculocortical axons pass beneath the dorsal ventricular ridge (DVR), pass through the pyramidal cell layer of the dorsal cortex and make synapses on the apical dendrites of the pyramidal cells as well as interneurons (fig.2.1B).

2.3.2 Visual stimuli

For the included studies, three methods of visual stimulation were used. i) For LED stimulation, a red LED (Kingbright, 640 nm) was connected to the output of a National

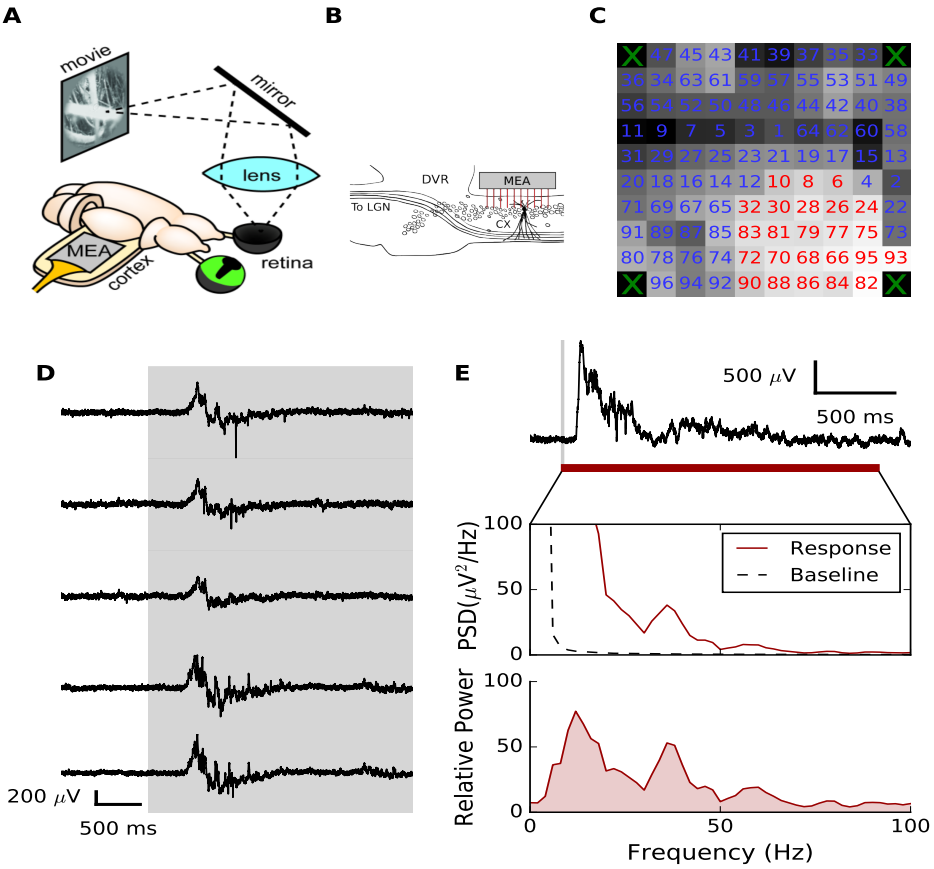

Figure 2.1: **Experimental setup and raw data.** A: Experimental set up using a monitor and mirror. The visual stimuli are presented on a monitor. The image reflects off a mirror and through a lens to form a picture on the retina of the turtle's hemisected eye. The multi-electrode array is placed in the unfolded cortex. B: A side view of the cortex showing lateral geniculate nucleus (LGN) axons passing through and then below the cellular layer of the cortex. The dendrites of one pyramidal cell are included to show the spatial extent of the dendritic arbors. In red are the electrodes from the MEA. C: Visual responsiveness across the electrode array for one of the preps. Each square represents an electrode. The background color for each square indicates the visual responsiveness with black being 0 and white being 1. The electrodes labelled in red have a visual responsiveness above the threshold, 0.75, to be included in analyses, and the electrodes labelled in blue had subthreshold responsiveness. D: Five simultaneous raw extracellular voltage recordings from electrodes in responses to natural movie stimulation. E: Relative power of a voltage trace. A 2 s sample recorded voltage trace in response to 50 ms red LED flash is shown. The power of this signal (red curve in middle inset) divided by the baseline power of the signal before stimulus onset averaged over many trials (dotted curve in middle inset) gives us the relative power (bottom inset).

Instruments BNC-2090 terminal block connected to a National Instruments PCI-6024E DAQ board. This output was controlled with a custom LabView program on a computer running Windows 7. ii) For monitor/mirror stimulation (fig.2.1A), a 19″ LCD monitor (Samsung model Syncmaster T190) displayed the stimuli. This image was reflected off a mirror located across room above the tissue, and focused on the retina with a lens placed above the tissue. iii) For projector stimulation, an AAXA P4 X projector combined with a system of lenses (Edmund Optics) to project images generated by a custom software package directly onto the retina. Both monitor/mirror and projector stimulation was provided using software written in python on a computer running Ubuntu 10.4. Visual stimuli included black dots moving on a white screen, red LED flashes, brief (100 – 250 ms) whole-field and sub-field flashes (red or white), sustained (10 s) gray screen, a naturalistic movie (*CatCam*), a motion-enhanced movie (*Gallant*), and a phase-shuffled version of the same movie.

2.3.3 MEA recordings and data acquisition

Data were collected at 30 kHz using the Cerebus data acquisition system by Blackrock Microsystems. Two different styles of microelectrode arrays were used for our LFP recordings. For some recordings, we used a 96-channel array (10-by-10 square grid, 400 μm inter-electrode spacing, 500 μm electrode length, no corner electrodes, Blackrock Microsystems). For others, we used an array of shank electrodes (44 array of shank electrodes with 8 recording sites on each electrode, 300 μm and 400 μm x and y distance between shanks and 100 μm between recording sites along a shank). We attached either array to a post fastened to a micro-manipulator (Sutter, MP-285) and inserted the array to a depth of 500 μm starting from the ventricular side of the unfolded cortex such that the

plane of electrodes was parallel to the dorsal surface of cortex. We recorded wide-band (0.7 Hz to 15 kHz) extracellular voltages relative to a silver chloride pellet electrode in the tissue bath (fig.2.1D).

2.3.4 Determining visually responsive electrodes

Since visual responses do not show up on all the electrodes, it is necessary to systematically determine which electrodes to include as visually responsive. For this purpose we quantify the level of spontaneous activity on each electrode by averaging over windows immediately before presenting the stimulus. Doing the same quantification for a window immediately following the onset of the stimulus, the normalized difference of these two quantities is our measure of visual responsiveness. We classify an electrode as visually responsive if this ratio is greater than 0.75 (fig.2.1C).

2.3.5 Intracellular Recordings

Whole-cell current clamp recordings were done by patch pipettes ($4-8\ M\Omega$), pulled from borosilicate glass and filled with a standard electrode solution (in Mm; 124 $KMeSO_4$, 2.3 $CaCl_2 - 2H_2O$, 1.2 $MgCl_2$, 10 HEPES, 5 EGTA) adjusted to pH 7.4 at room temperature. Cell patching was done under a dual interference contrast microscope (Olympus) with intracellular activity, membrane potential V_m, recorded using an Axoclamp 900 A amplifier, digitized by a data acquisition panel (National Instruments PCIe-6321), sampling at 10 kHz. Simultaneously recorded cells were located less than 300 μm apart. We excluded cells that did not display stable resting membrane potentials.

2.3.6 Data analysis

Burst Detection

To detect bursts of fluctuations in the LFP and V_m, we filtered the raw signal using 9 different 10 Hz wide pass-bands from 10 to 100 Hz. We then took the Hilbert transform of each of these filtered signals and normalized it by dividing by its mean value. Finally, we created a new array by taking the maximum value from all 9 normalized Hilbert transforms at every time step. This new array indicates whether there was substantial activity in any of the 9 pass-bands we considered. This array was used to look for bursts of oscillation. To do so we looked at all the crossing of both a high threshold (6 STD) and a low threshold (4 STD). Each time the signal crosses the high threshold becomes part of a burst, and the onset (and offset) of each burst is defined by extending forward (and backward) in time from the high threshold crossing until there is more than to the next low threshold crossing. The data used for burst duration distributions came from recordings including a mixture of visually evoked and dark periods.

Relative power

We examined visually evoked LFP and V_m responses to look for trends in the frequency profiles. Our primary measure of power at a given frequency is the relative power. The relative power is the power during a 2 s period after a stimulus onset divided by a baseline power (fig.2.1E). The baseline power was calculated by taking the average of the power spectral densities of all the 2-second periods before the stimulus onsets, during which any recorded activity was not visually evoked. To calculate the power spectral densities,

we down sampled our LFP recordings to 3 kHz and then performed multitaper (3 tapers) spectral estimations of 500 ms sliding windows (sliding by 50 ms) covering the 2 s periods. The average of these sliding windows were used as the powers to then calculate relative powers.

Peak frequency

To allow for the detection of peaks in relative power at more than one frequency for a single trial, we looked at more than simply the maximum value in the relative power. Instead, we started with all local maxima in relative power, and called the maxima peak frequencies if they met three conditions: 1) there must be a neighborhood around that frequency in which the relative power at some higher frequency (and lower frequency unless the neighborhood includes 0 Hz) was at most 1/4 the relative power of the putative peak frequency, 2) in this neighborhood, the putative peak frequency must have the highest relative power, and 3) the relative power at the putative peak frequency must be at least 4 (the evoked power must be at least 4 times the baseline power).

Wavelet transform

The Fourier transform of a signal allows us to have frequency components with the highest resolution. However, the uncertainty principle limits the temporal resolution we obtain. We know what frequency components exist in the signal but we do not know where in time different components are triggered. To get information on temporal dynamics of

the signal we have to give forfeit frequency precision. Wavelet, short-time Fourier, transform is designed for this purpose. The wavelet transform is suitable for analyzing non-stationary time series that contain power modulation at many different frequencies [107]. The time series signal is first multiplied by a window function, also called wavelet function, and the resulting signal is Fourier transformed to render the time-frequency content.

$$\int_{-inf}^{inf} d\tau . X(\tau)\psi^*(\tau - t, f) = R(t, f)exp(j\phi(t, f)) \tag{2.1}$$

where $X(\tau)$ is the signal to be transformed and the (*) indicates the complex conjugate. For our wavelet function we used the Morlet wavelet, consisting of a plane wave modulated by a Gaussian:

$$\psi(t - \tau, f; s) = \pi^{-1/4} exp(\frac{-(t-\tau)^2}{2s^2}) exp(j2\pi f t) \tag{2.2}$$

in which τ and s are center and temporal extent of the window function.

Analysis of the phase of the oscillations

To characterize phase distributions, voltage traces were sliced offline from -2 to 2 s from stimulus onset and padded with enough zeros to avoid edge effects of the wavelet transformation. The Morlet wavelet at 29 scales from 1.5 to 193 Hz provides us with instantaneous phase and amplitude across time and frequency. Based on results from previous studies (see Lakatos et al., 2007 [96] and references therein), six frequency bands were defined and used to quantify phases across trials in either a single or simultaneously recorded signals.

Single voltage trace: phase trajectories can be plotted in polar coordinate with radius as the amplitude and phase of the complex numbers during time. We define a frequency component that can be modelled as a sinusoidal function with a fixed phase as an auto-coherent signal. To compare the phase of a voltage signal to a pure sinusoidal signal, we define residual phase, $\phi_{res}(t,f) = \phi(t,f) - 2\pi mod(t, 1/f)$. If this quantity is not changing over time, signal in auto-coherent and parametric trajectories with residual phase in a polar plot should be confined in a sector of space while otherwise a random trajectory can be seen and signal is not auto-coherent. To quantify localization of the trajectories in phase portraits circular variation (CiV) is defined as,

$$CiV(f) = 1 - \frac{\Sigma_t R(t,f) exp(j\phi_{res}(t,f))}{\Sigma_t R(t,f)} \tag{2.3}$$

CiV is always normalized to be between zero and one with zero for the most coherent (sinusoidal) and one for signal with completely random phase drift [108,109].

Simultaneous voltage traces: To characterize phase locking between simultaneously recorded signals in each frequency band, phase concentration, $R(t,f)$, was calculated and averaged for 2 s before and 2 s after stimulus onset. At a given frequency and time, $R(t,f)$ can be defined as,

$$R(t,f) = cos(\phi_2(t,f) - \phi_1(t,f)) \tag{2.4}$$

in which ϕ_i is instantaneous phase of the signal $i = 1, 2$ [96,100,110]. The phase concentration ranges from -1 to 1; with positive value for phase locking and negative for anti-phase locking. Higher absolute values indicate that the observations are more closely clustered around the mean than the values closer to zero.

2.4 Results

2.4.1 Overview

Taking the power spectral density (PSD) of the voltage signal can be useful to learn about the spectral properties during that time, but there are a few drawbacks to simply looking at the PSD. Typically when looking at an evoked response or any event of neural activity, were interested in how that activity is different than the ongoing spontaneous activity. If we simply look at the PSD we dont get this information. For instance, if there was a consistent ongoing high power in a band near 80 Hz, then seeing that peak during a period of evoked activity would not indicate that any information was carried by that high power. Also, if one wishes to look at the changes in power of many electrodes, one might be misled by different electrodes having different impedances. To deal with these issues, we use relative power (see Materials and methods).

2.4.2 Variability in oscillatory bursts

The relative power at a given frequency represents the extent to which the power in that frequency has increased beyond an average baseline level calculated from periods without stimuli. Our analyses indicate that there isnt a systematic change in the relative powers and no recurrent feature is visible (fig.2.2). The top plot shows 1 s LFP voltage traces in response to 50 ms red LED flashes with their relative power shown immediately at their bottom. Relative powers for 30 more trials are shown at the third row which pin points two important features of the oscillations. First of all, the relative power often has peaks

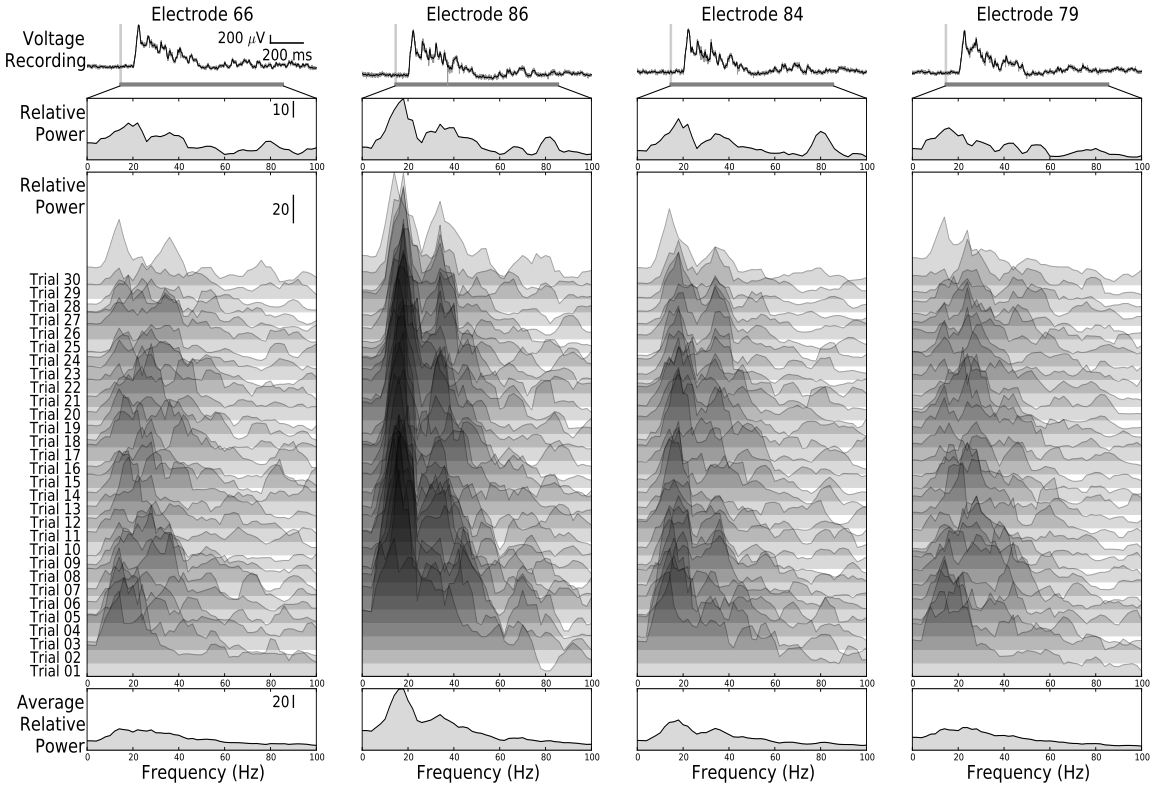

Figure 2.2: **Variability in oscillatory bursts of LFPs.** Recordings from four nearby electrodes in response to 50 ms red LED flashes. The top plot shows one-second voltage traces with their relative power plotted for that single trial in second row. Beneath that, the relative power is shown for 30 more trials and the last row is the average relative powers over all trials.

within narrow frequency bands, and multiple peaks can be present simultaneously. It is useful to think of each peak as being generated by some neural circuit. Second, several types of variability worth mentioning:

i) trial-to-trial variability: Each set of 30 repeated trials demonstrate that there can be significant trial-to-trial variability. While there is, consistently, an increase in power at some low frequency, the sharpness of the peak frequencies, and the centers of those peaks vary from trial to trial. Often, there are certain frequencies that have high relative powers in

most trials but not all. This suggests that there is a neural network that is typically activated by the given stimulus, but occasionally it is either inactive or overwritten by a more active network motif.

ii) electrode-to-electrode variability: For a single trial, peaks in relative power are often shared with nearby electrodes, but different peaks may see their maximal relative power at different electrodes. In some instances two distant electrodes may share peaks that do not show up on electrodes in between. In some data sets, it appears that one subset of electrodes tends to have a specific peak frequency, while another subset tends to have a different peak frequency. These electrode subsets often overlap. More detailed correlation exists between electrodes in the time domain using narrow filters corresponding to the frequency bands identified by the relative power plots.

To gain insight into the role of membrane potential, V_m, oscillations in the oscillations observed in collective LFP signals, we investigated relative power of V_m traces (fig.2.3). The top plot shows 1 s voltage traces in response to the movie with their relative power shown in second row. Beneath that, relative powers for 20 more trials are shown along with their averages plot in the last row. Aforementioned type of variability is still present in V_m oscillations but with a remarkable difference in the frequency. Low frequency oscillations are more prevalent in V_m than LFP.

Other type of variability not indicated by this plot is stimulus-to-stimulus variability. There can be a huge variability in relative power peaks in response to different stimuli presented (data not shown). All this variability types indicate the versatile functional roles of oscillatory bursts in information processing in visual cortex.

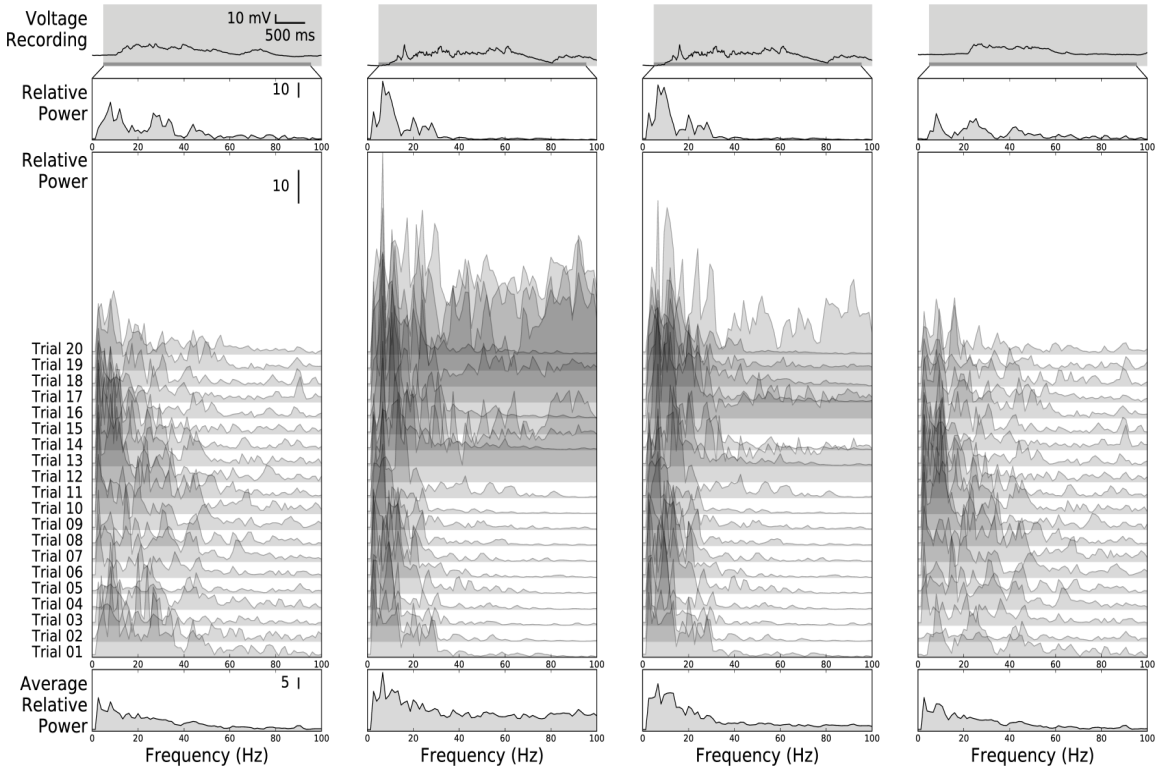

Figure 2.3: **Variability in oscillatory bursts of membrane potential recordings.** Recordings are from four cells in response to a naturalistic ten-second movie. The top plot shows one-second voltage traces with their relative power plotted for that single trial in second row. Third row shows the relative power for 20 more trials, which indicates that oscillations are likely to occur at lower frequencies (< 20 Hz). The last row is the average relative powers over all trials with a gamma-like profile.

2.4.3 Duration and peak frequency distribution

Understanding oscillation variability roles in cognitive processes requires characterizing properties of oscillatory epochs. This also helps in constructing computational models. Considering the synchronizing role for neuronal oscillations in the brain raises a question

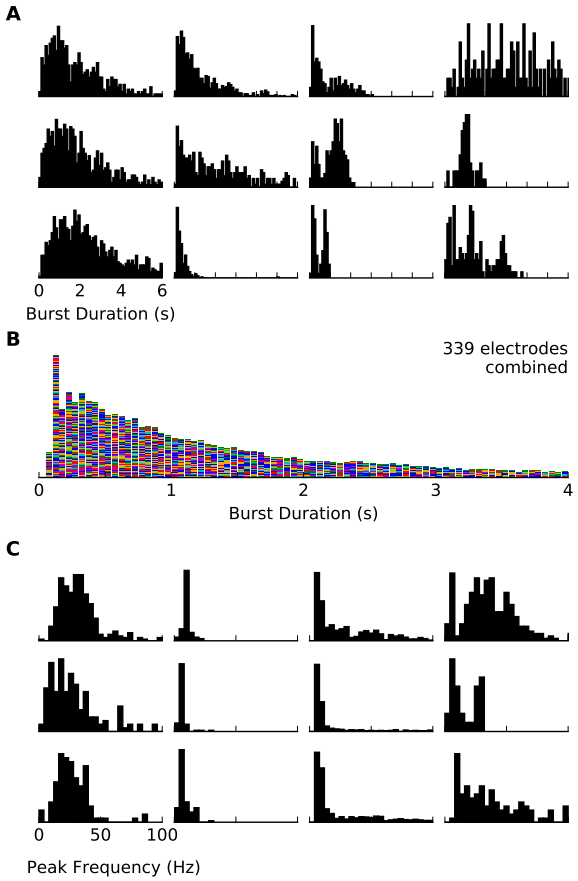

Figure 2.4: **Variable duration and peak frequency distributions in LFPs.** A: Burst duration distributions for a single electrode from twelve different turtles. They have been arranged by column, purely by visual inspection, to demonstrate a few recurring features: a broad, gamma-like distribution peaked at duration near 1 s; a narrow distribution with most bursts being less than 1 s; bimodal distributions; and three other distributions without any particular common feature simply to further illustrate the diversity of burst duration distributions. B: This shows the distribution of the bursts from 53 turtles (339 electrodes) combined. The contribution from each turtle is colored differently from the others near it, by simply cycling through 8 colors. C: Distributions of relative power peak frequencies for a single electrode from twelve different turtles. Again a few recurring features are: a broad distribution of peak frequencies primarily between 10 Hz and 40 Hz; a narrow distribution less than 20 Hz; a narrow distribution less than 20 Hz along with occasional peak frequencies covering a broad range of frequencies; and three additional distributions to further demonstrate the diversity of peak frequency distributions.

about the existence of a characteristic duration and frequency for oscillation epochs. Neuronal rhythms should last as far as the brain is processing information while frequency should remain unchanged.

Using Hilbert transform (see Materials and methods, Burst detection), we explored patterns appeared in burst duration profiles (fig.2.4A). Burst duration distributions for a set of 12 electrodes (fig.2.4A) are arranged by column, just by visual inspection, to demonstrate a few recurring distributions: a broad, gamma-like distribution peaked at duration near 1 s; a narrow, exponential-like distribution with most bursts being less than 1 s; bimodal distributions with most bursts being less than 2 s; and three other distributions without any particular common feature simply to further illustrate the diversity of burst duration distributions. Distributions from 53 turtles (total 339 electrodes) are combined (fig.2.4B). The contribution from each turtle is colored differently from the others near it, by simply cycling through 8 colors.

The speculation is that there could be space dependence for oscillation features. Since we recorded from a slightly different location each time, we would end up with a different duration profile. Another possibility could be the different internal state of the brain at the time of presenting the stimulus. Brain response is a complex interaction of inputs from sensory system with the spontaneous activity (internal state) of the brain at that time. As far as we don't have any control on the internal state, even presenting the same stimulus would lead to different responses.

Variable duration doesn't hurt on its own especially when durations are an order of magnitude longer than the time scale on which neuronal circuit process information and oscillations can still be used as a means for long range communication. However, variable frequency could have an adverse impact on this function of oscillations in the cortex. We examined visually evoked LFP responses to look for patterns in the frequency profiles. Our primary measure of power at a given frequency is the relative power. Using our approach (see Materials and methods, Peak frequency) we were able to detect multiple

peaks in relative power at more than one frequency for a single trial. Our analysis indicates that relative power peak frequencies for a single electrode from twelve different turtles show a noticeable variability (fig.2.4C). Profiles have been arranged to demonstrate a few recurring features: a broad distribution of peak frequencies primarily between 10 Hz and 40 Hz with a gamma-like distribution; a very narrow distribution less than 20 Hz; a narrow distribution less than 20 Hz along with occasional peak frequencies covering a broad range of frequencies; and three additional distributions to further demonstrate the diversity of distributions.

To trace back the variability occurring in LFP signals to the oscillation in membrane potentials, we did the same exact analysis on V_m signals (fig.2.5). Duration profiles are variable with some recurrent features (fig.2.5A). Though, two important differences between burst profiles in LFP and V_m worth mentioning: V_m oscillations (i) are generally shorter (< 3 s), and (ii) show more frequent very brief durations (sharp peak at low durations). Combined duration still shows the same profile (fig.2.5B). Moreover, peak frequency profiles are diverse (fig.2.5C) with some recurrent features and, still, more prevalent low frequency oscillations.

2.4.4 The phase drift within an epoch of oscillation

A largely controversial topic in oscillation literature is that whether oscillations act as a "clock" signal, by which information can be transferred among remote regions in the brain. Evaluation of the phase of the oscillation epochs might shed light on this question [66, 93, 108, 111]. A deterministic mechanism leads to auto-coherent oscillations; in which phase unfolds linearly with expanded time. It then provides a unique reference time

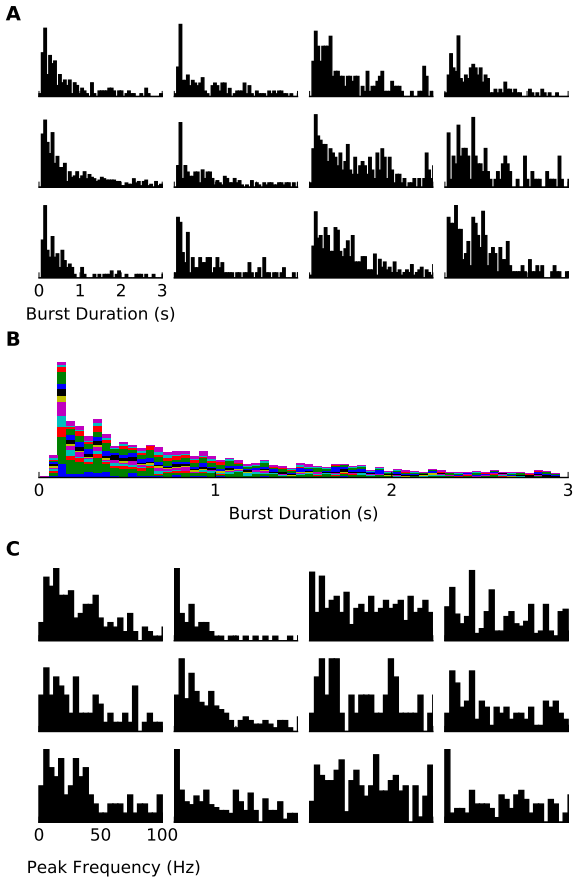

Figure 2.5: **Variable duration and peak frequency distributions in membrane potentials.** A: Burst duration distributions for twelve different cells. Columns are arranged to demonstrate a few recurring features: a narrow distribution with most bursts being less than 1 s; a very narrow distribution with a sharp peak at low durations; a more slowly decaying distribution; and three others without any particular common feature. B: This shows the distribution of the bursts from all cells combined and stacked on each other. C: Distributions of relative power peak frequencies for twelve different cells. Again a few recurring features are: a broad distribution primarily between 10 Hz and 50 Hz; a narrower distribution with a sharp peak at low frequencies; a broad distribution with all frequencies equally likely to occur; and three additional profiles to further demonstrate the diversity of peak frequency distributions.

for precise temporal encoding of visual information. On the other hand, having phase not evolving as a sinusoid makes aforementioned straightforward interpretation rather too complex. However, it leaves the temporal coordination functionality of oscillations possible on very short window of time. Nonetheless, this test helps us to keep or rule out many proposed rhythmogenesis mechanisms.

To this end, we use a time-frequency analysis method first proposed by Burns et al. [108]. Their analyses for the data from monkey V1 have indicated that gamma-band oscillations dont have the properties of a clock signal. Moreover, they showed that EEG signals in alpha rhythms are auto-coherent. They used circular variation (see Materials and methods; CiV) as a measure of localization of parametric paths in phase space. The CiV is the ratio of average complex coefficients from CGT normalized by average amplitudes of the coefficients. A CiV close to zero indicates that trajectories are localized in a sector of space and phase is nearly conserved, an auto-coherent oscillation. The other limit, CiV close to one, implies that the phase path is wandering all over the space and oscillations are not auto-coherent.

A 4 s LFP trace (fig.2.6A) along with its power spectrum (fig.2.6B) in response to a 10 ms red LED flash triggered at 1 s is shown. Spectrum shows elevated power for a wide range of frequencies (5 – 110 Hz). Phase portraits, with residual phases, are plotted in polar coordinates for 9 frequency bands from 10 to 100 Hz with the increment of 10 Hz (fig.2.6C). Radius of the trajectories is amplitude of the coefficients, which is actually square root of the power, and their phase is the residual, sine wave phase subtracted, phase of the coefficients. Except for alpha-band all other CiV values are very large and close to one that indicate oscillations in gamma-band aren't auto-coherent. Since auto-coherent oscillations have been observed in rat hippocampus on shorter time scales ($<$ 100 ms) [112,113], we tested CiV values during just elevated power, from 1 to 1.5 s, and results remained unchanged.

Summarizing CiV values over all recording sessions (3146) gives widely distributed histograms from 0.3 to 1 in alpha-band with slightly left-skewed distributions and rather

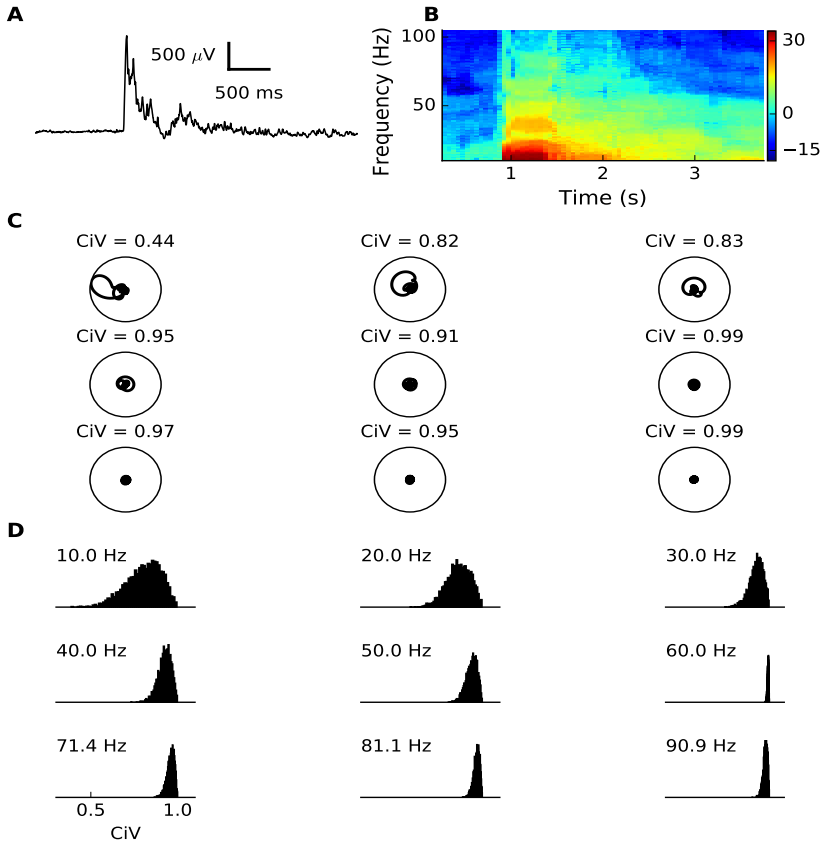

Figure 2.6: **Phase drift of oscillation epochs in LFPs.** A: A 4 s voltage trace from one of the extracellular electrodes. A 10 ms red flash is triggered at 1 s. B: Power spectrum of the signal for frequencies less than 100 Hz. It shows an increase in power at the onset of the stimulus. C: Parametric phase portraits of the data shown in A for frequencies from 10 to 100 Hz with the increments of 10 Hz. CiVs are shown at the top of the polar plots. D: CiV histograms for alpha and gamma rhythms for all recording sessions. Each inset is a CiV histogram, at the frequency listed on its top, for 3146 of 2 s LFP recordings in response to 10 ms red LED flashes. Broad distribution of CiVs in alpha-band (10 – 30 Hz) fails to reject auto-coherent of oscillations. In contrast, very sharp distribution of CiVs in gamma-band (30 – 100 Hz) indicates that oscillations aren't auto-coherent.

sharper histograms in gamma band (fig.2.6C). CiV in gamma-band are significantly different from zero (ttest; $P < 0.001$) and therefore oscillations arent auto-coherent, while ttest fails to reject auto-coherent of alpha-band oscillations ($P = 0.12$). These results, in line with those presented in Burns et al. [108], suggest that alpha-band oscillations can

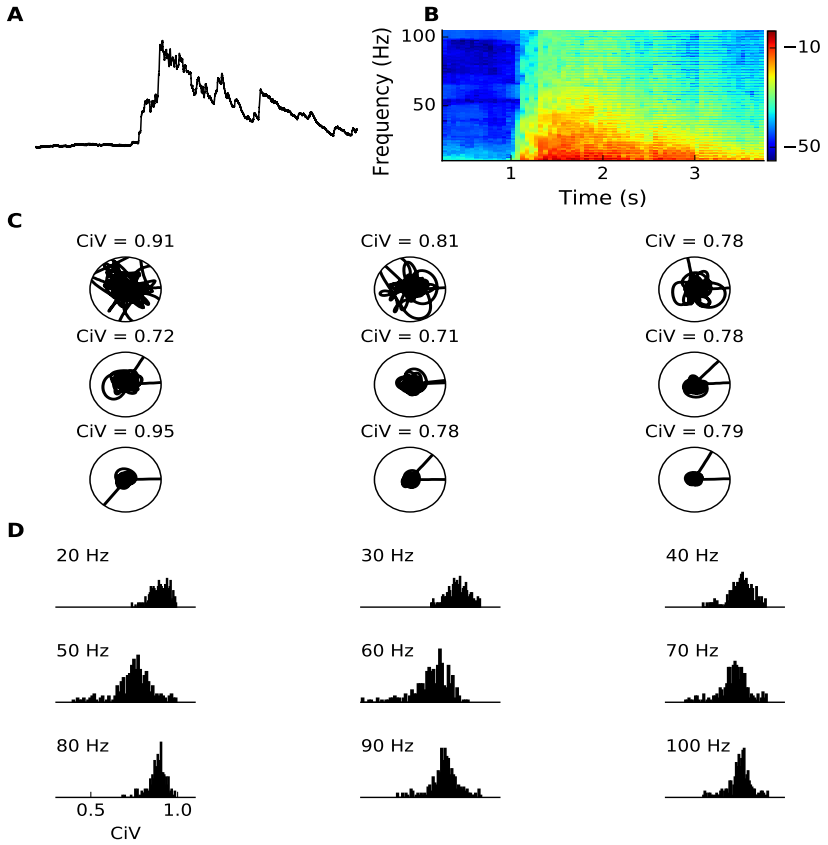

Figure 2.7: **Phase drift of oscillation epochs in membrane potentials.** A: A 4 s voltage trace of a cell in response to a naturalistic movie started at 1 s. B: Power spectrum of the signal for frequencies less than 100 Hz. It shows an increase in power in low frequencies ($<$ 20 Hz) at the onset of the stimulus. C: Parametric phase portraits of the data shown in A for frequencies from 10 to 100 Hz with the increments of 10 Hz. CiVs are shown at the top of the polar plots. D: CiV histograms for the given frequencies. Each inset is a CiV histogram for 297 trials of intracellular recordings in response to the movie. Broad profile of CiVs in gamma-band (30 – 100 Hz) fails to reject auto-coherent of oscillations. In contrast, alpha-band oscillations are auto-coherent ($P < 0.001$)

play as a clock signal in order to synchronize distal brain regions and help to bind features of visual stimuli. This raises the question that to what extent these features originate from membrane potentials? Or is there any relationship between oscillations occurring in these two disparate scales? To answer these questions, we analyzed phase of oscillation epochs in V_m traces. A 4 s response to a movie triggered at 1 s is shown (fig.2.7A) along with its power spectrum (fig.2.7B) and phase portraits in 9 frequency bands (fig.2.7C).

Summarized histograms for 297 trials (fig.2.7D) show a broader distribution in comparison to LFP signals (fig.2.6D). V_m CiV histograms show that alpha-band oscillations are auto-coherent (ttest; $P < 0.001$) while gamma-band isn't (ttest; $P = 0.34$). This gives us little clue on V_m oscillation's impact on LFP signals and this may happen due to disparate microcircuit structures, different types of neurons and neuronal properties, dendritic nonlinearity, and etc.

2.4.5 Communication through coherence

So far, we have shown that oscillations show variable instantaneous amplitude, frequency, and phase. So the question that arises is that what are the functional implications of neuronal oscillations? One prominent theory is that neuronal oscillations offer a mechanism for neuronal communication by coherence between the oscillations in the sending and receiving populations [2, 10, 99, 100]. Oscillations induce rhythmic excitability fluctuations and this opens up a window of opportunity for neuronal groups to communication. The necessary condition for this hypothesis to work is that the opening of their communication windows should be coordinated between the groups. Under this condition, outputs of the sending groups would reach to the target group at the prefect time and they elicit a significant response in it. Temporal coordination happens through frequency and phase matching of oscillations in recording sites. Our analysis indicates that stimulus-induced oscillations has more power across all frequency bands (data not shown) are more coherent that ongoing oscillations (fig.2.8). Phase concentration value, with 0 for random phase, 1 for phase locked, and -1 for completely anti-phase locked signals (see Materials and methods; Analysis of the phase of the oscillations), shows significant increase from ongoing to evoked epoch (ttest2; all $P << 0.001$). Two points worth mentioning; first

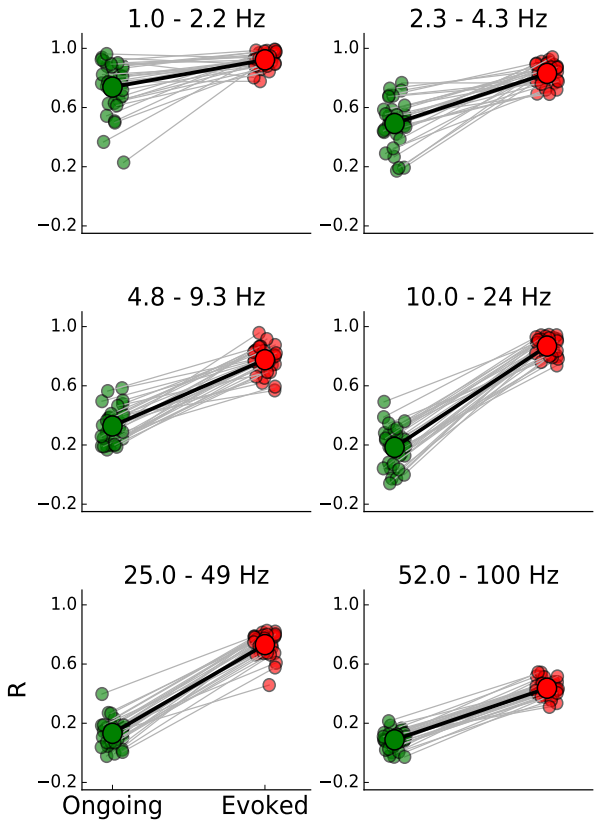

Figure 2.8: **Stimulus-induced oscillations in LFP are more coherent that ongoing oscillations.** Phase concentration, R, has shown for six frequency bands across 30 trials for one LFP channel averaged over 2 s windows. Green circles are for ongoing and red circles for evoked epoch. Individual trials are shown in low opacity and the averages in higher opacity. Phase concentration increases significantly for all frequency bands (1 – 2.2 Hz, 0.73 to 0.92; 2.3 – 4.3 Hz, 0.49 to 0.83; 4.8 – 9.3 Hz, 0.32 to 0.77; 10 – 24 Hz, 0.18 to 0.86; 25 – 49 Hz, 0.13 to 0.73; 52 – 100 Hz, 0.08 to 0.43; all $P << 0.01$).

all values are positive and no anti-phase locking has been observed, and second, largest increase is seen in gamma band activity (25 – 49 Hz, 0.13 to 0.73; 52 – 100 Hz, 0.08 to 0.43). Our results, in line with other works [96, 114], justify one assumption of communication through coherence theory.

To test this hypothesis on membrane potential traces, we did the same time-frequency analysis on simultaneously recorded membrane potentials. First of all, power increases

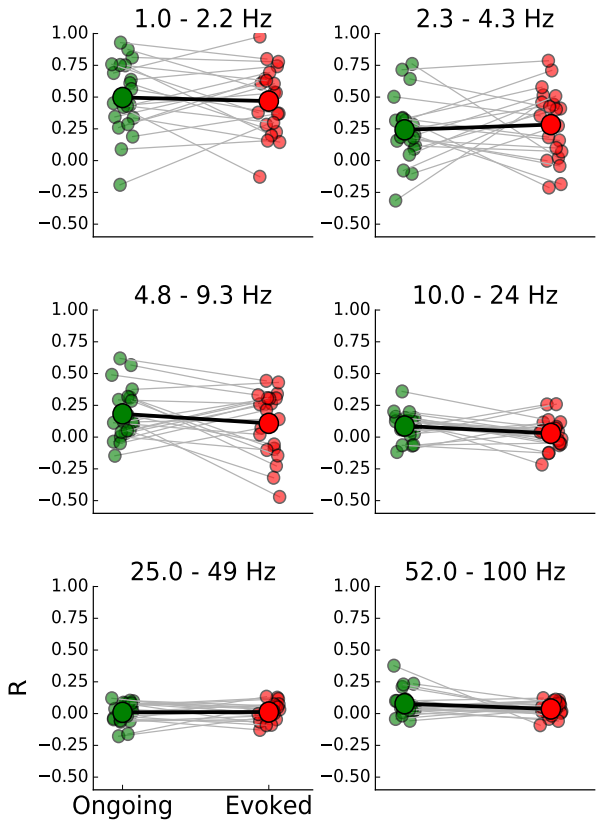

Figure 2.9: **Stimulus-induced oscillations in membrane potentials do not show a significant increase in the phase concentration.** Stimulus-induced oscillations in membrane potentials do not show a significant increase in the phase concentration. Same format as (fig.2.8)(1.0 – 2.2 Hz, 0.49 to 0.46, $P = 0.74$; 2.3 – 4.3 Hz, 0.24 to 0.28, $P = 0.6$; 4.8 – 9.3 Hz, 0.18 to 0.10, $P = 0.31$; 10 – 24 Hz, 0.08 to 0.03, $P = 0.10$; 25 – 49 Hz, 0.01 to 0.01, $P = 0.92$; 52 – 100 Hz, 0.07 to 0.03, $P = 0.12$).

significantly for the two lowest frequency bands, and (data not shown). This is in agreement with the low-pass filtering properties of neuronal membranes. However, phase concentration does not show significant increases across any of the frequency bands (fig.2.9). This result is intuitive since membrane potentials aren't used for communication between neurons or neuronal groups.

2.5 Discussion

This study is a comprehensive assessment of neuronal oscillations of turtle V1 cortex in terms of their power, duration, peak frequency, and phase. Results indicate that a huge variability exists among electrodes and trials. This can be attributed to the information processing happening in underlying neuronal circuits and the state of the cortex at that time. A large variability can be seen from stimulus-to-stimulus as well (data not shown). Huge variability seen in duration and peak frequencies disallows straightforward functional roles for oscillations. Phase drift in oscillations adds to this complexity and, hence, makes our interpretations more difficult. Delightfully, coherency increases at the onset of stimulus that justifies the possibility of neuronal oscillations involve in information transmission from one region to the other. This increase in coherency, along with power, gives us clues on deciphering functional roles of oscillations in the brain.

2.5.1 How oscillations are generated?

The simplest mechanism that can generate oscillations in any frequency band of LFPs is a network of cells rhythmically firing at that frequency. However, experimental works suggest that neurons fire irregularly [25, 65] and sparsely [65, 66, 115] even when oscillations are present in LFP signals of the network. Theoreticians showed that auto-coherent oscillations emerge in a population of inhibitory neurons [36, 37]. These early models indicated that recurrent interaction among inhibitory cells is the key underlying mechanism for the emergence of oscillations [57]. Numerous models included both excitatory

and inhibitory cells have been proposed for generating oscillations especially in gamma bands [52,74,79,116].

2.5.2 Oscillations are variable in duration and frequency

Its very well known that a network of neurons activated generates, intrinsically, rhythmic oscillations [117, 118], which has shown to vary considerably between recording sites [119–122]. Large stimulus-dependent variability in frequency agrees with computational models [54, 123]. Now it is the time to answer the question that what impact, if any, these oscillations can have on the activity of neuronal groups and modulate their responses. As stated earlier, if oscillations were used for timing, not only its duration should be long enough, but also its peak frequency should be approximately constant. To examine peak frequency variability, continuous LFP and V_m recordings were used to calculate relative power across trials (fig.2.2 and fig.2.3) and its profile is characterized (fig.2.4C and fig.2.5C). The same analysis has been done for burst durations (fig.2.4 and fig.2.5A, B). Distributions were diverse with some recurrent features showing up for some recording sites.

2.5.3 Phase drift in oscillations

Oscillations are always modelled such that their phase expands linearly with time like a pure sinusoid signal. To test this assumption, we did a time-frequency analysis of the recorded voltage traces using wavelet decomposition. Our observation indicates that phase evolution of the signal does not obey a linear dependence in time and it's rather more complicated. This observation, per se, calls into question the properties of a "clock"

signal during visual stimulation. However, two points worth mentioning. First of all, temporally unstructured dynamics could be resolved on shorter time scales of 100 ms on which gamma oscillations could be a clock signal. Second, analysis doesn't reject the possibility of low frequency rhythms to be auto-coherent and being used as a universal reference time. This raises a very important question that what are the functional roles of gamma-band oscillations? Moreover, what approaches should be taken to evaluate functional roles of oscillations in general?

2.5.4 Communication through coherence

During past two decades a surge of research on oscillations has happened on how cortical oscillations may contribute to cognitive functions [124–126]. One hypothesis for the role of neural oscillations is the concept of phase coding [95, 127, 128]. This hypothesis states that timing of spikes with respect to the phase of an ongoing network oscillation carries information about the presented stimulus. Another essential role has been conceived for a rhythmic oscillation is being a clock signal [2, 28, 94]. In this view, communication through coherence theory, brain uses oscillations for precise temporal encoding and for this purpose phase of the oscillations should be conserved during evoked response [2,10]. Communication through coherence is based on the realization that oscillations modulate neuronal excitability and therefore provide a window of opportunity for the sending group to have a large impact on the target neurons [2]. This makes frequency match of oscillatory activity incredibly critical and, hence, leaving communication impossible if frequencies in different areas are too disparate. This is because the relationship between excitable periods in different populations of neurons would vary over time. There exist a

very rich literature suggesting that, despite lack of regularity, oscillations have shown co-variance among remote neuronal groups [10,82,96,99,100,103,129–131]. This in principle means the existence of an active frequency-matching mechanism in the cortex. Our data demonstrate, as well, that stimulus presentation resets the phase of ongoing oscillations and boost the "predictability" of the activity in neuronal populations. Needless to say, power enhancement makes oscillations more perceivable to remote neuronal groups.

Some studies, on the other hand, show that gamma-band activity is a stochastic process and too random to serve as a clock signal for synchronizing brain regions over the length of the stimulus [105,108,111]. Their experimental results [105] indicate that gamma activity has an identical temporal structure in both awake and anesthetized monkeys and their modeling results, in line with others [132], suggest that gamma-band dynamics could be replicated in a recurrent network with Poisson-distributed inputs and is unlikely to be a reference time. To resolve this old-standing controversy and evaluate the importance of oscillations in neuronal circuit, a real-time analysis should be taken while controlling the occurrence of them [133]. Using this approach while the animal is performing a task, roles of oscillations can be explored.

ACKNOWLEDGMENTS

We thank members of the Neurophysics Laboratory for useful discussions. Wavelet software was provided by C. Torrence and G. Compo, and is available at URL:
http://paos.colorado.edu/research/wavelets/

AUTHOR CONTRIBUTIONS

W.C., J.P., W.S., and R.W. performed the experiments. J.P. and M.H. analyzed the data. M.H. performed the model simulations, M.H., J.P., and R.W. wrote the paper.

GRANTS

This research was supported by a Whitehall Foundation grant no. 20121221 and a NSF CRCNS grant no. 1308159 to R. Wessel.

DISCLOSURES

No conflicts of interest, financial or otherwise, are declared by the authors.

Chapter 3

Coherent and intermittent ensemble oscillations emerge from networks of irregular spiking neurons

This work has been published in Journal of Neurophysiology:

Mahmood S. Hoseini, Ralf Wessel .

Department of Physics Campus Box 1105 Washington University St. Louis Missouri 63130-4899 USA

Published 1 January 2016 Vol. 115 no. 1, 457-469 DOI: 10.1152/jn.00578.2015

3.1 Abstract

Local field potential (LFP) recordings from spatially distant cortical circuits reveal episodes of coherent gamma oscillations that are intermittent, and of variable peak frequency and duration. Concurrently, single neuron spiking remains largely irregular and of low rate. The underlying potential mechanisms of this emergent network activity have long been debated. Here we reproduce such intermittent ensemble oscillations in a model network, consisting of excitatory and inhibitory model neurons with the characteristics of regular-spiking (RS) pyramidal neurons, and fast-spiking (FS) and low-threshold spiking (LTS) interneurons. We find that fluctuations in the external inputs trigger reciprocally connected and irregularly spiking RS and FS neurons in episodes of ensemble oscillations, which are terminated by the recruitment of the LTS population with concurrent accumulation of inhibitory conductance in both RS and FS neurons. The model qualitatively reproduces experimentally observed phase drift, oscillation episode duration distributions, variation in the peak frequency, and the concurrent irregular single-neuron spiking at low rate. Furthermore, consistent with previous experimental studies using optogenetic manipulation, periodic activation of FS, but not RS, model neurons causes enhancement of gamma oscillations. In addition, increasing the coupling between two model networks from low to high reveals a transition from independent intermittent oscillations to coherent intermittent oscillations. In conclusion, the model network suggests biologically plausible mechanisms for the generation of episodes of coherent intermittent ensemble oscillations with irregular spiking neurons in cortical circuits.

3.2 Introduction

LOCAL FIELD POTENTIAL (LFP) recordings from cortical tissue have long revealed short epochs of periodic voltage fluctuations [31, 65]. Such recorded voltage fluctuations reflect the superposition of synchronized oscillatory local extracellular currents from spiking neurons and/or synaptic inputs within the recording volume determined by the LFP reach [134, 135].

The LFP oscillations are ubiquitous across different cortical areas, species, and behavioral and cognitive context [3, 136–138]. Despite this diversity in origin, cortical LFP oscillations tend to share four commonly observed features. First, for the population of neurons located within the LFP recording volume of an electrode, single neuron spiking is sparse (i.e., firing rate is smaller than oscillation frequency) [139–142] and irregular, both during epochs of oscillations and in the absence of oscillations [25]. Second, throughout an epoch of elevated spectral power, the phase of the oscillation is not conserved, i.e., not autocoherent [108, 111]. Third, the duration and the power spectral density (PSD) distribution of LFP oscillations vary from epoch to epoch [65, 105], as well as for different conditions of sensory stimulation [115, 143, 144]. Fourth, the fluctuating aspects of LFP oscillations covary across spatially separate cortical recording sites [82].

The ubiquity of LFP oscillations raises the question as to what these mesoscopic emergent phenomena reveal about the underlying cortical microcircuits. In other words, what combination of biophysical ingredients of a model network can generate the four common features of emergent cortical oscillations? Numerous network models of varying levels of complexity have reproduced subsets of the listed four features of cortical LFP oscillations [134, 145, 146]. For instance, detailed model networks of irregularly and sparsely

spiking neurons generated oscillations [52, 74, 75, 79]. However, these important investigations did not address intermittency and autocoherence. At a higher level of abstraction, a recurrent network consisting of one excitatory and one inhibitory node generated intermittent oscillations of variable durations and peak frequencies [105], but, by design of a rate model, these investigations did not speak to the nature of neuronal spiking. To the best of our knowledge, despite the vast literature on the mechanisms of cortical oscillations [11], no computational model has captured simultaneously the four important features of observed cortical oscillations, i.e., irregular and sparse spiking, phase drift, epoch-to-epoch variations, and coherence across multiple networks.

Here, we propose underlying mechanisms for cortical oscillations that explain all observed features simultaneously. To this end, we investigated a model network consisting of regular-spiking (RS) pyramidal neurons, fast-spiking (FS) interneurons, low-threshold spiking (LTS) interneurons, and stochastic external inputs. With the use of biologically plausible parameters, the model network spontaneously generated intermittent epochs of activity oscillations with evolving phase, while model neurons spiked sparsely and irregularly. Durations and peak frequencies varied from epoch to epoch, but covaried for two networks with sufficient coupling.

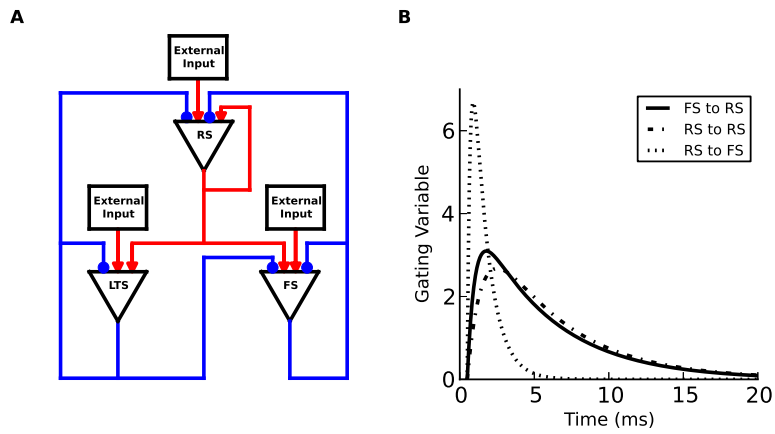

Figure 3.1: **Model network with recurrent connections and synaptic dynamics.** A: schematic representation of network structure. Each regular-spiking (RS) and low-threshold spiking (LTS) neuron can connect to all other neurons. In contrast, fast-spiking (FS) neurons can inhibit RS and FS but not LTS neurons. B: gating variable dynamics for three selected synapses. They are normalized in such a way that the area under the curve equals the membrane time constant.

Table 3.1: Neuron and network properties

Parameter	Description	Value
V_{leak}	Leakage reversal potential	-70 mV
V_{thr}	Threshold membrane potential	-59 mV
V_{reset}	Reset membrane potential	-70 mV
V_E	Excitation reversal potential	0 mV
V_I	Inhibition reversal potential	-80 mV
τ^E_{ref}	RS refractory time	2 ms
τ^I_{ref}	FS and LTS refractory time	1 ms
τ_l	Delay time constant	0.5 ms
τ^E_m	Excitatory membrane time constant	20 ms
τ^I_m	Inhibitory membrane time constant	10 ms
C_E	Excitatory membrane capacitance	0.2 nF
C_I	Inhibitory membrane capacitance	0.1 nF
dt	Simulation time step	0.05 ms
Δt	Time bin size	0.5 ms
N_{RS}	Number of RS pyramidals	2000
N_{FS}	Number of FS pyramidals	250
N_{LTS}	Number of LTS pyramidals	250
P_c	Connection probability	0.2

Table 3.2: Synaptic parameters

Synaptic conductances (nS)			
post- \ pre-	RS	FS	LTS
RS	0.25	3.80	3.80
FS	0.30	4.00	4.00
LTS	0.30	0.0	4.00
Rise time constant (ms)			
post- \ pre-	RS	FS	LTS
RS	1.0	0.5	5.0
FS	0.2	0.5	5.0
LTS	0.2	-	5.0
Decay time constant (ms)			
post- \ pre-	RS	FS	LTS
RS	5	5	50
FS	1	5	50
LTS	1	-	50
Leakage conductance (nS)			
	10	12.5	20

3.3 Materials and methods

3.3.1 Model Network

We consider a model network of 2,000 RS pyramidal neurons, 250 FS interneurons, 250 LTS interneurons and external inputs (fig.3.1A). The network structure resembles cortical feedback triads [147]. Specifically, each RS and LTS neuron can connect to all other neurons. In contrast, FS neurons can connect to other RS and FS neurons, but not to LTS neurons [148]. The main differences between the two groups of interneurons, besides projecting to different targets, are 1) LTS neurons operate on much longer time

scales [148–150], and 2) LTS neurons tend not to spike as frequently as FS neurons, since they need coordinated input from RS cells [151, 152]. We implemented these distinctions through different synaptic time constants and leak conductances. Of the possible connections, constrained by the network structure, a subset of connections is chosen with probability, P_c, thus generating a network with sparse and random connectivity. As a result, each model neuron obtains on average 400 excitatory and 100 inhibitory connections from within the network. In addition, each neuron has 800 excitatory connections from private external inputs with a given total firing rate [52]. Membrane potentials and action potentials of model neurons of each type are simulated as leaky integrate-and-fire neurons, with the subthreshold dynamics of the membrane potential V_i of neuron i given by $C\frac{dV_i(t)}{dt} = I_{ext} + I_{leak} + I_{syn}$, where C is the membrane capacitance, $I_{leak} = g_{leak}(V - V_{leak})$ is the leak current (g_{leak} is leak conductance), and $I_{syn} = g_{syn}S(t)(V - V_{syn})$ is the synaptic current due to excitatory and inhibitory inputs from within the network (g_{syn} is synaptic conductance and S is the gating variable) (Table3.1). The external excitatory input, I_{ext}, is conductance based and has the same dynamics as the excitatory synapses of connections within the network. The synaptic gating variable $S(t) = [\tau_m/(\tau_d - \tau_r)](exp[-(t - \tau_l)/\tau_d] - exp[-(t - \tau_l)/\tau_r])$ describes the time course of synaptic conductance change (fig.3.1B). The normalization constant ensures that the time integral of the synaptic gating variable equals the membrane time constant, and thus varying the synaptic time constant does not affect the time integral of the synaptic current. This normalization ensures the balance of excitation and inhibition. When the membrane potential of a neuron exceeds a threshold, the neuron fires an action potential, and the membrane potential resets and stays at the rest value for duration of the refractory period. The spike train of neuron i is given by the time series $\eta_i(t)$. The numerical values in Table3.2 are matched with experimental values for synaptic time scales [153–157] and

conductances [158, 159]. A model neuron receives external inputs with total firing rate of 6 and 8 kHz to RS and FS/LTS neurons. This external input can be delivered using a different number of synaptic connections.

Considering 800 excitatory synaptic inputs makes each synapse to deliver an independent Poisson pulse train with mean rate of 7.5 Hz for RS and 10 Hz for FS and LTS neurons. For simplicity, the Poisson to Binomial distribution approximation is used. Synaptic conductance for external inputs is 1.75 nS for RS and 2.0 nS for FS and LTS neurons. All model parameters are defined, and their values are given in Table3.1 and 3.2. Simulations were performed using Eulers method with a time step of 0.05 ms. Simulations were carried out for 4 s in real time unless stated otherwise.

3.3.2 Analysis of Simulation Results

Single-neuron spike trains. The sparseness of spiking is evaluated by comparing the distribution of single-neuron mean firing rates with the dominant frequency of the oscillation. The irregularity of spiking is evaluated via the interspike interval (ISI) distribution of the spike trains $\eta_i(t)$. For a Poisson pulse train we expect an exponential decay of the ISI distribution (for ISIs larger than the refractory period) and a coefficient of variation (CV) with a value near one. The CV is defined as the SD divided by the mean ISI. For a bursting spike train, the CV can be larger than one because of two completely different time scales present in the spike train. In contrast, a regular spike train has a CV value near zero.

Synchrony. To quantify the level of synchrony among the spike trains $\eta_i(t)$ within the model network we bin the time, $\Delta t = 0.5$ ms. From the spike train of neuron i, we get the instantaneous firing rate $r_i(t)$, i.e., the number of spikes within a time bin divided

by the bin size. From this, the network instantaneous firing rate is $r(t) = \Sigma_{i=1}^{N} r_i(t)$. Operationally, this quantity is derived by summing the number of spikes from all neurons within a time bin. We then compare the variance $var[r(t)/N]$ of the network instantaneous firing rate normalized by the network size against the population-averaged variance $\frac{1}{N}\Sigma_{i=1}^{N} var[r_i(t)]$ of the variance of instantaneous firing rates from individual spike trains [160,161]. Thus, we define the synchrony measure

$$\kappa^2(N) = \frac{var[\frac{r(t)}{N}]}{\frac{1}{N}\Sigma_{i=1}^{N} var[r_i(t)]} \tag{3.1}$$

For fully synchronous spike trains this measure equals one and is independent of network size. In contrast, for asynchronous spike trains, $\kappa(N)$ takes on values between zero and one and, importantly, varies linearly with the inverse of the square root of the network size, $\kappa(N) \sim \kappa(\infty) + \frac{\alpha}{\sqrt{N}}$ where α is a constant [162].

Oscillations. We evaluate the level of oscillations in the network activity from the PSD via Fourier transform of the network instantaneous firing rate. Calculations are performed using the multitaper method [98,163]. In general, time bins, Δt, must be much larger than the simulation time steps and much smaller than the period of the oscillations in network activity. Results are robust for time bins between 0.5 and 2 ms. To identify an episode of oscillation in network instantaneous firing rate signal, we first took the points in the time-frequency space that have at least one-half of the maximum power at any frequency between 20 and 100 Hz. Among these, points are accepted that are above three times the SD of a 5-Hz frequency band around it. Now neighboring points form an epoch. This procedure allows us to estimate the time duration and peak frequency of an oscillation episode.

Autocoherence. Complementary to evaluating the amplitude of a frequency component, it is informative to evaluate its residual phase, which is the difference between the phase of the analyzed frequency component and the phase of a pure sinusoidal function of the same frequency. To obtain the phase of the analyzed frequency component, the network instantaneous firing rate $r(t)$ is convolved with a Gabor filter

$$\psi(t;\tau,f) = \frac{1}{\sigma\sqrt{2\pi}} e^{-\frac{(t-\tau)^2}{2\sigma^2}} e^{-j2\pi ft} \tag{3.2}$$

and the resulting function is Fourier transformed (j is the square root of -1 not an index)

$$G_x(t,f) = \int_{-\infty}^{\infty} d\tau x(\tau)\psi(\tau - t, f) = R(t,f)e^{j\phi(t,f)} \tag{3.3}$$

This continuous Gabor transform [164] yields the amplitude $R(\tau, f)$ and the phase $\phi(\tau, f)$ of the network instantaneous firing rate $r(t)$ in each time-frequency point. The circular variation

$$CiV(f) = 1 - |\frac{\Sigma_t R(t,f)e^{j\phi(t,f)}}{\Sigma_t R(t,f)}| \tag{3.4}$$

where phase residual $\phi_r(\tau, f)$ is the difference between phase of the signal and phase of a pure sinusoidal signal with that frequency, $\phi_r(\tau, f) = \phi(\tau, f) - \phi_{sinusoidal}(\tau, f)$ where $\phi_{sinusoidal}(\tau, f) = 2\pi f mod[\tau, (1/f)]$. As an example, complex Gabor transform of a pure sinusoidal (autocoherent) signal results in a circle trajectory phase portrait. Time evolution of the signal manifest itself in the circular counterclockwise rotation of the state on that circle around the origin. Subtracting $\phi_{sinusoidal}$, which corresponds to a clockwise rotation in the reference coordinate, will result in one single point in the phase space as expected, since we started with an autocoherent signal. Circular variation (CiV) quantifies the localization of the residual phase in the phase portrait and is a criterion for the degree

of autocoherence of that frequency component [165]. The values of CiV are bounded by zero and one, with zero for the most coherent oscillation (pure sinusoidal) and one for random signals [108].

3.4 Results

3.4.1 Overview

To gain insight into what combination of cellular and/or circuit mechanisms can generate cortical oscillations, we investigated a model network motivated by cortical neurons, synapses, and circuits. Here we focus on four important features of experimentally observed cortical oscillations: irregular and sparse spiking, intermittent network oscillations with phase drift, epoch-to-epoch variations in network oscillations, and coherence across multiple networks. The model network consists of 2,000 RS excitatory neurons, 250 FS interneurons, 250 LTS interneurons, and excitatory external inputs (fig.3.1A). Connectivity is sparse and random (see Materials and methods) such that each model neuron receives on average 400 excitatory and 100 inhibitory connections from within the network, plus 800 excitatory connections from private external inputs. Each external input is simulated as an independent Poisson pulse train with mean rate of 7.5 Hz to pyramidal neurons and 10 Hz to interneurons.

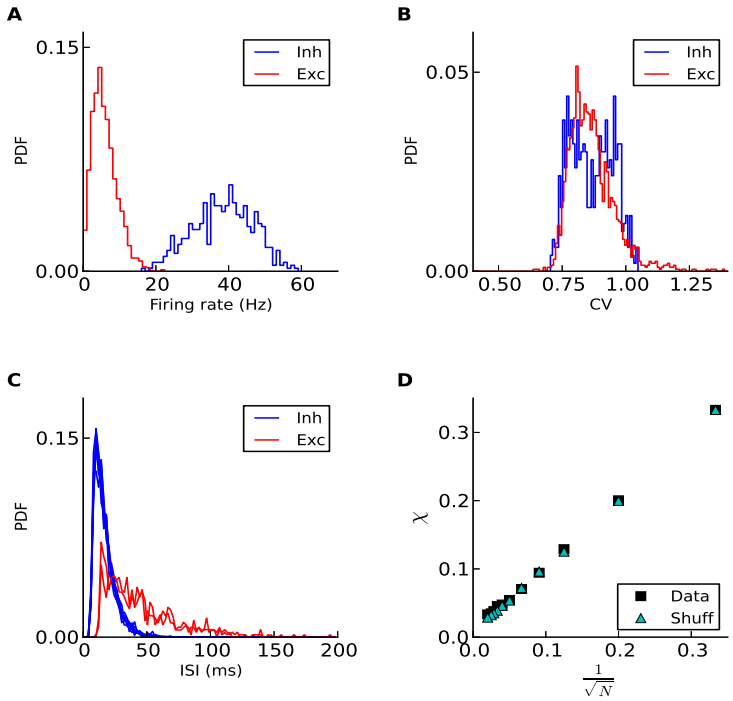

Figure 3.2: **Spiking is irregular and asynchronous on average.** A: distribution of time-averaged firing rates for excitatory (red) and inhibitory (blue) neurons. For clarity, the distributions of inhibitory LTS and FS neurons are merged. Average firing rates are 6 Hz for RS, 23 Hz for LTS, and 34 Hz for FS neurons. B: distribution of coefficients of variation (CVs) for excitatory (red) and inhibitory (red) neurons. The mean CVs are 0.80 for RS and 0.81 for LTS and FS neurons combined. C: interspike interval (ISI) distributions for a few excitatory (red) and inhibitory (blue) neurons on the right tail of time-averaged mean rate distribution in A. D: synchrony measure $\kappa(N)$ as a function of network size N. The linear increase with the inverse of the square root of the network size indicates the asynchrony of individual spike trains.

3.4.2 Single-Neuron Spiking is Sparse, Irregular, and Asynchronous

In response to the continuing external stochastic inputs and the inputs from the resulting spiking activity of other neurons from within the network, all neurons spike sparsely and irregularly (fig.3.2 and fig.3.3A). Time-averaged firing rates vary from neuron to neuron. Firing rates are distributed within the range of ~ 1 and 20 Hz ($mean = 6$ Hz; $maximum = 25$ Hz) for RS excitatory neurons, whereas firing rates for inhibitory neurons range from ~ 10 to 50 Hz ($mean = 23$ Hz for LTS and 34 Hz for FS; $maximum = 50$ Hz) (fig.3.2A).

The CV values are distributed around slightly below one (fig.3.2B). The interspike interval distributions for all neurons decay approximately exponentially (fig.3.2C), as expected for Poisson pulse trains, thus indicating irregular spiking. To evaluate the level of correlation among the spike trains, we use the synchrony measure $\kappa(N)$ (see Materials and methods). This measure is defined as the ratio of the variance of the population-averaged instantaneous firing rate and the average variance of the instantaneous firing rates from individual spike trains. Simulated spike trains in our model yield values of $\kappa(N) < 1$ and, importantly, scale with network size according to $\kappa(N) \sim \kappa(\infty) + \frac{\alpha}{\sqrt{N}}$ (fig.3.2D). Both observations are characteristics of asynchronous spiking. This conclusion is further corroborated by the similarity of the results for network spike trains and shuffled spike trains. It is important to note, however, that the synchrony measure $\kappa(N)$ is a time-averaged (total simulation time) measure and thus does not speak to transient correlations among spike trains.

3.4.3 Network Oscillations Are Intermittent

To evaluate the possibility of transient epochs of oscillations, we looked beyond the individual spike trains $\eta_i(t)$ (fig.3.3A) and analyzed the network instantaneous firing rate. Unlike the individual spike trains, this measure of network activity reveals significant oscillatory temporal structure (fig.3.3B). A time-resolved Fourier transform (see Materials and methods) reveals elevated power in narrow frequency bands for short periods of time (fig.3.3C). Importantly, however, spiking remains sparse. Even at the highest peak in network instantaneous firing rate near 70 Hz, $< 5\%$ of the neurons spiked during a given time bin (0.5 ms). Thus, visual inspection of a subset of spike trains (fig.3.3A) offers little information about epochs of network oscillations.

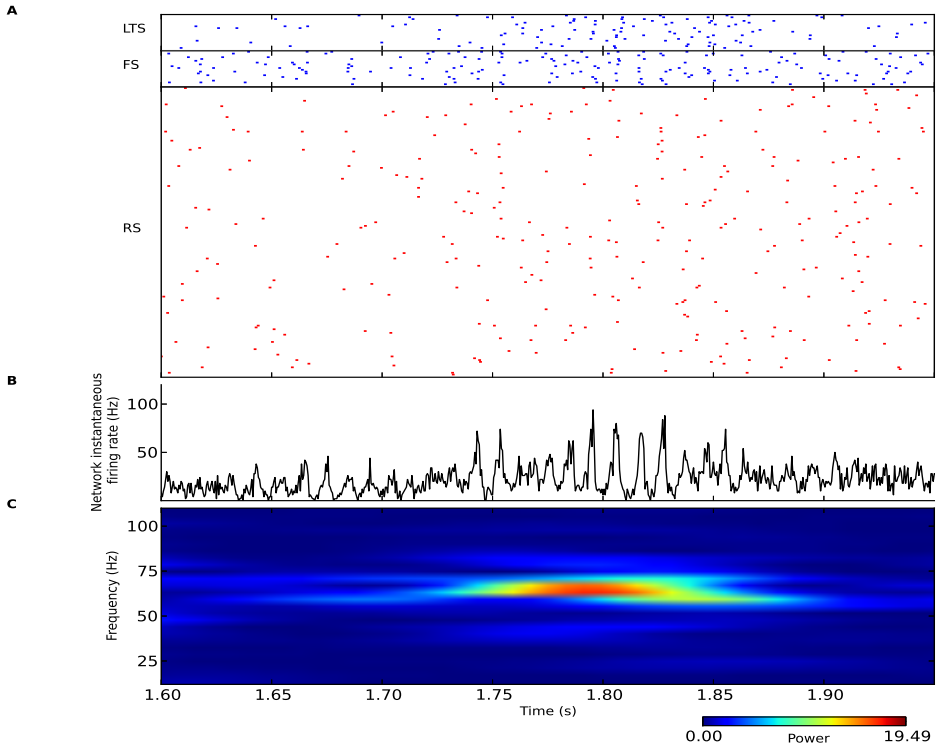

Figure 3.3: **Irregular asynchronous spiking is consistent with intermittent oscillations of network activity** A: raster plots of spikes for 160 RS, 20 FS, and 20 LTS neurons, respectively. Irregular spiking for all three types of neurons is apparent by visual inspection. B: network instantaneous firing rate $r(t) = \Sigma_{i=1}^{N} r_i(t)$ reveals oscillations in this continuous variable. An episode of oscillation starts at around 1.75 s and lasts for about 100 ms. C: power spectrum of the network instantaneous firing rate shows an episode of elevated power between 1.75 and 1.85 s in time and around 70 Hz in frequency.

In contrast, the network instantaneous firing rates for the RS and FS populations of neurons (fast time scale), and the dynamics of inhibitory synaptic conductance (slow time scale), are informative about the underlying mechanisms of the population dynamics (fig.3.4). Qualitatively, the intermittent oscillations of network activity arise through the following sequence of biophysical interactions. First, stochastic fluctuations in the spike

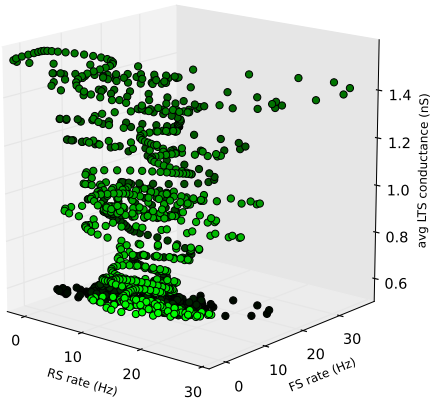

Figure 3.4: **Dynamics of intermittent oscillations represented in three continuous model variables.** A fluctuation in external inputs (data not shown) increases the RS and FS population-averaged instantaneous firing rates (dark green). The recurrent interaction between RS and FS neurons mediates oscillations. The coordinated activity of RS neurons activates LTS neurons. Because of the long decay of LTS synaptic conductances in other neurons, the population-averaged conductance accumulates. This accumulation causes a decline in RS and FS activity, which in turn terminates the oscillatory RS and FS activity. The vanishing coordinated activity in RS neurons causes a decline in LTS activity (light green). In this parametric plot the state of the network at a certain time is represented by a dot within 3-dimensional space spanned by the 150-Hz low-pass-filtered RS and FS instantaneous firing rates and the population- averaged LTS conductance in all neurons. Dots are plotted for 500 ms with time increments of $\Delta t = 0.5$ ms. Time increases from dark green to light green.

occurrence of the external inputs to the RS and FS neurons activate these groups of neurons. Second, from the thus transiently increased RS/FS activity and the recurrent interaction between RS/FS neurons, an oscillation in network activity emerges. Third, the increased synchrony of RS excitatory inputs to LTS neurons causes an increased activity of this group of inhibitory neurons during the oscillation. Fourth, the long synaptic decay time (50 ms) of LTS inhibitory synaptic conductances (fig.3.1B) causes a gradual build-up of inhibitory synaptic conductances in all neurons. Fifth, the increasing inhibitory synaptic conductance has two biophysical effects: 1) all membrane potentials drift closer to the inhibitory reversal potential of -80 mV and away from the spiking threshold of -59

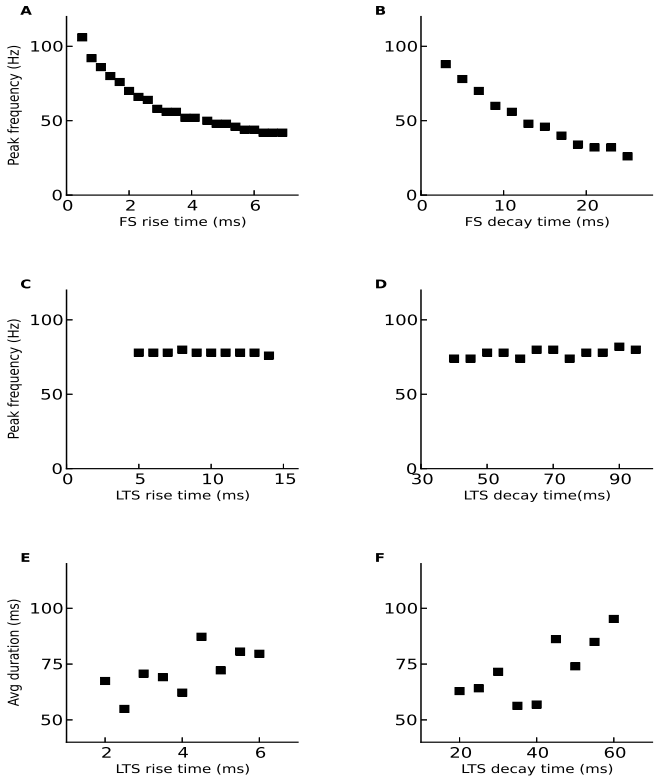

Figure 3.5: **Dependence of oscillations on synaptic time constants.** A and B: peak frequency decreases with increasing FS rise time and with increasing decay time. For time constants used in this work see Table3.2, except $\tau_{rise}^{FS} = 1.5$ ms in B. C and D: LTS synaptic time constants do not impact peak frequency. Parameters are based on Table3.2, except $\tau_{rise}^{FS} = 1.5$ ms. E and F: average duration of oscillation epochs increases with increasing LTS rise time and decay time.

mV; and 2) all effective membrane time constants decrease. Sixth, both effects reduce the spiking probabilities in all neurons and thus terminate the epoch of network oscillation.

Consistent with this description of mechanisms, the oscillation peak frequency decreases with increasing FS synaptic rise or decay time constant (fig.3.5A and fig.3.5B), whereas LTS synaptic rise and decay time constants do not impact the oscillation peak frequency (fig.3.5C and fig.3.5D). However, LTS biophysical parameters determine the duration of

oscillatory epochs (fig.3.5E and fig.3.5F). LTS decay time impacts the duration of episodes in the following way. Synaptic current is defined by $I_{syn} = g_{syn}S(t)(V - V_{syn})$, where the gating variable, S(t) (see Materials and methods), includes the normalization constant, $\tau_m/(\tau_d - \tau_r)$, which is chosen so that the time integral of the gating variable is equal to the membrane time constant [52]. This normalization was adopted to keep the balance between excitation and inhibition. Varying the synaptic time constants does not affect the time integral of a postsynaptic current but reduces the peak postsynaptic current. Thus, increasing synaptic time constants of LTS neurons, either τ_r or τ_d, reduces the LTS peak postsynaptic current. Therefore, more spikes in LTS are needed to terminate oscillations. Thus increasing synaptic time constants of LTS neurons leads to longer-lasting oscillations.

3.4.4 The Phase Drifts Within an Epoch of Oscillation

The stochastic nature of the generation of network oscillations in this model raises the question whether a resulting epoch of network oscillation resembles a sinusoid with a fixed phase. To address this question, we employed the continuous Gabor transform (see Materials and methods) to evaluate the difference between the phase of the analyzed frequency component and the phase of a pure sinusoidal function of the same frequency. We use CiV to quantify the localization of residual phase in the phase portrait. The CiV is a measure for the degree of phase drift of that frequency component, with zero for the most coherent oscillation (pure sinusoidal) and one for signals with random phase. For all epochs of network oscillations tested, phase portrait trajectories for given frequency bands between 20 and 100 Hz fill out the space with a significant nonzero CiV (fig.3.6).

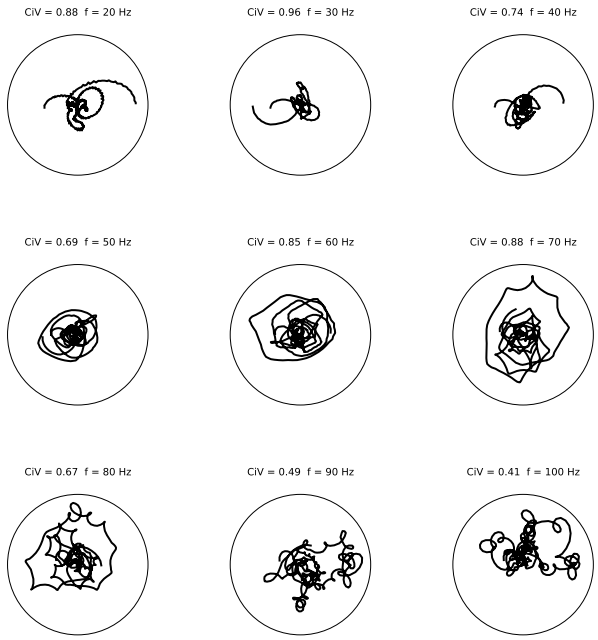

Figure 3.6: **The phase is not constant within an epoch of oscillation.** Displayed are phase portraits of one oscillation epoch for frequencies in the gamma range (20 – 100 Hz). The oscillation epoch had a peak frequency of 70 Hz and a duration of 200 ms. A phase portrait for a given frequency value is a parametric plot of the residual phase (represented by the angle) and the amplitude (radius) at consecutive points in time (parameter). Circular variation (CiV) is a measure for the degree of phase drift of that frequency component. The CiV values and the given frequency are shown above each graph. For comparison, a perfect sine wave at the given frequency would result in a point on this graph and a vanishing CiV value. In contrast, signals with a random phase result in a CiV value of 1.

This observation indicates that, over the time window of a given epoch of network oscillation, the phase is not constant. The network oscillation is not autocoherent.

3.4.5 Epochs of Oscillations Are Variable

To what extent do the features of network oscillations vary from epoch to epoch? This question too is motivated by the stochastic nature of network oscillation generation. To address this question, we detected epochs of oscillations in a long simulation (60 s) and

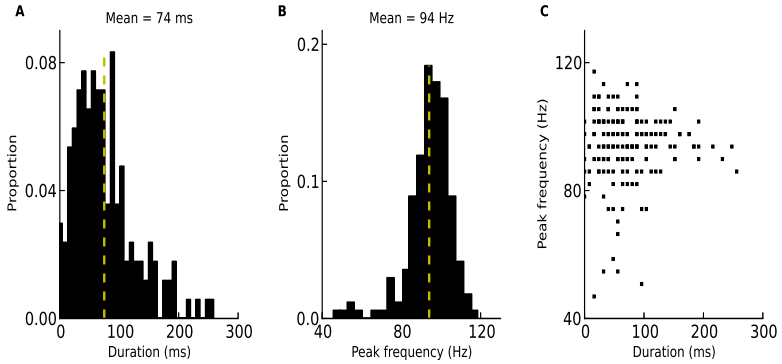

Figure 3.7: **Epochs of oscillations vary in duration and peak frequency.** A: epoch durations are distributed around 74 ± 51 ms (mean $\pm$ SD; the mean is indicated by the vertical yellow broken line). B: epoch peak frequencies are distributed around 94 ± 11 Hz (mean $\pm$ SD). C: epoch peak frequency and duration are unrelated. Values for a total number of 200 epochs are shown.

characterized each epoch in terms of its duration and peak frequency (see Materials and methods). For the model parameters chosen, the epoch durations are normally distributed with a mean of 74 ms (fig.3.7A). The duration distribution depends on LTS biophysical parameters (fig.3.5E and fig.3.5F). The peak frequencies are normally distributed around a mean of 94 Hz (fig.3.7B). As described above (fig.3.5A and fig.3.5B), peak frequencies depend on the FS synaptic rise or decay time constants. Epoch duration and peak frequency of network oscillations are not correlated (fig.3.7C).

3.4.6 The Role of FS Neurons in Rhythmogenesis

The recurrent interaction between RS and FS neurons has long been thought to be the core mechanism for the generation of network oscillations [36, 116, 166, 167]. To evaluate the role of each neuron type in this model (fig.3.1A), we stimulated RS or FS neurons through a 40% decrease in their leak conductance (pulses with 0.5- and 5-ms rise and decay time) repeated at regular intervals of 8 or 40 Hz frequency (fig.3.8A). First, we verified that this level of leak conductance modulation is sufficient to cause a corresponding increase in the

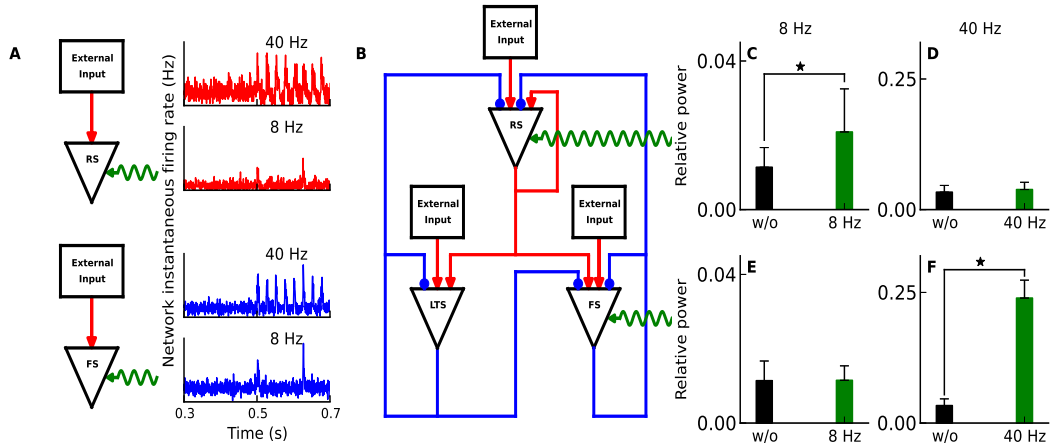

Figure 3.8: **The role of RS/FS neurons in network rhythmogenesis.** A: alpha function leak conductance modulation pulses with 0.5- and 5-ms rise and decay times modulate network spontaneous firing rate of uncoupled networks. B: schematic representation of the periodic leak conductance modulation of RS and FS neurons. C: low-frequency modulation of RS cells causes a significant relative power increase ($P = 0.002$) in a 4-Hz frequency band around stimulation frequency, 8 Hz. To compute the power we use multitaper power spectral density with 3 tapers, 500-ms time window sliding by 50 ms. Relative power in the given frequency is defined as the ratio of power in a 4-Hz frequency range around the given frequency to the total power from 0 to 100 Hz. Black bar is for no modulation case (baseline), and green is in the presence of periodic modulation. Error bars are calculated over 25 repetitions of the simulation. D: 40 Hz modulation of RS neurons does not have a significant ($P = 0.23$) impact of the relative power at high frequencies centered around 40 Hz. E: low-frequency leak conductance modulation of FS interneurons does not cause a significant ($P = 0.91$) change in relative power around 8 Hz. F: stimulating FS neurons at gamma-band frequencies significantly ($P \ll 0.01$) increases relative power in gamma-band frequencies. *Significant difference between two bars or values.

network instantaneous firing rate in isolated RS and FS neurons (fig.3.8A). We then evaluated the impact of the imposed leak conductance modulation on network activity in the network with all possible connections intact (fig.3.8B). Modulating RS leak conductance at 8 Hz caused a small, but significant ($P = 0.002$; 2-sample t-test distribution), increase in network activity in the 6- to 10-Hz frequency band (fig.3.8C). Modulation of RS leak conductance at 40 Hz had no significant effect ($P = 0.23$) on network activity in the 38- to 42-Hz frequency band (fig.3.8D). Qualitatively, the modulation-induced correlated RS activity triggers LTS spiking, which, in turn, produces extended inhibition (50 ms decay

time) of both RS and FS neurons. As a result, the LTS inhibition largely suppresses the drive-evoked RS spiking response. Modulating FS leak conductance, in contrast, evokes a different set of biophysical mechanisms. Periodic modulation of FS leak conductance at 8 Hz has little effect ($P = 0.91$) on the network activity in the 6- to 10-Hz range (fig.3.8E). With the short decay time (5 ms) of FS inhibition, the impact of FS inhibition on RS spiking is much shorter than the period of modulation (120 ms), thus leaving most of the RS spiking to be dominated by stochastic external input. The situation changes for 40-Hz modulation of FS leak conductance. This rate of modulation significantly ($P \ll 0.01$) increased the power of the network activity in the 36- to 42-Hz range (fig.3.8F). Qualitatively, at 40 Hz modulation and with the decay time (5 ms) of FS inhibition, the external input-evoked RS spiking undergoes sinusoidal fluctuations. This observation highlights the impact of periodic FS activity on network rhythmogenesis.

3.4.7 Coherent Oscillations Emerge Dynamically in Coupled Networks

As described above, the stochastic nature of rhythmogenesis causes fluctuations in occurrence, phase, duration, and frequency content of oscillation episodes. Such fluctuations raise the question to what extent intermittent oscillations in two networks covary. To address this question, we constructed two identical networks but with independent external inputs and varied the coupling between the two networks (fig.3.9A).

Within each network, of all possible connections, con- strained by the network structure (fig.3.1A), a subset of connections is chosen with probability, $P_c = 0.2$. This procedure generates sparse and random connectivity within each network. Parameters are tuned

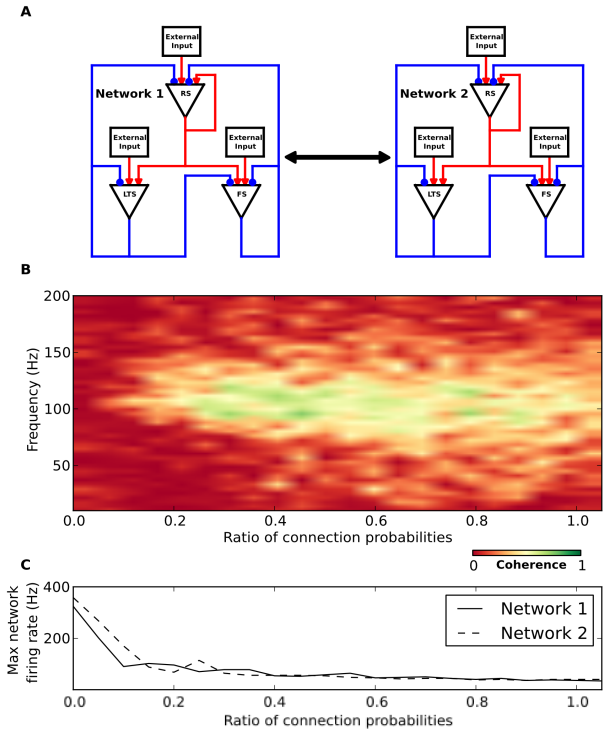

Figure 3.9: **Oscillations covary in networks with modest coupling.** A: schematic representation of two networks with all possible connections and internetwork coupling. Internetwork coupling is similar to intranetwork connection, but with different connection probability. B: coherence plot between two networks as a function of frequency and the ratio of inter- to intranetwork probabilities for a 4-s simulation. C: maximum amplitude of network instantaneous firing rate as a function of the ratio of inter- to intranetwork probabilities.

(fig.3.5A and fig.3.5B) so that each network generates intermittent oscillations at frequencies around 100 Hz. Coupling between the two networks is constrained by the same rules of the network structure. A subset of connections between the two networks is chosen from the possible connections with internetwork probability that ranges from 0 to 0.2. The coupling between the two networks, quantified as the ratio of inter- to intranetwork connection probability, ranges from zero (two independent networks of 2,500 neurons each) to one (one network of 5,000 neurons).

As expected, in uncoupled networks local activity fluctuations within each network trigger independent episodes of ensemble oscillations resulting in vanishing coherence values, which were calculated over the 4-s simulation time (fig.3.9B). However, a small increase in the coupling between the two networks causes a sharp rise in the coherence of the two network activities in the frequency range around 100 Hz. This is despite the fact that the two networks receive independent external inputs. In conclusion, coherent oscillations emerge dynamically in two networks with modest reciprocal coupling. Above some intermediate coupling, the coherence decreases with increasing coupling. This is because, in our model, inhibitory (FS and LTS) neurons have a larger time-averaged firing rate than excitatory (RS) neurons (fig.3.2A). Thus the coupling between the two networks decreases the overall excitation-to-inhibition ratio, which in turn decreases the overall network activity (fig.3.9C) and thus reduces coherence.

3.5 Discussion

In this model investigation we have shown that intermittent ensemble oscillations can arise from the interaction of excitatory RS and inhibitory FS and LTS neurons, while single neuron spiking remains largely irregular and sparse. The recurrent interaction between the RS and FS neurons provides a generative mechanism of oscillation. Periodic activation of FS, but not RS, model neurons causes enhancement of gamma oscillations. The emerging correlated RS spiking during an oscillation activates LTS neurons. The long LTS synaptic decay time causes an accumulation of inhibitory synaptic conductances in all neurons, which eventually terminates the ensemble oscillation. The stochastic nature of ensemble oscillation causes a phase drift during an epoch of oscillation, and a large

variability in durations and peak frequencies from epoch to epoch. Importantly, however, oscillations largely covary for two networks with sufficient coupling.

3.5.1 Discrete and Continuous Variables Interact in the Network

The dichotomy between discrete irregular single-neuron spiking and continuous network activity lies at the core of cortical oscillations [52, 74, 75]. First, the firing rate of individual neurons is typically much smaller than the dominant oscillation frequency [5, 65, 66, 115]. Second, discrete spike events are transformed into continuous variables, such as the synaptic gating variable and the membrane potential. Third, the continuous variables determine the probability of single-neuron spiking. Fourth, in a large population of neurons, the probability of single-neuron spiking translates into network instantaneous firing rates. In conclusion, at the level of continuous variables, the network dynamic is fully described within the three-dimensional state space spanned by the instantaneous firing rates of RS, FS neurons, and LTS-mediated slow inhibitory conductances in all neurons (fig.3.4).

3.5.2 Fast Negative Feedback Generates Oscillations

The biophysical mechanisms of sparse pyramidal neuron spiking during gamma oscillation have been explored in recent studies emphasizing the role of spike frequency adaptation and global inhibition [168] as well as shunting inhibition [169, 170]. Pharmacological blockade of inhibition disrupts oscillations [36, 116, 166, 167, 171, 172]. Our model results (fig.3.8F) corroborate the need for inhibition in rhythmogenesis and further predict how the FS synaptic rise and decay time constants impact the oscillation frequency (fig.3.5A

and fig.3.5B). The oscillation of the continuous variables is, however, the result of the convolution of discrete and stochastic spike events. The stochastic nature of rhythmogenesis results in phase drifts during an epoch of oscillation (fig.3.6). In other words, the phase of an oscillation is not conserved during the elevated power of an oscillation. This lack of autocoherence has been observed in LFP recordings from primary visual cortex of monkeys [105,108]. In addition, the stochastic nature of rhythmogenesis results in a large epoch-to-epoch variability in peak frequencies (fig.3.7B), largely similar to the variability examined in primary visual cortex [105].

Optogenetic manipulation of barrel cortex in vivo showed that light-driven periodic (40-Hz) activation of FS neurons amplifies oscillations in the gamma range, whereas similar activation of RS had no such effect [92]. Our model reproduces this experimental observation (fig.3.8D and fig.3.8F) and thus, consistent with investigations of a more complex model [173], emphasizes the role of FS neurons in rhythmogenesis.

3.5.3 Slow Negative Feedback Terminates Oscillations

Synchronous RS activity during an oscillation recruits LTS neurons, and their slowly accumulating inhibition eventually terminates the oscillation (fig.3.4). Because of the underlying stochastic spiking, accumulation of activity too is stochastic, which translates into a distribution of oscillation epoch durations (fig.3.7A). Such duration variability is qualitatively similar to what has been observed in primary visual cortex [105]. On average, the duration of an oscillation epoch increases with increasing LTS synaptic time constants (fig.3.5E and fig.3.5F). With biologically plausible LTS synaptic time constants, the model generated oscillation durations of up to a few hundred milliseconds (fig.3.7A). Because

the network stops fulfilling all four features for very large LTS synaptic time constants, additional mechanisms would have to be explored for longer durations. Importantly, our model makes the experimentally testable prediction that optogenetic activation of LTS neurons after the onset of an oscillation will shorten the duration of that oscillation epoch.

Finally, our model investigation raises an important question about the FS and LTS connectivity (fig.3.1A). Our simulations show that, in the presence of FS-to-LTS connections of sufficient strength, spontaneously started oscillations continue indefinitely, while the peak frequency distribution remains largely unchanged (data not shown). The qualitative change in network behavior from intermittent to continuous as a function of FS-to-LTS synaptic conductance occurs within a narrow range between 4.0 nS (intermittent oscillations) and 4.7 nS (continuous oscillations).

The key mechanisms of oscillation termination are the accumulation of activity and the resulting negative feedback. The LTS neurons are but one biophysical implementation of the termination mechanism. Alternatively, oscillation termination can be accomplished by nonlinear transfer functions [174], possibly implemented by the nonlinear properties of dendrites and synapses [175,176]. Memmesheimer [174] has shown that incorporating supralinear dendritic enhancement of synchronous inputs leads to the generation of intermittent sharp-wave ripples (200 Hz). This poses the question for future studies whether coexistence of these two mechanisms, slow inhibition and nonlinear transfer function, renders intermittent oscillations more robust. The model presented here shows that intermittency can arise due to the network structure rather than single-neuron property. However, the model is not robust. Intermittent oscillations arise from small volumes within the multidimensional parameter space.

For completeness, we discuss two important features of network models with nonlinear components, robustness and degeneracy. First, an exhaustive scan of the $\sim$ 25-dimensional parameter space is computationally extremely expensive and is beyond the scope of the present paper. Nevertheless, network behavior is robust with respect to small variations of connection probability (from 30% up to 50%) and synaptic conductances for AMPA and GABA channels ($\sim$ 10% around the values given in Table3.2). Second, the fact that, in networks with nonlinear elements multiple combinations of parameters can give rise to the same output, is well established in network theory and nonlinear dynamics, was introduced in neuroscience with a detailed model simulation [177], and received further intellectual support in the analytic investigation of a simple model [147]. An exhaustive scan of the parameter space in search for degeneracy is beyond the scope of this manuscript.

3.5.4 Oscillations Covary for Coupled Networks

The stochastic nature of rhythmogenesis and the resulting variability in phase, peak frequency, and duration raise questions as to the potential coordination of oscillations across multiple networks. Regardless of the observed variability and the fact that phase does not unfold linearly with extended time, it is thought crucial for two networks to be able to offset differences in oscillation frequencies. In this manner, networks can initiate and maintain oscillations as communication means between distant neuronal groups [2,80–83]. We have shown that oscillations between distant regions remain robustly coordinated despite significant variations in their internal dynamics. Our results indicate that a wide range of frequencies could be exploited as mechanisms for information transmission between two networks with recurrent connections during perceptual and cognitive processing.

3.5.5 Simulating Important Features of Cortical Oscillations

Numerous previous theoretical investigations have offered physical intuition about individual aspects of rhythmogenesis in cortical circuits [36, 79, 173, 178–180]. Here we highlight selected examples. 1) A spiking model was designed to generate ensemble oscillations in the presence of irregular and sparse spiking, but did not reproduce the intermittency of rhythms [52]. 2) Another spiking model included spike timing-dependent plasticity and displayed the transition between different frequency bands [181]. However, the degree of synchronization of spikes during network oscillations was inconsistent with the experimentally observed irregular and sparse spiking. 3) Clustered connections have been proposed to generate slow dynamics and high variability in a network of spiking neurons [182]. This model, however, does not reproduce intermittent ensemble oscillations with variable peak frequencies. 4) electroencephalogram (EEG) model net- works (not spiking) generate intermittent oscillations [105, 183–186]. However, by design (not spiking), these EEG models do not speak to irregular and sparse spiking.

In contrast, the spiking model proposed here, for the first time, reproduces five important features of observed cortical oscillations: 1) irregular and sparse spiking, 2) phase drift during an epoch of oscillation, 3) intermittent oscillations, 4) epoch-to-epoch variations in peak frequency and duration, and 5) coherence across multiple networks.

In addition, the model makes two testable predictions. First, our model predicts a lack of connections from FS to LTS neurons. Experimental observations in hippocampus [148, 187] support this prediction. In cortex, the connectivity from FS to LTS neurons could be tested experimentally in the following two ways: 1) search for physiological connections via dual whole cell recordings in a slice of cortex and 2) search for anatomical connections

via electron microscopic survey (connectomics) of a piece of cortical tissue. Second, the model predicts that optogenetic hyperpolarization of LTS neurons would transform oscillations from intermittent to more continuous. This experiment could be refined by triggering the optogenetic manipulation of LTS neurons on a detected oscillation (for online oscillation detection, see, for instance, [133]). The prediction is that oscillation-triggered hyperpolarization of LTS neurons would increase oscillation episode duration, whereas oscilla- tion-triggered depolarization of LTS neurons would decrease oscillation episode duration.

ACKNOWLEDGMENTS

We thank members of the Neurophysics Laboratory for useful discussions.

GRANTS

This research was supported by a Whitehall Foundation Grant no. 20121221 and National Science Foundation CRCNS Grant no. 1308159 to R. Wessel.

DISCLOSURES

No conflicts of interest, financial or otherwise, are declared by the authors.

AUTHOR CONTRIBUTIONS

Author contributions: M.S.H. and R.W. conception and design of research; M.S.H. analyzed data; M.S.H. prepared figures; M.S.H. drafted manuscript; M.S.H. and R.W. edited and revised manuscript; M.S.H. and R.W. approved final version of manuscript.

Chapter 4

Adaptation modulates correlated response variability in visual cortex

This work has been submitted to Nature Communications:

Nathaniel C. Wright, Mahmood S. Hoseini, Ralf Wessel.

Department of Physics Campus Box 1105 Washington University St. Louis Missouri 63130-4899 USA

4.1 Abstract

Cortical sensory responses are highly variable. This variability can be correlated across neurons (due to some combination of dense intracortical connectivity, cortical activity level, and cortical state), with fundamental implications for population coding. Yet the interpretation of correlated response variability (or noise correlation) has remained fraught with difficulty, in part because of the restriction to extracellular neuronal spike recordings. Here, we measured response variability and its correlation at the most microscopic level of electrical neural activity, the membrane potential, by obtaining dual whole-cell recordings from pairs of cortical pyramidal neurons during visual processing. We found that during visual stimulation, correlated variability adapts towards an intermediate level and that this correlation dynamic is mediated by intracortical mechanisms. A model network with external inputs, synaptic depression, and structure reproduced the observed dynamics of correlated variability. These results establish that intracortical adaptation self-organizes cortical circuits towards a balanced regime at which network coordination maintains an intermediate level.

4.2 Introduction

Sensory cortex is not simply one layer in a feedforward network; it receives strong inputs from thalamus, but intracortical feedback dominates cortical circuitry (fig.4.1a). This tangle of cortical connections causes neural activity to be coordinated across multiple spatial and temporal scales [188, 189]. Moreover, in a given cortical network, the strength of this coordination can vary with activity level and network state [84, 190–194], which is

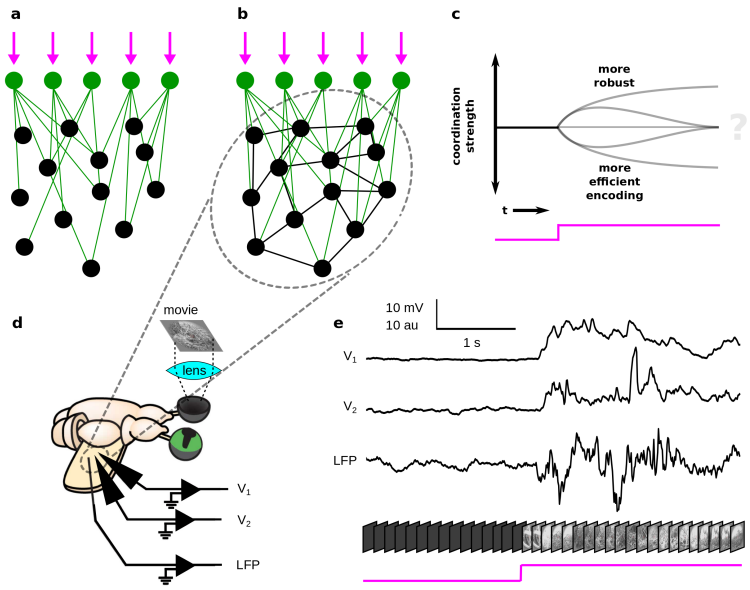

Figure 4.1: **Investigating the dynamics of correlated variability in recurrent circuits of visual cortex.** (a) Feedforward thalamocortical network subject to sensory inputs (magenta). Coordination between pairs of cortical neurons (black) is determined by convergence patterns in thalamic inputs (green). (b) A more realistic, interaction-dominated thalamocortical network, in which the inputs to any one cortical neuron arise primarily from other cortical neurons. Coordination is thus a function of both feedforward and recurrent inputs. (c) The level of cortical coordination affects cortical function, and it is unknown if and how this changes with sensory stimulation. (d) We simultaneously recorded the membrane potentials from pairs of cells, as well as the nearby LFP, during ongoing and visually-evoked activity in a densely-interconnected thalamocortical network. (e) Pairwise membrane potential recordings provided a measure of cortical coordination across stimulus conditions that avoids the pitfalls of spike data.

considered to have implications for cortical function [195–198]. For example, weak coordination corresponds to a larger library of words available to the spatiotemporal code, while stronger coordination supports signal propagation (fig.4.1c). The realized level of coordination in active cortical circuits is expected to represent a balance between such competing system needs. Two unanswered questions concerning coordination continue to block our path to understanding sensory processing in cerebral cortex. First, what are the levels of cortical coordination during sensory processing, and to what extent do these levels change with varying stimulus conditions (fig.4.1c)? Second, what mechanisms are responsible for the realized level of cortical coordination and its changes?

Recording the spike trains from pairs of neurons for repeated presentations of an identical stimulus and evaluating the level of correlated response variability (or noise correlation) has remained the work horse of investigating cortical coordination (see [84, 199] for reviews). This spike-based approach is popular in part because of the relative ease of obtaining spiking responses from pairs of neurons in intact brains. Reported values of spike-based noise correlation tend to be significantly nonzero, but results have varied across studies [84, 191, 199–201]. Furthermore, the interpretation of cortical coordination from spike data is littered with complications, including a spike-rate dependence of noise correlation values [199, 202], the underrepresentation of sparse-spiking neurons, and possible biases introduced by the spike-sorting process [199, 203]. In conclusion, the important study of cortical coordination, including its relation to mechanisms and function, has been restricted by its focus on spike recordings, and continues to represent an unmet challenge in systems neuroscience.

In response to this need, we investigated the dynamics of correlated response variability at the level of the membrane potential by obtaining dual whole-cell recordings from pairs of cortical pyramidal neurons during visual processing (fig.4.1d), e. We found a high level of trial-to- trial membrane potential response variability. Further, correlated variability in the gamma band range of membrane potential fluctuations increased at stimulus onset, but returned to pre-stimulus values during continued visual stimulation. A brief visual stimulus, triggering persistent cortical activity, elicited a similar dynamic of correlated variability, thus implicating an intracortical mechanism. A model network with small-world connectivity, external inputs, and synaptic depression reproduced the observed dynamics of correlated variability, and further indicated that network oscillations play a crucial role. Taken together, these results establish adaptation towards an intermediate

level of coordination as a fundamental principle of cortical organization during visual processing.

4.3 Results

To quantify response variability and its correlation across neurons, we recorded the membrane potential (V) from 19 pairs of pyramidal neurons in visual cortex of the turtle ex vivo eye-attached whole-brain preparation during visual stimulation of the retina (fig.4.1d). Ongoing activity in turtle visual cortex was largely quiet. In contrast, visual stimuli evoked barrages of postsynaptic potentials in cortical pyramidal neurons that were accompanied by extensive fluctuations in the nearby local field potential recording (fig.4.1e), indicating strong concurrent network activity.

4.3.1 Pyramidal neuron membrane potential visual responses are highly variable

Single-neuron membrane potential responses to repeated movie presentations varied from trial to trial, with a response variability magnitude that exceeded the trial-averaged mean response (fig.4.2a). Importantly, the magnitude of the response variability was qualitatively unchanged when the visual stimulus consisted of brief flashes, which evoked long-lasting responses in visual cortex (fig.4.2b). This stimulus invariance of the trial-to-trial response variability indicates an intra-thalamocortical origin of the network activity and the resulting membrane potential fluctuations.

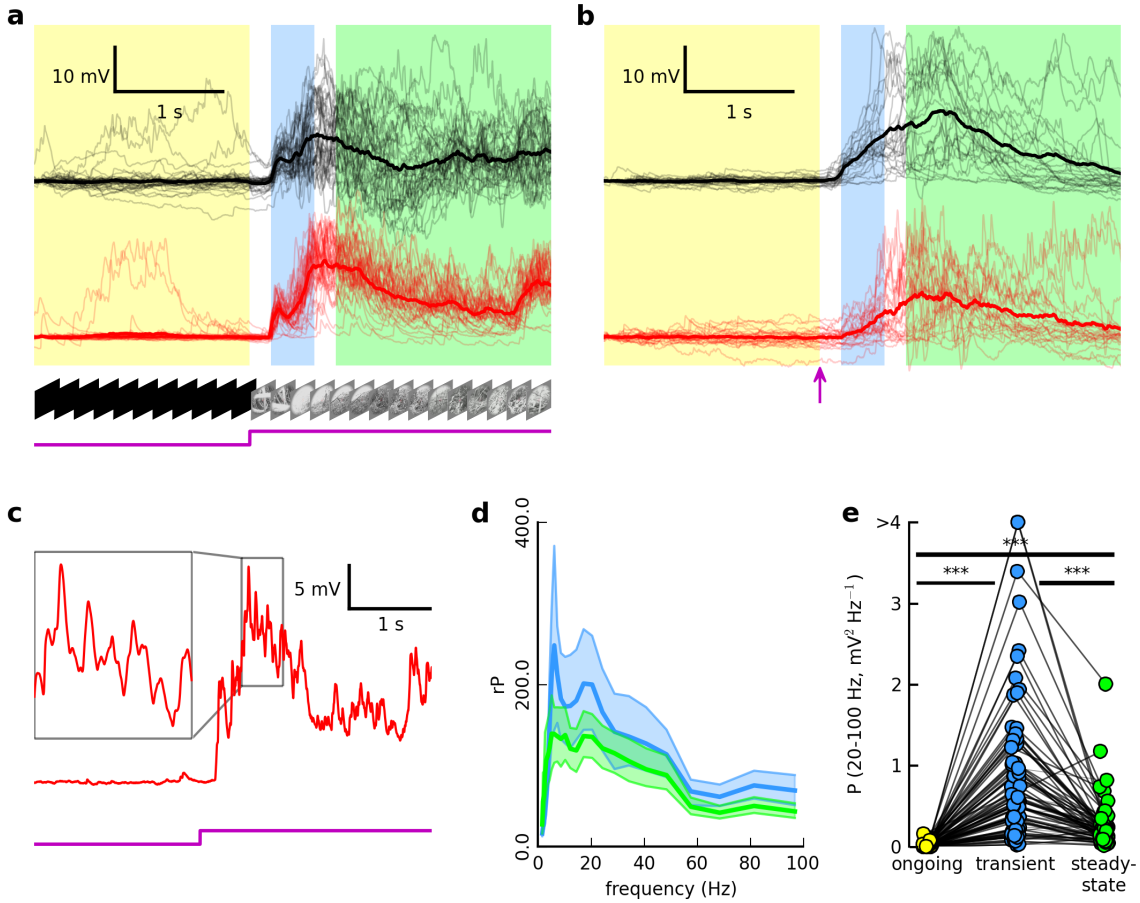

Figure 4.2: **Dynamics and complexity of trial-to-trial response variability.** (a) Single-trial responses (low opacity) and across-trial average responses (high opacity) for two simultaneously-recorded neurons. Stimulus is naturalistic movie (see Methods). Single trials artificially aligned for clarity. (b) Same as in (a), but for a different pair of cells, and stimulus is 150 ms red (640 nm) whole-field flash, with onset at magenta arrow, (see Methods). (c) Single-trial response from cell in (a). Inset: high-frequency activity nested within the broader depolarization. (d) Average relative power spectrum (evoked power divided by ongoing) of residuals for red traces in (a) for the transient (blue) and steady-state (green) epochs. Shaded regions indicate ±95% confidence intervals by bootstrapping method. (e) Trial-averaged gamma (20 – 100 Hz) power for each of 37 pairs. Each dot represents the across-trial average gamma power for one pair for that epoch. Dark (light) lines connecting dots represent (in)significant changes in gamma power for that pair across epochs. Across-epoch significance for each pair determined by comparing bootstrap intervals. Asterisks above line connecting two epochs indicates results of Wilcoxon signed-rank significance test for difference in populations of values for those epochs (**: $0.001 < P < 0.01$; ***: $P < 0.001$; no asterisk and gray line: $P > 0.05$). Two outliers truncated for clarity.

For any given trial of visual stimulation, the evoked membrane potential fluctuations were large and consisted of high-frequency fluctuations nested within broader deflections (fig.4.2c). To quantify the frequency content of the response fluctuations we first calculated the membrane potential residual (V_r), which is the single-trial membrane potential recording from which the trial-averaged membrane potential time series has been subtracted. We then divided the evoked residuals into two analysis windows: the transient (200 to 600 ms after stimulus onset) and steady-state (800 to 2800 ms after stimulus onset) windows (Supplementary Information 1). Finally, we calculated the relative power spectral density (rP), which is the power spectral density of the membrane potential residual for the transient or steady-state window divided by its trial-averaged counterpart from the ongoing window (2 s prior to stimulus onset).

This analysis revealed four important features concerning the spectral content of the residual membrane potential fluctuations and of the trial-to-trial response variability. First, evoked power of residual membrane potential fluctuations in the 0.1 to 100 Hz range typically increased by two orders of magnitude compared to ongoing activity (fig.4.2d, fig.S4.2). Second, the frequency content of the membrane potential residual varied across trials (as indicated by the broad confidence bands in (fig.4.2d). Third, the relative power spectral density typically consisted of a prominent peak located approximately in the 4 to 10 Hz theta range and a broader, but distinct, distribution in the 20 to 100 Hz gamma range. Fourth, for both movies and flashes, gamma power increased from the ongoing to the transient window, and significantly decreased from transient to steady-state (fig.4.2e). Gamma power of the transient activity varied drastically across cells.

Together, these data establish that cortical pyramidal neuron membrane potential visual responses (i) have complex temporal dynamics, (ii) are highly variable from trial to trial, and (iii) differ from neuron to neuron (fig.4.2).

4.3.2 Correlated variability adapts during visual stimulation

The complex and extensive variability of membrane potential visual responses (fig.4.2) and the interconnected nature of cortical circuits (fig.4.1b) raised the question to what extent the response variability is correlated across pyramidal neurons. To address this question, we calculated the Pearson correlation coefficient between residual membrane potential fluctuations for each trial and window of interest, i.e., the ongoing, transient, and steady-state windows. We focused on gamma-band (20 – 100 Hz) activity, which captures the fast, nested membrane potential fluctuations (fig.4.2c, inset; fig.4.3a), and see Supplementary Information 2). This band of activity is thought to be associated with narrow windows of opportunity for spiking, determining the precise timing of spikes within a broader depolarization (see [204] for a review). Trial-averaged correlation coefficients (CC) for ongoing activity were broadly distributed across pairs of pyramidal neurons (fig.4.3b), and the population average ($\langle CC \rangle$) was significantly nonzero ($\langle CC \rangle = 0.03$, $P = 0.006$, one-sided t-test). During the transient period (200 to 600 ms after movie onset) trial-averaged correlation coefficients increased significantly compared to ongoing values (fig.4.3b), to an elevated population average of $\langle CC \rangle = 0.11$ ($P = 2.9e-4$ for ongoing–transient comparison, Wilcoxon signed-rank test). In the steady-state period, i.e., during continued movie presentation, trial-averaged correlation coefficients returned to near-ongoing values ($\langle CC \rangle = 0.041$, $P = 1.6e-4$ for transient–steady-state comparison, $P > 0.05$ for ongoing–steady-state comparison).

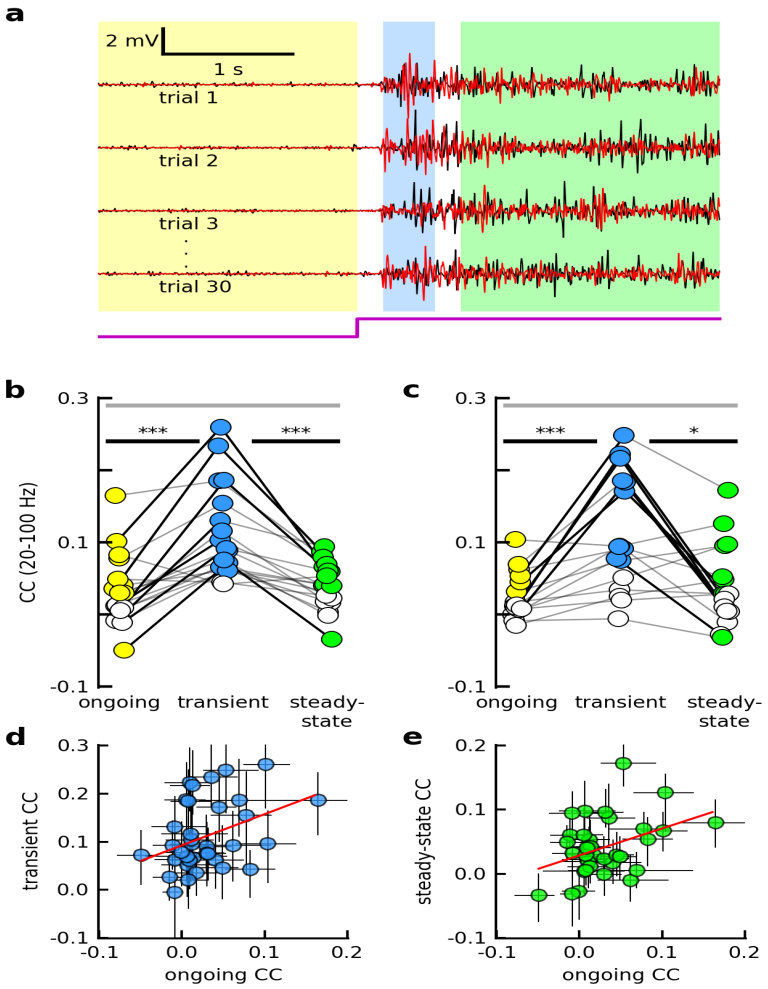

Figure 4.3: **Evoked gamma band correlated variability appeared to be modulated by internal mechanisms.** (a) Examples of gamma band (20 - 100 Hz) residual membrane potential pairs for several trials (same pair as in (fig.4.2a)). (b) Trial-averaged CC values for each of 22 pairs, 20 - 100 Hz, extended visual stimulation (see Methods). Each dot represents the across-trial average CC value for one pair for that epoch. Colored (white) dots represent values (not) significantly different from zero (one-sided t-test). Otherwise, same as in (fig.4.2e). (c) Same as in (b), but for 17 pairs, and brief visual stimulation (see Methods). The population-average CC was significantly nonzero during all epochs ($\langle CC \rangle = 0.029$, $P = 0.004$ ongoing, $\langle CC \rangle = 0.096$, $P = 3.44e-6$ transient, $\langle CC \rangle = 0.041$, $P = 1.50e-6$ steady-state, one-sided t-test), and increased significantly from the ongoing to transient epochs ($P = 0.001$ for ongoing-transient comparison, Wilcoxon signed-rank test), before relaxing to near ongoing values during the steady-state ($P = 0.002$ for transient–steady-state comparison, $P = 0.189$ for ongoing–steady-state comparison, Wilcoxon signed-rank test). (d) Across-trial average transient CC vs. average ongoing CC for each pair, for all stimuli. Error bars indicate 95% confidence intervals by bootstrapping method. Red line indicates significant linear regression fit ($r^2 = 0.10$, $P = 0.035$). (e) Same as (d), but for steady-state epoch ($r^2 = 0.15$, $P = 0.016$).

These results were largely robust with respect to choices of window sizes and gaps between windows (see Supplementary Information 1 and fig.S4.1). These changes in correlated variability primarily reflected changes in phase synchrony in the gamma band residual activity of simultaneously-recorded neurons (see Supplementary Information 3 and fig.S4.4). In contrast, low-frequency (0.1 – 20 Hz) CC values followed a different dynamic (fig.S4.3a, b) and were not significantly related to gamma-band CC (see Supplementary Information 2 and fig.S4.3c – e).

The observed dynamics of gamma band correlated variability in response to continuous visual stimulation could be imposed by the spatiotemporal structure of the stimulus, or alternatively, could be intrinsic to the thalamocortical system. To distinguish between these two hypotheses, we recorded from 16 pyramidal neuron pairs while presenting brief flashes (1 – 200 ms) of light, which evoked responses lasting several seconds in the visual cortex (fig.4.2b). We found that across the population of all pairs, CC values for responses to brief stimuli were not significantly different from those for extended stimuli ($P > 0.05$, Wilcoxon rank-sum test, for all epochs, see Supplementary Information 4, and fig.S4.5). Importantly, the same dynamics of correlated variability were observed for brief stimuli ($\langle CC \rangle = 0.03$, $P = 0.003$ ongoing, $\langle CC \rangle = 0.11$, $P = 3.0E^{-5}$ transient, $\langle CC \rangle = 0.041$, $P = 0.006$ steady-state, one-sided t-test; $P = 6.4E^{-4}$ for ongoing–transient comparison, $P = 0.020$ transient–steady-state comparison, $P > 0.05$ ongoing–steady-state comparison, Wilcoxon signed-rank test, (fig.4.3c). The similarity of the dynamics of correlated variability for brief and extended stimuli implicates a mechanism that is stimulus-invariant and likely to be intracortical in origin.

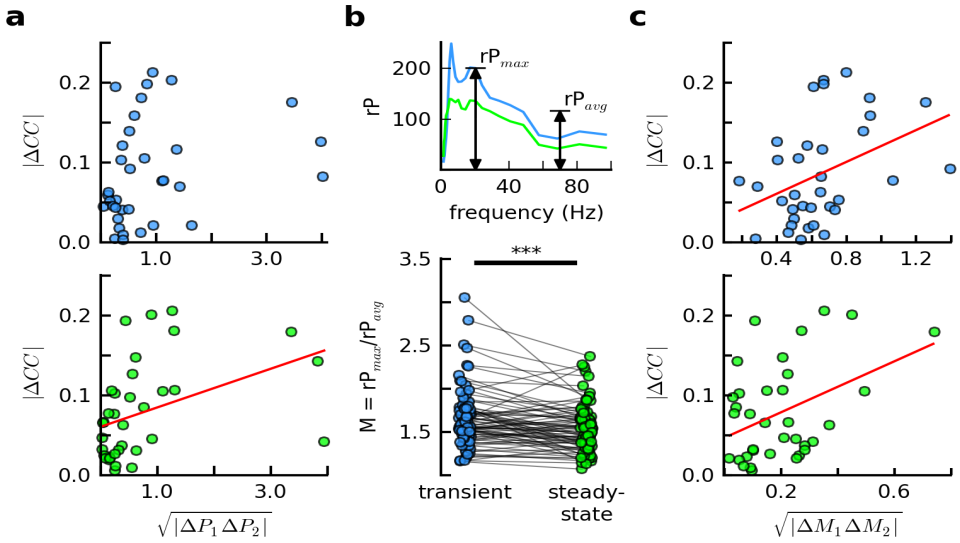

Figure 4.4: **Changes in CC are related to changes in the shape of relative power spectra.** (a) Absolute value of change in CC (evoked minus ongoing) vs. absolute value of geometric mean of change in gamma power, for each pair, for transient (top), and steady-state (bottom) epochs. (b) Top: same as in (fig.4.2d), but confidence bands omitted for clarity. For each cell, the peak power index (M), is defined as the maximum relative power value in the gamma range (rP_{max}), divided by the average over the gamma range (rP_{avg}). Bottom: M for all recorded cells (brief and continuous stimulation), for transient (blue) and steady-state (green) epochs. (c) Same as in (a), but for absolute value of geometric mean of change in M, for all cells. If present, red lines indicate significant linear regression fit ($P < 0.05$).

The evidence of an intracortical origin of correlated variability suggested to us that the correlated variability of ongoing activity for a given pair should be predictive of its correlated variability in response to visual stimulation. Indeed, we found that CC values during the ongoing epoch were significantly related to CC values for both evoked epochs ($r = 0.38$, $P = 0.03$, transient vs. ongoing, (fig.4.3d); $r = 0.39$, $P = 0.02$, steady-state vs. ongoing, (fig.4.3e), Pearson correlation). This observation suggests a close link between the underlying mechanisms that determine ongoing and evoked correlated variability, with connectivity being one candidate mechanism [205, 206].

4.3.3 Correlated variability is related to the network state

Recent experimental and computational work suggests that the level of coordination between pairs of neurons might be shaped not only by anatomical connectivity, but also by network activity level and network state [84, 190–194]. We therefore asked how well network activity level and/or network state could explain the observed dynamics of correlated variability.

As a proxy for network activity level, we inferred the level of presynaptic spiking activity using the average gamma power in residual membrane potentials. As a population, the gamma power dynamic (fig.4.2e) was qualitatively similar to that of CC (fig.4.3b), c. In contrast, for a given pair of cells, the geometric mean of the absolute change in power $\sqrt{|\Delta P_1|.|\Delta P_2|}$ was not related to the magnitude of the change in CC amplitude for the ongoing–to–transient transition ($r = 0.28$, $P = 0.10$, Pearson correlation). The two quantities were however related for the transient–to–steady-state transition ($r = 0.40$, $P = 0.017$, Pearson correlation) (fig.4.4b). In conclusion, changes in network activity levels alone did not fully explain the changes in gamma band correlated variability.

Next, we sought a measure of the network state. Specifically, we focused on the degree of action potential synchrony as an indicator of network state. Computational work has shown that synchronous network spiking can generate prominent subthreshold membrane potential fluctuations in a narrow frequency band [52]. Here, we used a measure of power spectrum peakiness in the 20 to 100 Hz range as a proxy for synchronous network spiking. The residual relative power spectra (rP) of some cells tended to contain peaks in the gamma band during the transient epoch, which were often smaller or absent in the steady-state (fig.4.2d, fig.S4.2). To quantify this aspect of the power spectrum for each

cell and epoch, we defined the quantity M as the ratio of the maximum relative power in the gamma range (rP_{max}) to the average relative gamma power (rP_{avg}) (fig.4.4b, top). Across the population of cells, M varied continuously, and the population average ($\langle M \rangle$) decreased significantly from transient to steady-state ($\langle M \rangle = 1.65$ transient, $\langle M \rangle = 1.54$ steady-state, $P = 2.2E^{-4}$ for transient–steady-state comparison) ((fig.4.4b), bottom). For the population of pairs, we found that the geometric mean of the absolute change in M, $\sqrt{|\Delta M_1|.|\Delta M_2|}$, was significantly related to the amplitude of the change in CC ($r = 0.40$, $P = 0.02$ ongoing–to–transient; $r = 0.41$, $P = 0.01$ transient–to–steady-state, Pearson correlation, where $\Delta M = M_{trans} - 1$ for the ongoing–transient transition) (fig.4.4c). In conclusion, for a given pair of cells, the change in network state, measured as a change in gamma spectrum peakiness, was a good indicator of the change in correlated variability.

4.3.4 Synaptic time constants, synaptic depression, and synaptic clustering together mediate the dynamics of correlated variability

What biophysical mechanisms could mediate the experimentally-observed response properties (i.e., across-trial variability (fig.4.2a, b), subthreshold gamma oscillations (fig.4.2c, fig.4.3a), the dynamics of correlated variability (fig.4.3) and its network state dependence (fig.4.4))? To address this question, we investigated a model network (see Methods) of 800 excitatory and 200 inhibitory leaky integrate-and-fire neurons, with Poisson process external inputs to all excitatory neurons (fig.4.5a). Excitatory-to-excitatory and excitatory-to-inhibitory connections had small-world connectivity, with 5% connection probability. Inhibitory-to-inhibitory and inhibitory-to-excitatory synapses were random, with 20% connection probability. An increase in the external input rate mimicked the stimulus. We

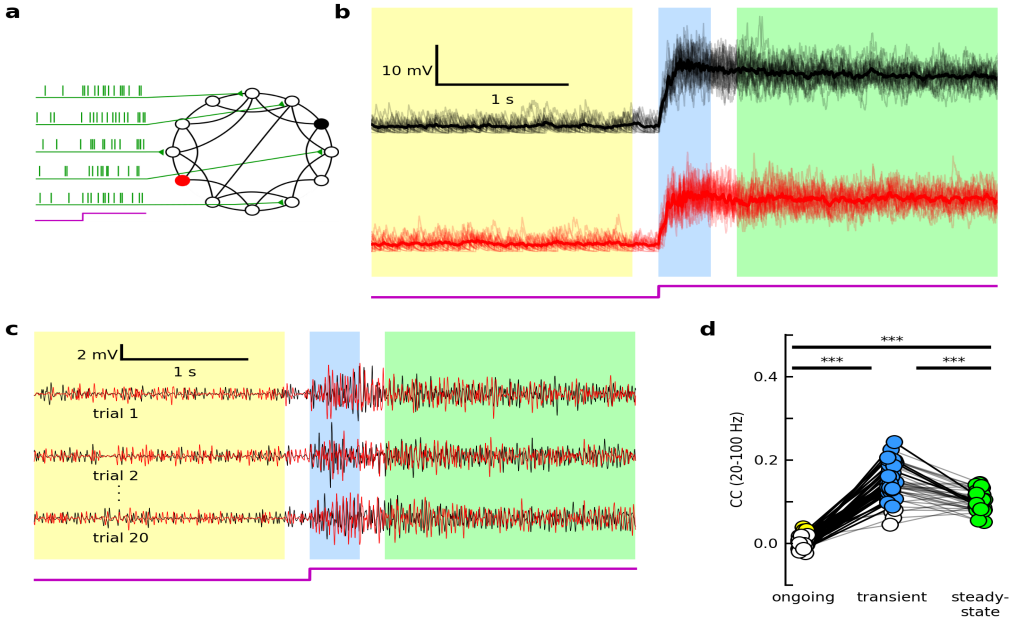

Figure 4.5: **A model network strengthens the internal mechanism hypothesis, suggesting crucial roles for network oscillations.** (a) The model network was composed of 800 excitatory LIF neurons with small-world connectivity, and 200 randomly-connected inhibitory LIF neurons (not depicted). All excitatory neurons received Poisson external inputs, and the stimulus was modeled as a gradual increase in the external input rate (see Methods). (b – c) Same as in fig.4.2b, c, but two excitatory model neurons randomly-selected from the network (see Methods). (d) Same as in fig.4.2d, but for forty pairs of excitatory neurons, generated from twenty neurons randomly-selected from the network.

selected a set of synaptic rise and decay times [11,52] that were consistent with gamma oscillations in the instantaneous network firing rate when the network was subject to strong external drive. Motivated by previous experiments (ref#21 in Shew et al. 2015) and models (ref#14 in Shew), we implemented adaptation via short-term synaptic depression with recovery (see Methods). Armed with this battery of mechanisms and structural complexity, we simulated the network spiking in response to repeated stimulus presentations (20 trials).

The model network reproduced the experimentally observed response variability and gamma oscillations. The simulated membrane potentials from randomly-selected excitatory model neurons revealed fluctuations and across-trial response variability (fig.4.5b) that were qualitatively similar to what we observed from recorded membrane potentials of pyramidal neurons (fig.4.2a, b). Furthermore, the gamma band residuals of simulated membrane potentials (fig.4.5c) largely resembled the experimentally-observed residual subthreshold gamma oscillations (fig.4.3a). Residual power spectra were peaked in the gamma range (fig.S4.6a, top), at frequencies that coincided with peaks in the spectra of the instantaneous network firing rate (fig.S4.6a, bottom). Due to synaptic depression with slow recovery, the model also reproduced the eventual decrease in the total gamma power in membrane potential residuals (fig.S4.6b), and in the amplitudes of gamma-band peaks in the residual membrane potential and population spike rate spectra (fig.S4.6a).

In addition, the model network reproduced the experimentally-observed dynamics of correlated variability. The simulated correlated variability increased significantly from ongoing to transient ($\langle CC \rangle = 0.003$ ongoing, 0.146 transient, $P = 3.6E^{-8}$ for ongoing–transient comparison) (fig.4.5d), a trend that was consistent with our experimental results (fig.4.3b), c. Furthermore, mediated by synaptic depression, correlated variability decreased significantly from transient to steady state ($\langle CC \rangle = 0.10$ steady-state, $P = 1.49E^{-6}$ for transient–steady-state comparison, $P = 3.6E^{-8}$ for ongoing–steady-state comparison) (fig.4.5d). In contrast, when synaptic depression was absent, correlated variability increased from transient to steady state (fig.S4.7a).

As observed in experiment, this dynamic of correlated variability depended crucially on network activity oscillations. When synaptic time constants for excitation and inhibition

were chosen to be identical (see Methods and Supplementary Information 5), the stimulus instead pushed the network into a regime of asynchronous activity, as evidenced by the population spike-rate and residual membrane potential power spectra (fig.S4.6c). This had little effect on the overall network activity level and gamma power dynamics (fig.S4.6d). Correlated variability, however, was very weakly modulated by the stimulus (fig.S4.7b), in contrast with our experimental results (fig.4.3b), c. This dependence on network oscillations had a synaptic basis: in the synchronous network, not only were correlations between synaptic conductances stronger than those in the asynchronous network, the lag between excitation and inhibition was larger, allowing for a longer window of opportunity for synaptic input correlations to be manifested in pairs of membrane potentials [84, 190] (fig.S4.8). In conclusion, changes in network oscillations, rather than network activity levels alone, determine the changes in correlated variability.

The network oscillation dynamic described here is not the only one capable of reproducing the experimentally-observed dynamics of correlated variability. For example, a similar randomly-connected network generates oscillations that either invade the entire network or are absent, and the CC dynamic can be reproduced by abolishing the oscillation early in the transient window via strong synaptic depression (data not shown). This oscillation dynamic is inconsistent with the experimental results, in which gamma oscillations were strongest during the transient epoch, but persisted in the steady-state (fig.4.3a, fig.4.4a, fig.S4.4a). In contrast, the small-world network reproduces the correct network oscillation temporal dynamics (fig.4.5c, fig.S4.6a, bottom, fig.S4.9a). Furthermore, the spatial arrangement of connections introduced by the small-world architecture adds a spatial dimension to the dynamics of network activity (see Supplementary Information 5, fig.S4.9a). Soon after stimulus onset, when synaptic connections are near their default strength, oscillatory spiking is largely coherent across the network of excitatory

neurons. However, because of synaptic depression and the distance-dependence of connections, the network dynamically subdivides, and coherent oscillations proceed among spatially separate groups of neurons in the steady-state. This spatiotemporal dynamic predicts a dependence of CC temporal dynamics on distance between neurons (fig.S4.9b, c).

Taken together, these results strengthen the hypothesis that the experimentally-observed dynamics of correlated variability are primarily driven by the dynamics of thalamocortical network oscillations. As such, synaptic time constants and synaptic depression are two intrinsic parameters relevant to correlated variability. Constraining the model to also produce a realistic network oscillation temporal dynamic reveals an additional role for synaptic clustering.

4.4 Discussion

To study how cortical coordination evolves during visual processing, we measured correlated variability between the membrane potentials of pyramidal neuron pairs in turtle visual cortex during ongoing and visually-evoked activity. This approach provides an exceedingly rare and much-needed view into the subthreshold events underlying coordinated spiking activity [84], and importantly, is uncorrupted by issues associated with spike-based investigations. For example, the process for targeting cells for recording is agnostic to the cells spike rates, and this study thus gives voice to the dark neurons that overwhelmingly populate the cortex [207], but are rarely represented in the vast literature on correlated variability. By supplementing our experimental approach with a model network investigation, we further addressed the relative contribution of the thalamocortical

network to the dynamics of correlated variability, and identified relevant network variables.

We found that both extended and brief visual stimulation evoked large, low-frequency membrane potential fluctuations (fig.4.1e), with nested gamma-band (20 – 100 Hz) oscillations (fig.4.2c and fig.4.3a), both of which varied significantly from trial to trial (fig.4.2a and b, fig.4.3a). This gamma-band variability was significantly correlated across the population of pairs in a given window of activity (fig.4.2b and c). It is reasonable to ask whether this is at all relevant to sensory processing, given that cortical neurons transmit spikes, and not subthreshold fluctuations. Previous work suggests it is. First, the fluctuations themselves are important for interpreting spiking activity in networks of sparse-spiking neurons; subthreshold gamma oscillations define narrow windows in which a given neuron is most likely to fire, and thus determine precise spike timing [204,208]. Second, the across-trial variability of these fluctuations constrains that of the spiking activity [209]; spiking responses can be no more reliable than the corresponding subthreshold activity. Finally, if and when neurons do spike in this visually-evoked high conductance state, the spike correlations will be shaped by state-induced changes in response gain, distance from threshold, and subthreshold correlations [84]. In fact, this last relationship may be supralinear [210], meaning that small changes in subthreshold correlated variability can have major repercussions for supra-threshold coordination.

What determines the strength of correlations in these single-trial deviations for a given pair of neurons? Anatomical connectivity is one obvious candidate, but what are the relative contributions from feedforward and recurrent connections (fig.4.1b)? Recent work has shown that the coupling of the spiking activity of a neuron with that of the population is stimulus-invariant [191, 192], suggesting a crucial role for intracortical connectivity. In

agreement with this, we found that gamma band correlated variability for ongoing and evoked activity was significantly related, for both the non-adapted (transient, fig.4.2e) and adapted (steady-state, fig.4.2f) conditions. In addition, although all pairs of neurons were separated by less than 300 microns, and therefore likely received similar sensory inputs [211], correlated variability was broadly-distributed across the population during a given window of activity (fig.4.3b and c). This variability suggests that the sparse connectivity of the cortex dramatically affects the distribution of pairwise correlations [190]. Indeed, alternate network models with higher connectivity were unable to reproduce this variability (data not shown).

Connectivity was not the only relevant parameter; for most pairs of neurons, and for the population as a whole, gamma band correlated variability increased with visual stimulation, but then relaxed to near ongoing values, despite persistent activity (fig.4.2). That is, for a given network (i.e., an anatomical arrangement of feedforward and recurrent connections), the level of coordination was not static. This was true for responses to both extended and brief stimulation (fig.4.3b and c) suggesting the dynamic did not reflect a change in the statistics of the sensory inputs. Previous experimental work implicates the cortical state: coordination in spiking activity [191, 192], synaptic inputs [121, 194], and membrane potentials [208] appear to be related to network synchrony. Accordingly, we found ample experimental and computational evidence implicating an evolving network state. Specifically, changes in correlated variability across epochs were related to changes in properties of the power spectra (fig.4.4b and c), and reflected a phase synchrony dynamic (fig.S4.4) consistent with a network adapting from a "disinhibited" to a "balanced" state [110]. In addition, the model revealed a strong relationship between network spike-rate oscillations and gamma-band correlated variability (Supplementary Information 5),

and also demonstrated the synaptic basis: synaptic current correlations and the lag between excitation and inhibition are larger for pairs of neurons in a synchronous network than for those in an asynchronous network (Supplementary Information 5, fig.S4.8). As such, our experimental results relating correlated variability to network state are in simultaneous agreement with multiple experimental studies of cortical activity across a variety of preparations and spatial scales, and importantly, demonstrate this principle in action at the level of the membrane potential during sensory processing. Moreover, our model results confirm computational predictions relating synaptic current dynamics to membrane potential correlations [84, 190], and extend previous work by demonstrating the effects of synaptic clustering and adaptation.

Gamma band correlated variability decreased from transient to steady-state, yet remained significantly nonzero (fig.4.2d and fig.4.3c). While vanishingly-small values would theoretically support greater response fidelity [195], this realized steady-state value may reflect the level of neuronal interaction necessary for cortical function (e.g., feature binding [212], effective signal propagation [85], and general cognitive function [129]). In other words, cortical coordination during sensory processing is maintained at an intermediate level (i.e., less than that during the initial response phase, but larger than zero) that represents the ideal balance between competing cortical needs (fig.4.1c). This balanced state can be maintained across stimulus conditions by intrinsic adaptation mechanisms.

Previous studies have described a stimulus-induced abolition of low-frequency correlated variability in membrane potential [208] and membrane potential–LFP [201] pairs in visual cortex. We observed no such decrease (fig.S4.3a, b). This discrepancy may be partially explained by the nature of ongoing activity. In these previous studies, visual stimulation interrupted large-amplitude, low-frequency events that were coherent across

electrodes and had random phase relative to stimulus onset. These fluctuations largely remained in residual traces, likely influencing pre-stimulus correlated variability. In contrast, these spontaneous bursts of activity occurred relatively infrequently in our experiments (fig.4.1e, fig.4.2a and b). To reproduce this quiescent –to– active sensory-evoked dynamic, we limited the inputs to our model neurons to those from external stimulation, and stimulus-triggered, yet internally-generated events. Our model could likely be modified to reproduce the results of these other works by adding a shared background fluctuation [84]. This brute-force implementation would not be very illuminating, however; spontaneous events can be strikingly similar to evoked [205, 206, 213], and may therefore represent activity in the same microcircuits, triggered by events usually hidden from the experimenter. Reproducing spontaneous events in a manner that is consistent with their possible sources is beyond the scope of this study.

Here, we have focused on fundamental properties of the cortex (anatomical and emergent) that are likely to strongly influence correlated variability. Future work can more definitively assess the relative contributions to cortical coordination from various intracortical and extracortical sources not addressed here, such as strong inhibitory feedback [214, 215], thalamic adaptation [216, 217], unequal adaptation of excitatory and inhibitory cortical synapses [218], and the (time-varying) statistics of neuronal activity in the early visual pathway (e.g., correlations across thalamic inputs [219, 220]), to name a few. Of particular interest are top-down influences (e.g., attention), which have been shown to impact spike-count correlations in awake, behaving preparations [221,222]. Our results predict that such higher-order inputs may impact correlated variability by influencing the network state. It will be interesting to test this hypothesis, and to determine the synaptic basis of the interaction if confirmed. Further, it is crucial to test for a relationship between subthreshold correlated variability and psychophysical performance,

which will require a behavioral assay. As dual whole-cell recordings in awake, behaving preparations (possibly combined with other recording modalities in multiple areas) become increasingly common, future experiments can be designed to address these exciting questions.

4.5 Methods

4.5.1 Surgery

All procedures were approved by Washington Universitys Institutional Animal Care and Use Committees and conform to the guidelines of the National Institutes of Health on the Care and Use of Laboratory Animals. Seventeen adult red-eared sliders (Trachemys scripta elegans, 150 – 1000 gr) were used for this study. Turtles were anesthetized with Propofol (2 mg Propofol/kg), then decapitated. Dissection proceeded as described before [223, 224]. In brief, immediately after decapitation, the brain was excised from the skull, with right eye intact, and bathed in cold extracellular saline (in mM, 85 NaCl, 2 KCl, 2 $MgCl_2$ *$6H_2O$, 20 Dextrose, 3 $CaCl_2 - 2H_2O$, 45 $NaHCO_3$). The dura was removed from the left cortex and right optic nerve, and the right eye hemisected to expose the retina. The rostral tip of the olfactory bulb was removed, exposing the ventricle that spans the olfactory bulb and cortex. A cut was made along the midline from the rostral end of the remaining olfactory bulb to the caudal end of the cortex. The preparation was then transferred to a perfusing chamber (Warner RC-27LD recording chamber mounted to PM-7D platform), and placed directly on a glass coverslip surrounded by Sylgard. A final cut was made to the cortex (orthogonal to the previous and stopping short of the border

between medial and lateral cortex) allowing the cortex to be pinned flat, with ventricular surface exposed. Multiple perfusion lines delivered extracellular saline, adjusted to pH 7.4 at room temperature, to the brain and retina in the recording chamber.

4.5.2 Intracellular Recordings

For whole-cell current clamp recordings, patch pipettes (4 – 8 MΩ) were pulled from borosilicate glass and filled with a standard electrode solution (in mM; 124 $KMeSO_4$, 2.3 $CaCl_2 - 2H_2o$, 1.2 $MgCl_2$, 10 HEPES, 5 EGTA) adjusted to pH 7.4 at room temperature. Cells were targeted for patching using a dual interference contrast microscope (Olympus). Simultaneously recorded cells were located less than 300 microns apart, and all cells were located within 300 microns of an extracellular recording electrode. Intracellular activity was collected using an Axoclamp 900 A amplifier, digitized by a data acquisition panel (National Instruments PCIe-6321), and recorded using a custom Labview program (National Instruments), sampling at 10 kHz. We excluded cells that did not display stable resting membrane potentials. The visual cortex was targeted as described below.

4.5.3 Extracellular Recordings

Extracellular recordings were achieved with tungsten microelectrodes (MicroProbes heat treated tapered tip), with approximately 0.5 MΩ impedance. Electrodes were slowly advanced through tissue under visual guidance using a manipulator (Narishige), while monitoring for activity using custom acquisition software (National Instruments). Extracellular activity was collected using an A-M Systems Model 1800 amplifier, band-pass

filtered between 1 and 20,000 Hz, digitized (NI PCIe-6231), and recorded using custom software (National Instruments), sampling at 10 kHz.

4.5.4 Identification of Visual Cortex

We used a phenomenological approach to identify the visual cortex, described previously [225]. In general, this region was centered on the anterior lateral cortex, in agreement with voltage-sensitive dye studies [226, 227]. Anatomical studies identify this as a region of cortex receiving LGN projections [211].

4.5.5 Visual Stimulation

Whole-field flashes were presented using either a red LED (Kingbright, 640 nm), mounted to a manipulator and positioned 1 – 5 cm above the retina, or a projector-lens system (described below). The mean LED light intensity (irradiance) at the retina was 60 W/m^2. For one turtle, we used these same LEDs in conjunction with 200 micron optical fibers (Edmund Optics) to project sub-field flashes (1 – 200 ms) onto the visual streak. Other stimuli were presented using using a projector (Aaxa Technologies, P4X Pico Projector), combined with a system of lenses (Edmund Optics) to project images generated by a custom software package directly onto the retina. The mean irradiance at the retina was 1 W/m^2 . This system was used to present brief (100 – 250 ms) whole-field and sub-field flashes (red or white), sustained (10 s) gray screen, a naturalistic movie (*Catcam*) a motion-enhanced movie (courtesy Jack Gallant), and a phase-shuffled version of the same movie (courtesy Jack Gallant and Woodrow Shew). In all cases, the stimulus was triggered using a custom Labview program (National Instruments).

The preparation was in complete darkness before and after each stimulus presentation. Flashes lasted between 1 ms and 150 ms, with at least 20 s between flashes. Movies lasted either 10 s or 20 s, and were shown at least 12 times, with at least 30 s between the end of one presentation and the beginning of the next. We presented extended visual stimuli (movies) while recording from 19 pairs, and brief stimuli (diffuse flashes) while recording from 16 pairs.

4.5.6 Signal Processing

In all analyses, only cells with 12 or more visual stimulation trials were included. Raw data traces were down-sampled to 1000 Hz. Because action potentials in turtle cortical pyramidal neurons are relatively wide, spike waveforms still contributed to the band-pass filtered intracellular recordings. To remove these, an algorithm was used to detect spikes, and the membrane potential values in a 20 ms window centered on the maximum of each spike were replaced via interpolation. Finally, the traces were filtered (20 Hz lowpass or 20 – 100 Hz bandpass Butterworth filter).

4.5.7 Cross-correlation Analysis

For each single-trial voltage trace, the residual (V r or deviation from the average activity) was found by subtracting the across-trial average time series from the single-trial time series:

$$V_r = V - < V >_{trials} \tag{4.1}$$

Residuals were then separated into three epochs: the ongoing epoch (defined to be the two seconds prior to the onset of visual stimulation), the transient epoch (200 to 600 ms after stimulus onset), and the steady-state epoch (800 to 2800 ms after stimulus onset; fig.4.2a). For each pair of simultaneously-recorded cells, the Pearson correlation between residual pairs was then calculated for each epoch and trial. The results were averaged across all trials, resulting in the trial-averaged correlated variability (CC) for each pair and epoch:

$$CC^{epoch} =< \frac{cov(V_{r,1}^{epoch}.V_{r,2}^{epoch})}{\sqrt{var(V_{r,1}^{epoch}).var(V_{r,2}^{epoch})}} >_{trials} \tag{4.2}$$

Because the correlated variability of spike counts been shown to depend on the size of the window used for calculations [203], we repeated the above process for three other sets of choices for epoch window sizes and gaps between epochs (see Supplementary Information 1).

The significance of CC for a given pair and epoch was determined by bootstrapping; CC was considered to be significantly nonzero if the average value $\pm$ the 95% confidence level from bootstrapping did not include zero. Similarly, CC for two epochs were considered to be significantly different from one another if the bootstrapping intervals did not overlap.

For the population of pairs, we determined the significance of the population-average CC for a given epoch using the one-sample t-test (that is, by comparing to a zero-mean normal distribution with the same standard deviation). We tested for a significant change in population CC values across two epochs by applying the Wilcoxon signed-rank test to the two sets of CC values.

We also compared CC for responses to brief and extended visual stimulation. First, pairs were segregated according to the stimulus presented, resulting in 17 flash and 22

extended-stimulus pairs. The two resulting sets of trial-averaged CC values were then compared using the Wilcoxon rank-sum test.

4.5.8 Power Analysis

For each trial and cell, we extracted a 5.8 s window of activity (with epoch windows and gaps between epochs as described above, plus 500 ms windows on eac end to avoid filtering artifacts in the ongoing and steady-state epochs), and calculated the residual time series as described above. For each residual trace, we performed wavelet analysis in Matlab using software provided by C. Torrence and G. Compo (available at URL: http://paos.colorado.edu/research/wavelets/, [107]). This resulted in a power time series for each cell, for multiple frequencies. For each frequency below 100 Hz, we averaged the time series across each epoch to obtain the average power at each frequency for each epoch. We then averaged across trials. For each pair, we also averaged across all frequencies in the gamma range (20 - 100 Hz), and plotted the resulting trial-averaged gamma power (P) in each epoch to inspect for trends across the population (fig.4.2e). We tested for significant changes in a given pair and across the population using the same methods as those described for CC values.

We next inspected for a relationship between changes in CC and changes in gamma power for a given pair. For the ongoing–to–transient and transient–to–steady-state transitions, we calculated the change in trial-averaged gamma power for each neuron

$$\Delta P_{neuron}^{epoch1 \rightarrow epoch2} = P_{neuron}^{epoch2} - P_{neuron}^{epoch1} \tag{4.3}$$

and took the geometric mean of the absolute values:

$$\sqrt{|\Delta P_1.\Delta P_2|}^{epoch1 \rightarrow epoch2} = \sqrt{|\Delta P_1^{epoch1 \rightarrow epoch2}.\Delta P_2^{epoch1 \rightarrow epoch2}|} \tag{4.4}$$

For each pair, we plotted the absolute value of the average change in CC vs. the result, and performed linear regression analysis (fig.4.4a).

For each cell, we also obtained the relative power spectrum (rP) for the transient and steady-state epochs, defined to be the trial-averaged evoked spectrum divided by the trial-averaged ongoing spectrum (fig.4.2d, fig.S4.6a, c): $rP_{neuron}^{epoch} = P_{neuron}^{epoch} / P_{neuron}^{ongoing}$. Second, to obtain the peakiness of the relative power spectrum within the gamma range for each cell, we divided the maximum value of rP in the gamma range by the average value in the gamma range to obtain the peak ratio (M_{neuron}^{epoch}) (fig.4.4b, similar to [208]):

$$M_{neuron}^{epoch} = \frac{[max(rP_{neuron}^{epoch})]_{gamma}}{[avg(rP_{neuron}^{epoch})]_{gamma}} \tag{4.5}$$

(where $M_{neuron}^{ongoing} = 1$). We then calculated the change in peak ratios across epochs:

$$\Delta M_{neuron}^{epoch1 \rightarrow epoch2} = M_{neuron}^{epoch2} - M_{neuron}^{epoch1} \tag{4.6}$$

and then the geometric mean of the absolute values for each simultaneously-recorded pair ($\sqrt{|\Delta M_1.\Delta M_2|}$). Finally, we inspected for a relationship between $\sqrt{|\Delta M_1.\Delta M_2|}$ and changes in CC for a given pair (fig.4.4c) as described above for changes in power.

4.5.9 Phase Concentration Analysis

For each residual trace in a given trial, we used wavelet analysis (described above) to calculate the phase of each signal as a function of time and frequency. We then averaged over all frequencies in the gamma range (20 - 100 Hz) to obtain the gamma phase time series for each trace ($\phi_i(t)$). For each pair of residuals, we calculated the cosine of the phase difference, and averaged over each epoch to obtain the phase concentration (R) for each epoch and trial:

$$R_{epoch}^{trial} =< cos[\phi_1(t) - \phi_2(t)] >_{epoch}^{trial} \tag{4.7}$$

We then averaged over all trials and analyzed the results for pairwise and population trends using the same methods as those described for CC values (fig.S4.4b). We also inspected for a relationship between changes in CC and changes in R for a given pair (fig.S4c) as described above for changes in power.

4.5.10 Network Models

To investigate the roles of network properties in our experimental results, we implemented a model network of 800 excitatory and 200 inhibitory leaky-integrate- and- fire neurons. Excitatory-excitatory connections had small-world connectivity [219,228] (with 5% connection probability), and all other connections were random (with 5% excitatory-inhibitory, and 10% inhibitory-excitatory and inhibitory-inhibitory connection probability). Each nonzero entry in the connection weight matrix was drawn from a Gaussian distribution with mean value 1.

The dynamics of the membrane potential (V) of each neuron evolved according to

$$\tau_m \frac{dV(t)}{dt} = -g_L[V(t) - E_L] + I_{syn}(t) \tag{4.8}$$

where the membrane time constant $\tau_m = 50$ ms (excitatory neurons), 25 ms (inhibitory), and the leak conductance $g_L = 10$ nS (excitatory), 5 (inhibitory). The leak reversal potential E_L for each neuron was a random value between -70 and -60 mV, drawn from a Gaussian distribution. The reversal potentials for the synaptic current $I_{syn}(t)$ were $E_{GABA} = -68$ mV, and $E_{AMPA} = 50$ mV.

The synaptic current for each synapse type (between presynaptic neurons of type X and postsynaptic neurons of type Y) had three relevant time course parameters: delay (τ_{LX} , that is, the lag between presynaptic spike time and beginning of conductance waveform), rise time (τ_R^{YX}), and decay time (τ_D^{YX}). Synaptic conductances were modeled as products of time-varying gating variables (S_{YX}) and maximum conductances (g_{YX}). Following a presynaptic spike at time 0, the gating variable dynamics were described by

$$S_{YX}(t) = \frac{\tau_m}{(\tau_D^{YX} - \tau_R^{YX})}[exp^{(-(t-\tau_{LX})/\tau_D^{YX})} - exp^{(-(t-\tau_{LX})/\tau_R^{YX})}] \tag{4.9}$$

with time constants (in ms) $\tau_{LE} = 1.5$, $\tau_R^{EE} = 0.2$, $\tau_D^{EE} = 1.0$, $\tau_R^{IE} = 0.2$, $\tau_D^{IE} = 1.0$, $\tau_{LI} = 1.5$, $\tau_R^{II} = 1.5$, $\tau_D^{II} = 6.0$, $\tau_R^{EI} = 1.5$, $\tau_D^{EI} = 6.0$. Maximum conductance values (in nS) were $g_{EE} = 1.0$, $g_{IE} = 6.0$, $g_{EI} = 30$, $g_{II} = 30$. In response to a presynaptic spike, the weight (W) of a synapse depressed and recovered according to

$$\frac{dW_{ij}(t)}{dt} = -\frac{W_{ij}(t)}{\tau_{depress}}.\delta(t - t_j^{sp}) + \frac{W_{ij}^0 - W_{ij}(t)}{\tau_{recover}} \tag{4.10}$$

with depression time constant $\tau_{depress} = 30$ ms, recovery time constant $\tau_{recover} = 1500$ ms and t_j^{sp} is the spiking time in presynaptic neuron j^{th}. Depression and recovery time constants were chosen to give reasonable activity time courses for low-frequency (0 – 20 Hz) membrane potentials. The spike threshold for each neuron was -40 mV. A neuron reset to -59 mV after spiking, and was refractory for 2 ms (excitatory) and 1 ms (inhibitory).

All excitatory neurons received Poisson external inputs. During ongoing activity, the external input rate to each neuron was 25 Hz. The stimulus was modeled as a gradual increase to 500 Hz; the input rate was increased by 95 Hz at stimulus onset, and by an additional 95 Hz every 50 ms for 200 ms. This gradual increase provided more realistic low-frequency membrane potentials than did a single step function stimulus, but did not qualitatively impact the results. The gating variables for external inputs had the same parameters as for excitatory-excitatory connections, and maximum conductances were $g_E = 4$ nS.

Each trial was 5.8 s in duration, with stimulus onset at 2.7 s, and the time step was 0.05 ms. The ongoing epoch was defined to be 2200 ms to 200 ms before stimulus onset, the transient epoch 0 ms to 400 ms after stimulus onset, and the steady-state epoch 600 ms to 2600 ms after stimulus onset. The additional 500 ms at the beginning and end of each trial ensured there were no wavelet filtering artifacts in the ongoing and steady-state epochs.

We then randomly selected 20 excitatory neurons, and generated 40 V-V pairs from these twenty. Because action potential rates were higher in this model network than in experiment, and because action potentials can affect V-V noise correlations, we substituted test neurons for these network neurons before doing the calculation (see Supplementary Information 6). Test neurons were identical to network neurons, but all synaptic conductances were multiplied by a factor of 0.5, and spike threshold was raised to -30 mV, which

was sufficient to eliminate all action potentials. Thus, a test neuron membrane potential acted as a network sub-sampler, representing the response to re-scaled versions of inputs to the corresponding network neuron. For each pair of test neurons, we then calculated the same parameters as for experimental neuron pair (CC, R, etc.). We also calculated cross correlations as a function of lag for residual synaptic conductance traces (fig.S4.8). This process was identical to that described for the (zero lag) Pearson correlation coefficient described above, but was performed for all lags in ± 50 ms.

For each trial, we calculated the instantaneous spike rate of all excitatory neurons in the network. We then calculated the power spectra of the transient and steady state spike rates using wavelet filtering, and averaged over all trials (fig.S4.6), as described above.

To investigate the dependence on distance between neurons, we repeated the above analysis for this model using two alternate sets of randomly-selected neurons. First, we randomly selected 20 neurons from a group of 100 neighboring neurons. Second, we used a smaller group of 20 neighboring neurons (see Supplementary Information 5, and fig.S4.9).

In addition, we implemented two alternate model versions (see Supplementary Information 5, and fig.S4.6, S4.7, S4.8). In one, we eliminated synaptic adaptation. In the other, we maintained synaptic adaptation, but tuned synaptic time courses to give an asynchronous transient epoch ($\tau_{LX} = 1.5$ ms, $\tau_R^{YX} = 0.2$ ms, $\tau_D^{YX} = 1.0$ ms for all X and Y). (In the absence of adaptation, this version was also asynchronous in the steady-state.)

Acknowledgments

We thank Woodrow Shew for assistance with the design of the visual stimulus. We thank Thomas Crockett for contributing data. This research was supported by a Whitehall Foundation grant #20121221 (R.W.) and a NSF CRCNS grant #1308159 (R.W.).

Author Contributions

N.W., M.H., and R.W. conceived the study and designed the experiments. N.W. performed the experiments. M.H. performed the model simulations. N.W. analyzed the data. N.W., M.H., and R.W. wrote the paper.

Competing Financial Interests

The authors declare no competing financial interests.

4.6 Supplementary Materials

4.6.1 Supplementary Information 1: windows of activity chosen for analysis

When relating two measures of cortical coordination (e.g., correlated variability and network state), the ideal approach would be to determine both measures for the same dataset. Unfortunately, some experimental methods for recording large-scale population activity (e.g., microelectrode array, or MEA, recordings) and those for recording pairs of membrane potentials (pairwise whole-cell recordings) are not easily implemented in the same region of cortex simultaneously. Furthermore, determining the network state requires a large number of neuronal avalanches, and therefore recording times that often surpass the amount of time a typical whole-cell patch remains stable. As such, we motivated our choice of windows for this study based on the results of a previous study of population activity in the same preparation [225].

In this previous work, the "transient" epoch for a given preparation was defined by the total network activity over all trials. Briefly, the activity at each electrode was band-pass filtered to give the local field potential (LFP), the absolute value of the resulting trace was divided by its standard deviation, and all such traces from responsive electrodes were summed to give the network activity for a single trial. All trials were overlaid, the 90th percentile envelope was calculated, and the transient epoch was defined to be the full-width at half-max of this envelope. The "v"isually-driven steady-state" began at the end of the transient epoch, and ended with the stimulus. The transient epoch was calculated on a prep-by-prep basis, and across all preparations, lasted 423 ± 202 ms

($mean \pm SD$). For nine preparations and four different stimuli, the transient epoch was shown to be supercritical, and the visually-driven steady-state critical. There were not enough ongoing avalanches to determine the pre-stimulus state.

Translating this result into window choices for this study involved two additional considerations. First, the resting membrane potential of a neuron affects the amplitude of depolarization for a given level of synaptic input. As such, taking the absolute value and overlaying trials to calculate the 90th percentile envelope, as above, for a pair of neurons may not be a viable approach. Second, noise correlation distributions (for spike data) depend on window size, and so the three epochs should be of comparable duration. That is, a transient epoch of around 400 ms, and a steady-state epoch of nearly 10 s would not be appropriate. With this in mind, we chose the same epochs for all recorded pairs: the ongoing and steady-state epochs were chosen to be 2 s in duration, and the transient epoch 400 ms. Due to the observed variability in the previous study, epochs were separated by 200 ms (with the end of the ongoing epoch coinciding with stimulus onset, 4.2a).

These choices have implications for our assumptions about the network state during each epoch. Specifically, the transient epoch as defined in this study is presumed to be in general supercritical, but this has not been shown explicitly for this window choice. Furthermore, the label of "critical" is only valid for the full visually-driven steady-state from the previous study (see above), and the steady-state epoch as defined in this study is a subset of that activity. As such, we work under the somewhat weaker assumption that the cortex is supercritical during the transient epoch, and is adapting toward criticality during the steady-state (although it may not yet be critical).

To test the robustness of our results, we repeated the analysis for three other sets of epoch windows and gaps: the windows described above, but with a 300 ms gap between stimulus onset and beginning of transient epoch (fig.S4.1a, b), 1 s windows for all epochs with no gaps (fig.S4.1c, d), and 400 ms windows for all epochs, with 1 s gaps (fig.S4.1e, f). For all choices, the population trends were approximately the same, suggesting that the observed noise correlations generally reflect those of "pre-stimulus" activity, "early" response, and "late" response. For a given epoch, however, across-population variability did decrease somewhat with increasing window size (e.g., compare fig.S4.1d and f), and so the increase in variability from ongoing to transient epochs in the original set of choices may be partially due to this effect.

4.6.2 Supplementary Information 2: spectral content of residual traces, frequency bands chosen for analysis, and low-frequency results

For each cell, we calculated the across-trial average power for the ongoing, transient, and steady-state epochs using the wavelet transform (see Methods). Across cells, visual stimulation (either brief or extended) evoked a broad-band increase in residual power in the transient epoch (fig.S4.2a). Residual power generally decreased in the steady-state, but was still elevated above ongoing levels (fig.S4.2b). The height and location of peaks in residual relative power (rP) spectra varied across cells; for most cells (and for both response epochs), the peak frequency was in the 0.1 – 20 Hz range (fig.S4.2c). The size of the peaks (quantified by $M_{100} = rP_{max}/rP_{avg}$, calculated by considering all frequencies below 100 Hz) were generally large in the transient epoch, and varied continuously across cells (fig.S4.2d). Note that this definition for M_{100} is slightly different from that for M

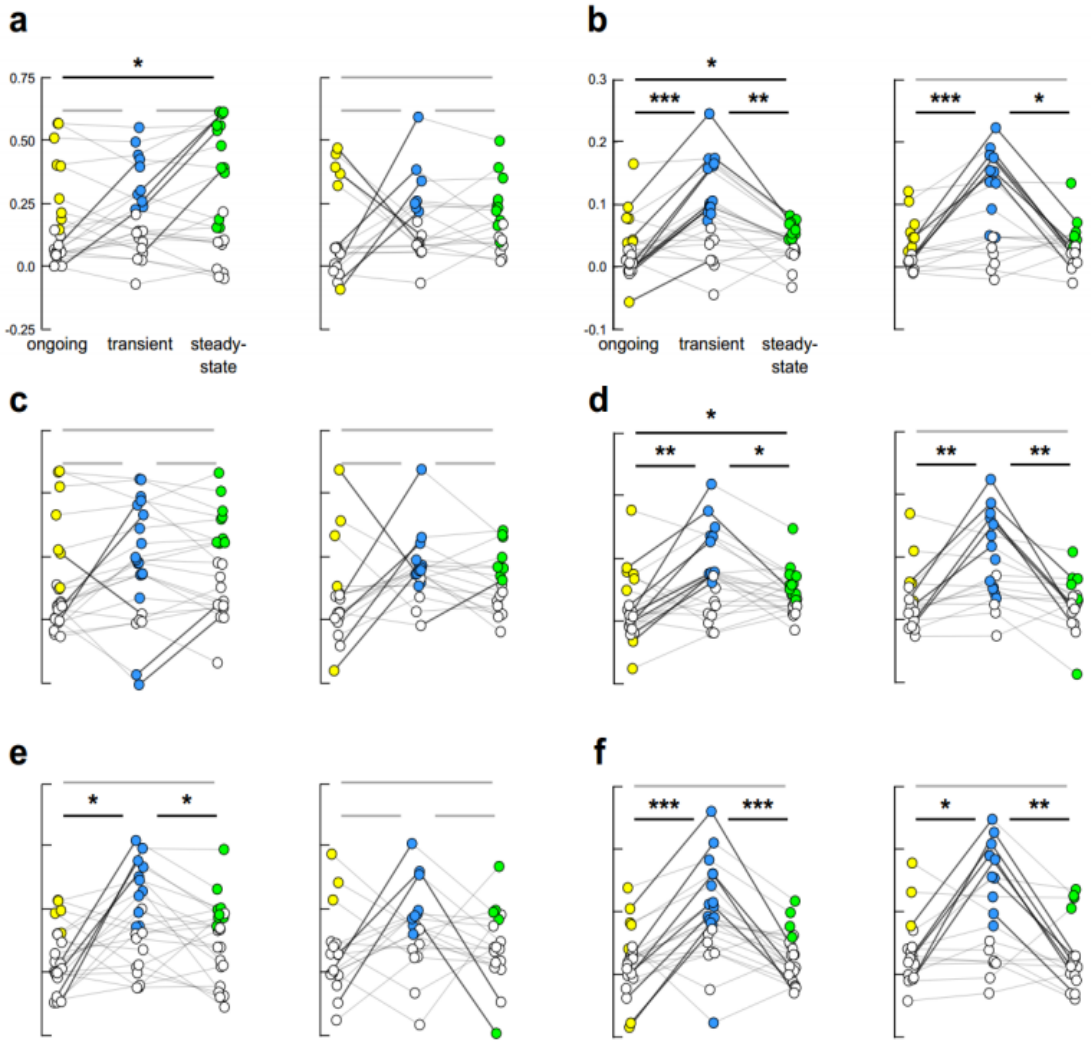

Figure S4.1: **Results for various choices of epoch windows and gaps between epochs.** Vertical scales are the same for a, c, e, and for b, d, f. Bars and asterisks linking epochs indicate results of tests for significance of changes in values across epochs (Wilcoxon signed-rank test): light bars correspond to insignificant changes ($P > 0.05$), * to $0.01 < P < 0.05$, ** to $0.001 < P < 0.01$, *** to $P < 0.001$. (a) Correlated variability (as in 4.2d) for epoch windows (in ms) ongoing = 2000, transient = 400, steady-state = 2000, with 0 ms between then end of the ongoing epoch and stimulus onset, 300 ms between stimulus onset and the start of the transient epoch, and 200 ms between the end of the transient epoch and the start of the steady-state epoch, for extended (left) and brief (right) stimuli, 0.1 – 20 Hz. Hereafter, these choices are indicated by, e.g. epochs = (2000, 400, 2000), gaps = (0, 300, 200). (b) Same as in (a), but for 20 – 100 Hz. (c, d) Same as in (a, b), but for epochs = (1000, 1000, 1000), gaps = (0, 0, 0). (e, f) Same as in (a, b), but for epochs = (400, 400, 400), gaps = (800, 200, 1000).

(used in Results and 4.4b, c), which is calculated using only frequencies in the 20 – 100 Hz range.

For the remainder of our analysis, we treated high- and low-frequency activity separately. There were three primary motivations for doing so. First, a recent study of V-LFP correlated variability (CC) in primate V1 found that low-frequency CC was stimulus-modulated, and high-frequency CC was not [201]. Second, it is a long-standing hypothesis that different frequency bands in cortical activity represent distinct functionalities [11, 229, 230], suggesting it is more reasonable to separate low and high frequencies than to analyze broad-band activity. Finally, after separately calculating CC for low (0.1 – 20 Hz) and high (20 – 100 Hz) frequencies, we observed that the two sets of CC values were not significantly correlated (fig.S4.3c), suggesting correlated variability of the two bands was independently modulated by visual stimulation. We refer to the high-frequency component as "gamma activity", although the bounds of gamma activity vary across studies.

Population-averaged correlated variability ($\langle CC \rangle$) for low frequencies gradually increased from ongoing to transient to steady-state for extended ($\langle CC \rangle = 0.175$ ongoing, 0.203 transient, 0.275 steady-state, $P = 0.758$ for ongoing–to–transient, $P = 0.046$ for transient–to–steady-state, $P = 0.016$ for ongoing–to–steady-state transition, Wilcoxon signed-rank test, fig.S4.3a) and brief ($\langle CC \rangle = 0.125$ ongoing, 0.175 transient, 0.181 steady-state, $P > 0.05$ for all across-epoch comparisons, Wilcoxon signed-rank test, fig.S4.3b) stimulation, although the modulation was stronger for extended.

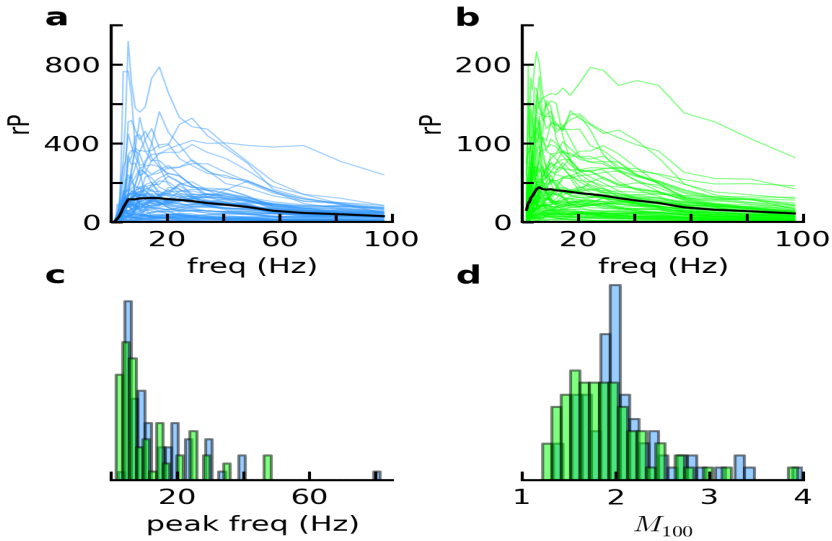

Figure S4.2: **Spectral properties of residual evoked activity vary across cells.** (a) Across-trial average relative power (rP, evoked divided by ongoing) for individual cells (blue lines), and across-cell average (black) for the transient epoch. (b) Same as in (a), but for steady-state epoch. (c) Distribution of peak frequencies in the 0.1 – 100 Hz range for all cells for the transient (blue) and steady-state (green) epochs. (d) Same as in (c), but for M_{100}, the ratio of of rP_{max} to rP_{avg} for each cell.

4.6.3 Supplementary Information 3: Modulation of phase relationship by visual stimulation

In this study, we use the correlated variability of gamma band residual traces as a measure of coordination between neurons. For pairs of analog signals, another popular measure is the phase difference6. This alternative measure is (non-trivially) related to correlation, and indeed, we did observe that some residual pairs tended to be more phase-locked during the transient than during the steady-state epoch (fig.S4.4a). To relate the results of our study to previous work, then, we also calculated the phase concentration of residual gamma band pairs (R), defined to be the cosine of the difference in phase angles for two residual traces, averaged over a window of interest, and then averaged over all trials (see

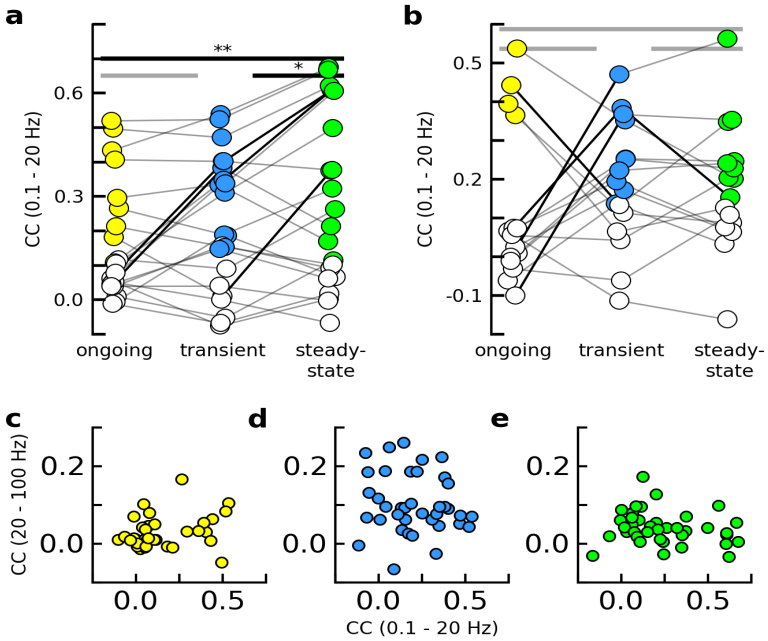

Figure S4.3: **Low– (0.1 – 20 Hz) and high– (20 – 100 Hz) frequency correlated variability were independent, and were modulated differently by visual stimulation.** (a) Correlated variability (CC) trajectories for 0.1 – 20 Hz bandpass-filtered data, for extended visual stimuli (compare with 4.3b). (b) Same as in (a), but for brief flashes (compare with 4.3c). (c - e) Across-trial average gamma band (20 – 100 Hz) CC vs. low-frequency (0.1 – 20 Hz) CC for each recorded pair (for both brief and extended stimuli), for the ongoing (c), transient (d), and steady-state (e) epochs. All linear regression fits insignificant ($P > 0.05$).

Methods). The phase concentration takes a value of +1 for a pair of perfectly in-phase signals, -1 for perfectly out-of-phase signals, and 0 for two signals with random phase.

We found that across the population of all pairs (including both brief and extended stimuli), the average phase concentration ($\langle R \rangle$) followed the same dynamics as $\langle CC \rangle$ ($\langle R \rangle = 0.030$ ongoing, 0.056 transient, 0.029 steady-state; $P = 3.70E^{-4}$ for ongoing–transient comparison, $P = 6.50E^{-5}$ for transient–steady-state comparison, $P = 0.97$ for ongoing–transient comparison, Wilcoxon signed-rank test, fig.S4.4b). Moreover, changes in CC were significantly related to changes in R ($r = 0.733$, $P = 1.70E^{-7}$ for ongoing–to–transient transition, $r = 0.712$, $P = 5.48E^{-7}$ for transient–to–steady-state transition, Pearson correlation, fig.S4.4c).

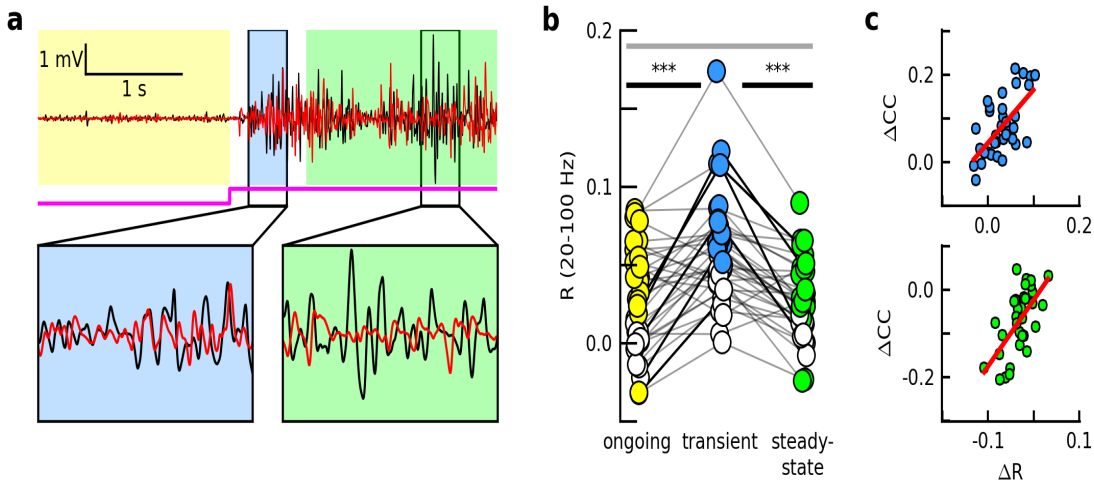

Figure S4.4: **Changes in correlated variability reflect changes in phase relationship between residual traces.** (a) Top: single-trial residual trace pair (same cell pair as in 4.2b, c). Bottom: close-up of transient and steady-state activity. (b) Same as in 4.2d, but for phase concentration (R) of gamma band residual pairs, for all recorded pairs. (c) Change in CC vs. change in R across epochs for gamma band residual pairs for ongoing–to–transient transition (top) and transient–to–steady-state transition (bottom). Red lines indicate significant linear regression fit ($r^2 = 0.537$, $P = 1.70E^{-7}$ for ongoing–to–transient transition, $r^2 = 0.507$, $P = 5.48E^{-7}$ for transient–to–steady-state transition).

4.6.4 Supplementary Information 4: comparison of responses to brief and extended visual stimulation

To investigate the dependence of correlated variability on the nature of the stimulus, we utilized both brief and extended visual stimulation (see Methods and Results). Briefly, we recorded from 19 pairs while presenting extended stimuli (lasting 10 s or longer), and 16 pairs while presenting brief (lasting 10 – 150 ms) subfield or whole-field flashes.

We compared the results in two ways. First, for each response epoch, we compared the sets of CC values for the extended and brief stimuli using the Wilcoxon rank-sum test (the distributions are visualized using histograms in fig.S4.5). For both epochs and frequency

bands, the two sets of values were not significantly different ($P > 0.05$, Wilcoxon rank-sum test), suggesting feedforward sensory input plays at best a small role in determining noise correlation strength across the population. Low-frequency values were larger for extended stimuli (see Supplementary Information 2), but not significantly so. Second, we qualitatively compared the across-epoch CC dynamics for the two stimulus types (see Results). In general, stimulus modulation of low-frequency CCs was weaker for brief stimuli (see Supplementary Information 2; fig.S4.3a, b), but for gamma band CCs, the dynamics were essentially the same (fig.4.3b, c).

It is important to note that in response to brief flashes, input to the cortex from the lateral geniculate nucleus (LGN) can continue beyond the duration of the stimulus. Specifically, previous work in turtle retina indicates that brief (220 ms) sub-field flashes of 646 nm light can evoked depolarization and spiking in retinal ganglion cells up to 200 ms after stimulus offset [231]. Thus, for a typical brief flash used in this study (e.g., 150 ms) it is possible that some sensory inputs to cortex persist during the steady-state epoch. There is no evidence, however, that persistent retinal responses to brief flashes last on the order of seconds. Furthermore, previous work has concluded that the AMPA- and NMDA-mediated EPSPs and GABA-mediated IPSPs that dominate persistent responses (to electrical stimulation of either cortex or LGN fibers) in turtle cortex are intracortical in origin, and distinct from excitatory LGN inputs [232]. As such, we assume that the vast majority of steady-state activity in response to brief visual stimulation can be attributed to intracortical feedback.

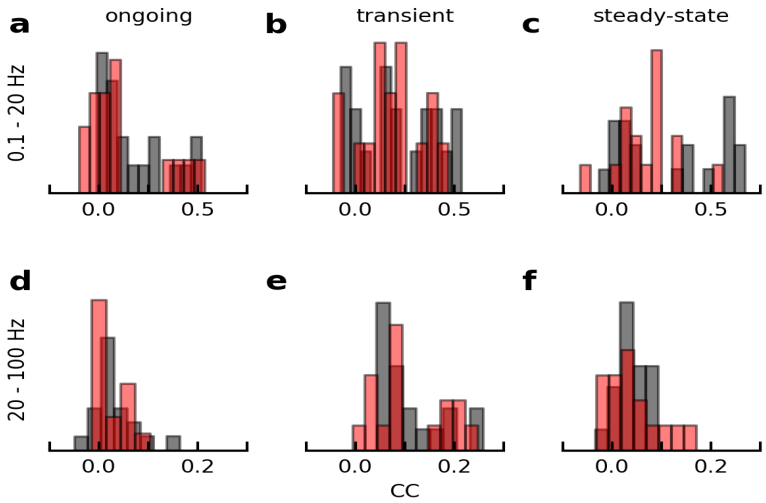

Figure S4.5: **Correlated variability is similar for responses to brief flashes and extended visual stimuli.** (a-f) Distributions of CC values for extended stimuli (black) and brief flashes (red), for the ongoing (a, d), transient (b, e), and steady-state (c, f) epochs, for 0.1 – 20 Hz (top row) and 20 – 100 Hz (bottom row) activity. $P > 0.05$ for all pairs of distributions (Wilcoxon rank-sum test).

4.6.5 Supplementary Information 5: additional model results

In order to better understand our model results, we implemented three versions of the small-world network: the model described in Results, in which adaptation was tuned to closely reproduce the experimental results (hereafter referred to as the "synchronous" model, fig.S4.6); a model identical to the synchronous model, but with synaptic adaptation removed ("synchronous, no adaptation"); and a model that was identical to the synchronous model, but with excitatory and inhibitory time constants tuned to result in an asynchronous post-stimulus state ("asynchronous" model, see Methods).

Residual membrane potential relative power spectrum peaks reflect network spike rate oscillations. In the experimental data, the relative power spectra of many cells had clear peaks in the gamma (20 – 100 Hz) spectrum (fig.4.2d, fig.S4.2a, b). This was also true of cells in the synchronous model (fig.S4.6a, top). Moreover, the location of the peak in the simulated

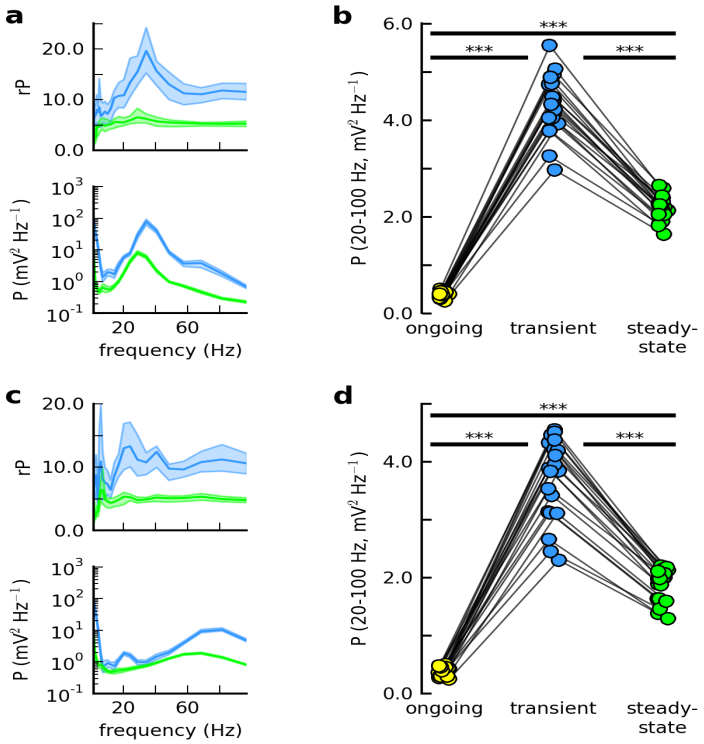

Figure S4.6: **Residual membrane potential relative power spectrum peaks reflect network spike rate oscillations.** (a b) Synchronous model. (c-d) Asynchronous model. (a) Top: relative power (evoked divided by ongoing) in residual membrane potential traces for one randomly-selected model neuron for the transient (blue) and steady-state (green) epochs. Bottom: power in network spike rate for the transient (blue) and steady-state (green) epochs. Dark lines indicate across-trial averages, bands indicate 95% confidence intervals (via bootstrapping, see Methods). (b) Same as in fig.4.5a, but for 20 randomly-selected pairs from SWA model. (c - d) Same as (a b), but for AWA model.

data coincided with the frequency of the network spike-rate oscillation (fig.S4.6a, bottom). In the asynchronous network, the network spike rate power spectrum did not contain prominent peaks (fig.S4.6c, bottom), and peaks in the membrane potential spectra were smaller than those in the synchronous network (fig.S4.6c, top). In both networks, total gamma power in residual membrane potential traces followed trajectories similar to that observed in experiment (fig.S4.6b, d, compare to 4.2e), and generally reflected the average network spike rate in the two evoked epochs (fig.S4.9a).

Together, these results suggest the across-epoch changes in gamma power observed in experimental membrane potential residuals reflect changes in the level of network spiking activity, and that peaks in the gamma spectrum reflected oscillations in the network spike rate.

Network spike rate oscillations increase correlated variability, and synaptic adaptation reduces correlated variability by abolishing these oscillations. We used the synchronous, no adaptation and asynchronous models to further test the relationship between network oscillations and membrane potential correlated variability. In the synchronous, no adaptation model, the population-averaged correlated variability ($\langle CC \rangle$) increased from ongoing to transient (as with the synchronous model), and continued to increase from transient to steady-state ($\langle CC \rangle = 0.163$ transient, 0.314 steady-state, $P = 3.57E^{-8}$ for transient–steady-state comparison, Wilcoxon signed-rank test, fig.S4.7a), as network oscillations became increasingly coherent. In the asynchronous model, $\langle CC \rangle$ significantly increased from ongoing to transient ($\langle CC \rangle = 0.002$ ongoing, 0.033 transient, $P = 1.5E^{-4}$ ongoing–transient comparison, Wilcoxon signed-rank test, fig.S4.7b), although the change was much smaller than in the synchronous model (fig.4.5d). And in sharp contrast to the synchronous model, synaptic adaptation did not have a significant impact on $\langle CC \rangle$ ($\langle CC \rangle = 0.028$ steady-state, $P = 0.48$, Wilcoxon signed-rank test). Thus, gamma-band membrane potential correlated variability in the model network is inextricably linked to network spike rate oscillations.

Network oscillations determine synaptic input correlations. As described in the Results and Discussion sections, membrane potential correlations are strongly influenced by correlations in synaptic inputs. As such, we investigated correlated variability between excitatory (g_e–g_e CC), and inhibitory (g_i–g_i CC) synaptic conductances for pairs of excitatory

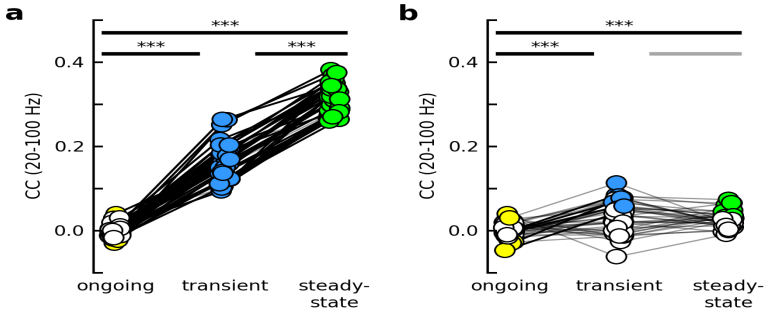

Figure S4.7: **Network spike rate oscillations increase gamma-band membrane potential correlated variability, and synaptic adaptation reduces correlated variability by abolishing oscillations.** (a) Same as in fig.4.5d, but for synchronous model without synaptic adaptation. Removing synaptic depression causes oscillations to become increasingly coherent, and correlated variability increases further from transient to steady-state. (b) Same as in (a), but for asynchronous model with synaptic adaptation. In the absence of network oscillations, the initial increase in correlated variability is much smaller, and CC does not decrease significantly from transient to steady-state, despite synaptic depression.

neurons the model, as well as correlations between excitatory and inhibitory conductances (g_e–g_i CC). Because CC can be shaped by the lag between excitation and inhibition, we calculated g-g CC as a function of lag. To better understand how these are shaped by network oscillations, we did this for the synchronous and asynchronous models (described above), using 40 pairs generated from 20 neurons randomly-selected from the entire network. For the synchronous model, we the same neurons and trials as in the Results section.

For both models, g_e–g_e $\langle CC \rangle$ was relatively small during both the transient and steady-state epochs (and larger for the synchronous than asynchronous model, fig.S4.8a). In contrast, g_i–g_i CC was large for both models (and larger for the synchronous model), and only decreased slightly from transient to steady-state (fig.S4.8b). The disparity between correlations for these two conductance types likely reflects the stronger, more densely

interconnected, and spatially-independent inhibitory synapses (see Methods), and is consistent with earlier experimental recordings of excitatory and inhibitory conductances during gamma oscillations [233,234].

Strong g_i–g_i (and/or g_e–g_e) correlations alone are not sufficient to guarantee large membrane potential correlations; if excitation and inhibition are perfectly phase-locked, they will cancel at the level of the membrane potential, resulting in small membrane potential correlations. In the synchronous model, g_e–g_i CC was large, and peaked at -6 ms (fig.S4.8c, d, left), indicating a lag between the two conductances. In the asynchronous model, g_e–g_i CC was smaller, and peaked instead at -2 ms (fig.S4.8c, d, right). The dynamics of correlated variability in the synchronous model can thus be understood in the context of synaptic inputs. During the transient epoch, excitatory inputs to pairs of neurons are weakly, but significantly correlated. Inhibitory inputs are much more strongly correlated with one another, and also with the excitatory inputs. Crucially, the lag between excitation and inhibition allows for a "window of opportunity" during each cycle of the oscillation in which g_e–g_e and g_i–g_i correlations are independently manifested in pairs of membrane potentials. During the steady-state, correlations between inhibitory inputs and between inhibitory and excitatory inputs are only moderately reduced. However, correlations between excitatory inputs have decreased to near zero for many pairs, and thus V-V correlations across the population decrease significantly.

The distance-dependence of correlated variability reflects the spatiotemporal dynamics of network spiking. The results in the main text were calculated for forty pairs generated from 20 neurons randomly-selected from the entire network of 800 excitatory neurons. We tested the

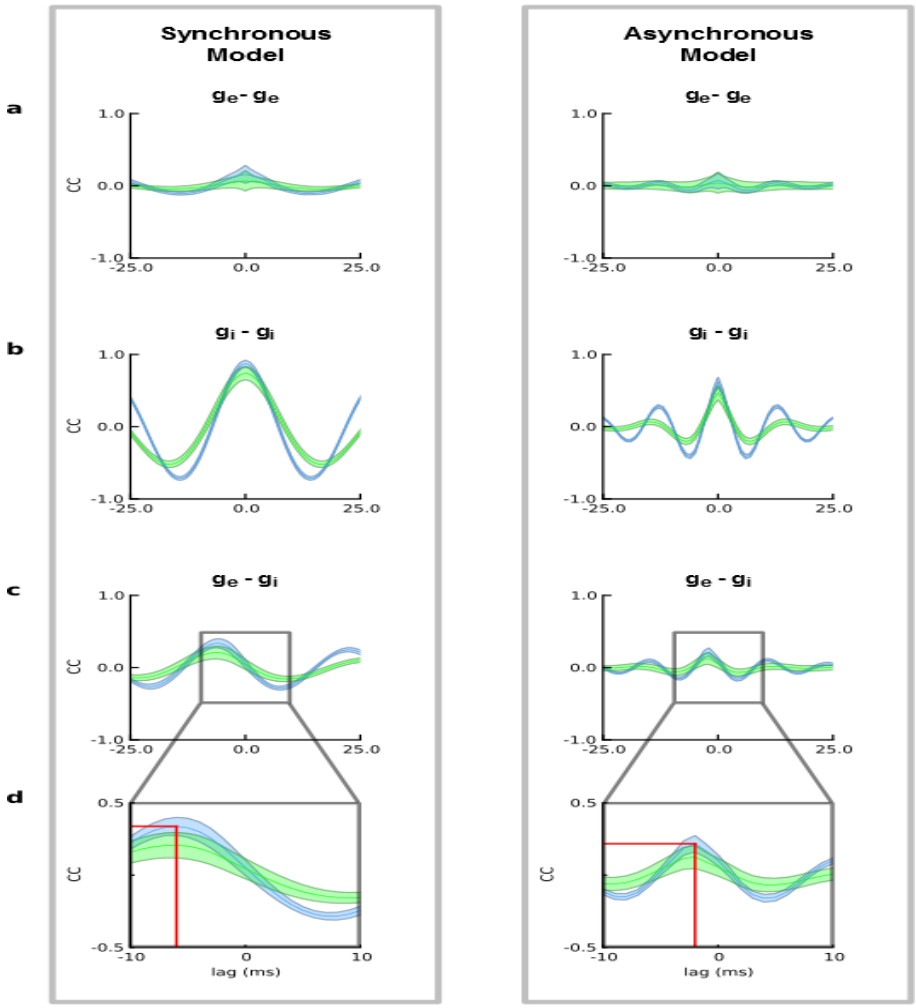

Figure S4.8: **Network oscillations shape synaptic input correlated variability.** (a c) Correlated variability of synaptic conductances as a function of lag for the transient (blue) and steady-state (green) epochs, for the synchronous (left) and asynchronous (right) models (average +/- standard deviation, with average taken over trials and pairs, and standard deviation taken over pairs). Results calculated for inputs to forty pairs generated from twenty neurons randomly-selected from 800 excitatory neurons. Correlated variability is calculated for pairs of excitatory (a) and inhibitory (b) synaptic conductances, and for excitatory-inhibitory synaptic conductance pairs (c). (d) Close-up view of (c). Red lines indicate maximum transient CC values, and lag at which the maxima occur. In general, synaptic conductance correlations are stronger (have larger maximum amplitude) in the synchronous model. Crucial to membrane potential correlations is the larger excitatory lag in the synchronous model (6 ms vs. 2 ms, (d)).

dependence of CC dynamics on average distance between neurons by repeating the analysis for 20 neurons randomly-selected from a group of 100 neighboring neurons (fig.S4.9b, top), and also for 20 neighboring neurons (fig.S4.9c, top).

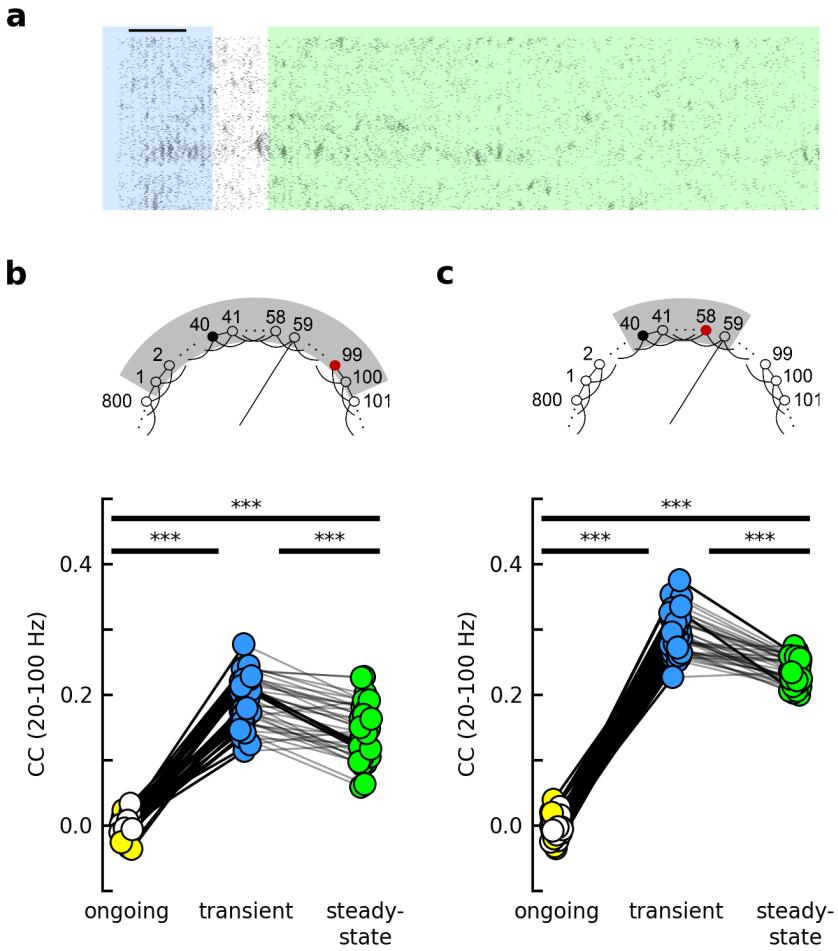

Figure S4.9: **The distance-dependence of V-V CC reflects the spatiotemporal dynamics of network spiking.** (a) Evoked spiking activity for all 800 excitatory neurons (arranged in order of neuron number, or location in network) for one trial. Blue and green regions indicate transient and steady-state epochs, respectively. Scale bar indicates 200 ms. (b) Top: twenty neurons were randomly-selected from 100 neighboring neurons in the network. Bottom: Same as in fig.4.5d, but for neurons selected from cluster of 100. (c) Top: twenty neighboring neurons were selected from the network. Bottom: Same as in fig.4.5d, but pairs generated from 20 neighboring neurons.

For pairs from the group of 100 neurons, evoked $\langle CC \rangle$ was larger than when neurons were selected from the entire excitatory network ($\langle CC \rangle = 0.192$ transient, 0.144 steady-state, fig.S4.9b, bottom). Values were larger still for pairs generated from 20 neighboring neurons ($\langle CC \rangle = 0.294$ transient, 0.237 steady-state, fig.S4.9c, bottom). In addition,

across-population CC variability for a given evoked epoch decreased with pool size. Interestingly, the modulation of $\langle CC \rangle$ by adaptation (that is, the proportional decrease in $\langle CC \rangle$ from transient to steady-state) also decreased: $\langle CC \rangle$ decreased by 31.5% for neurons selected from the entire excitatory network, by 25% for those selected from the group of 100, and by 19% for the group of 20. This reflected the spatiotemporal dynamics of network spiking activity. During the transient epoch, spiking activity tended to be correlated across the network (thus increasing CC even for pairs of neurons separated by large distances). While adaptation reduced network spiking levels and correlated spiking generally, brief episodes of coherent spiking activity often appeared during the steady-state, during which spiking was far more correlated among nearby neurons than across the population (fig.S4.9a). Thus, correlated variability decreased from transient to steady-state for most pairs, but was more strongly diminished for distant pairs.

4.6.6 Supplementary Information 6: Use of "test neurons" to calculate correlated variability in a model network

Individual neurons in our model network had much higher post-stimulus spike rates than those recorded in experiment. Because of the limited network size, this higher spike rate was necessary to generate large avalanches of activity. That is, a large number of synaptic inputs were required to bring a neuron to spike threshold, and in this small network, those inputs necessarily came from a larger percentage of the total network than in a more realistic sparse-spiking network. This is a common issue with small LIF networks [56]. Importantly, this higher spike rate has implications for calculating V-V correlated variability: replacing spikes requires interpolation, which tends to mask synaptic inputs.

We sought to avoid this issue while maintaining reasonable simulation times. Therefore, to calculate CC for a pair of neurons in this network, we fed re-scaled versions of the synaptic conductances to "test" LIF pairs. Specifically, all conductances were multiplied by 0.75. In addition, the spike threshold of test neurons was -30 mV (vs. -40 mV in network neurons), thus reducing the probability to spike. Test neurons were identical to network neurons in all other respects. Thus, test neurons subsampled network spiking activity without reaching action potential threshold. All reported CC values for the model were calculated using such test pairs. In this way, each neuron in the model network can be thought to represent the net spiking output of a small cluster of neurons in a large, more sparse-spiking network. This implicitly assumes that individual cortical neurons fire sparsely and variably across trials, but clusters of such neurons are more reliable. We have (unpublished) MEA data that loosely supports this assumption. Specifically, a given stimulus presentation tends to evoke a rhythmic LFP oscillation at a given electrode (suggesting synchronous activity near the electrode tip), yet spikes recorded from the same electrode (corresponding only to neurons very near the electrode) are sparse when present. In addition, the receptive field defined by spiking activity tends to be correlated with that defined by the LFP, suggesting that each sparse-spiking unit in the cluster follows a similar dynamic when spiking. This is consistent with a picture of a relatively reliable cluster of neurons composed of sparse-spiking and less reliable individual units. This is a common experimental observation, and is captured by LIF network models such as the ones used in this study [52].

Chapter 5

State Dependence of Correlated Variability in Local Field Potentials

Mahmood S. Hoseini*[1], Nathaniel C. Wright[1], Wesley Clawson[2], Woodrow Shew[3], Ralf Wessel[1]

[1]Department of Physics, Washington University, St. Louis, MO

[2]Department of Electrical Engineering and [3]Department of Physics, University of Arkansas, Fayetteville, AR

Contact information: Corresponding author email - sayedmahmood@wustl.edu

This work is in preparation for the Journal of Neuroscience

5.1 Abstract

Neural response in sensory cortex to repeated stimulus presentation is highly variable. The trial-to-trial variability and the extent to which this variability is shared among neurons have a strong impact on the population coding accuracy. To investigate the nature/source of this variability, we recorded local field potential (LFP) in the primary visual cortex (V1) of turtles in response to naturalistic movies. We found that across-trial average captures a large fraction of the variability in early part of the responses while across-electrode average is a better estimator of both ongoing activity and late part of the responses. In addition, recordings show a strong correlated variability (or "noise correlation") that transiently increases with the stimulus onset. More importantly, we found that LFPs have a strong, shared fluctuations that accounting for them markedly reduces correlated variability. Our model investigations indicated that intra-cortical adaptation self-organizes cortical circuits towards a balanced regime at which network dynamically subdivides into clusters that leads to experimentally-observed variability and an intermediate coordination level.

5.2 Introduction

The response of neurons in visual cortex to repeated stimulus presentations is highly variable. This trial-to-trial variability can be as large as the response itself [209, 235, 236]. Cortical neurons can generate highly reliable spike trains [237], therefore variability of their output is more likely due to variability in their synaptic inputs [209, 238]. Synaptic inputs must be, at least partially, shared across neurons due to the interconnected nature

of the cortex [84, 199]. To crack the code of sensory processing in the cortex, it is essential to understand how response variability arises, to what extent it is shared across neuronal populations, and what factors influence it. Indeed, the presence of variability has profound implications for the brain computational power [239], while excessive variability poses a fundamental problem for information processing [240].

Stimulus presentation elicits variable responses in lateral geniculate nucleus [241] and the variability is carried out to the cortex [242]. However, cortical responses are shown to be more variable than LGN [243] and, therefore, there should exist other sources of variability intrinsic to the cortex. A portion of the variability is due to processes internal to single neurons, such as transmission noise in synapses and channel noise in membranes [244]. A factor that influences cortical response, but it is not known to the experimenter, is the state of the cortex [245, 246]. The cortex can exhibit a continuum of states from strong synchronization to complete desynchronization [247, 248], which are not linked to the visual stimulus [245].Despite being studied extensively, the relative contribution of cortical states in response variability is still unclear [249]. How does it affect the variability in population response during visual processing?

To gain insight on response variability and its correlation structure, we recorded local field potential (LFP) with a microelectrode array in primary visual cortex. Network state estimation using the LFP enabled us to decompose response variability into stimulus-dependent and network-state dependent components. Our results indicated that, except early phase of the response, shared fluctuations (due to network state) could explain a larger portion of the response variability relative to the stimulus itself. Moreover, correlated variability significantly increases with stimulus onset and then adapts toward an

intermediate level. Indeed, correcting the neural responses for the effects of network-state highlights this dynamics more.

5.3 Results

To quantify response variability and its correlation, we recorded population neural activity (local field potential, LFP) using a microelectrode array (MEA) inserted into the geniculo-recipient dorsal cortex (visual cortex) of the turtle eye-attached whole-brain ex vivo preparation during visual stimulation of the retina (fig.5.1a). Unlike ongoing activity, evoked responses are characterized by extensive fluctuations across MEA. Visual responsive channels were identified and used for analyses (fig.5.1b, see Methods).

5.3.1 Across-trial average captures most of the variability in transient epoch

We recorded neural activity from 11 turtle eye-attached whole-brain ex vivo preparations while presenting continuous visual stimulation (see Methods). LFP responses to repeated presentations of extended stimuli varied from trial to trial, with a response variability magnitude as large as trial-averaged mean response (fig.5.2c). What factors contribute to the variations from the mean response?

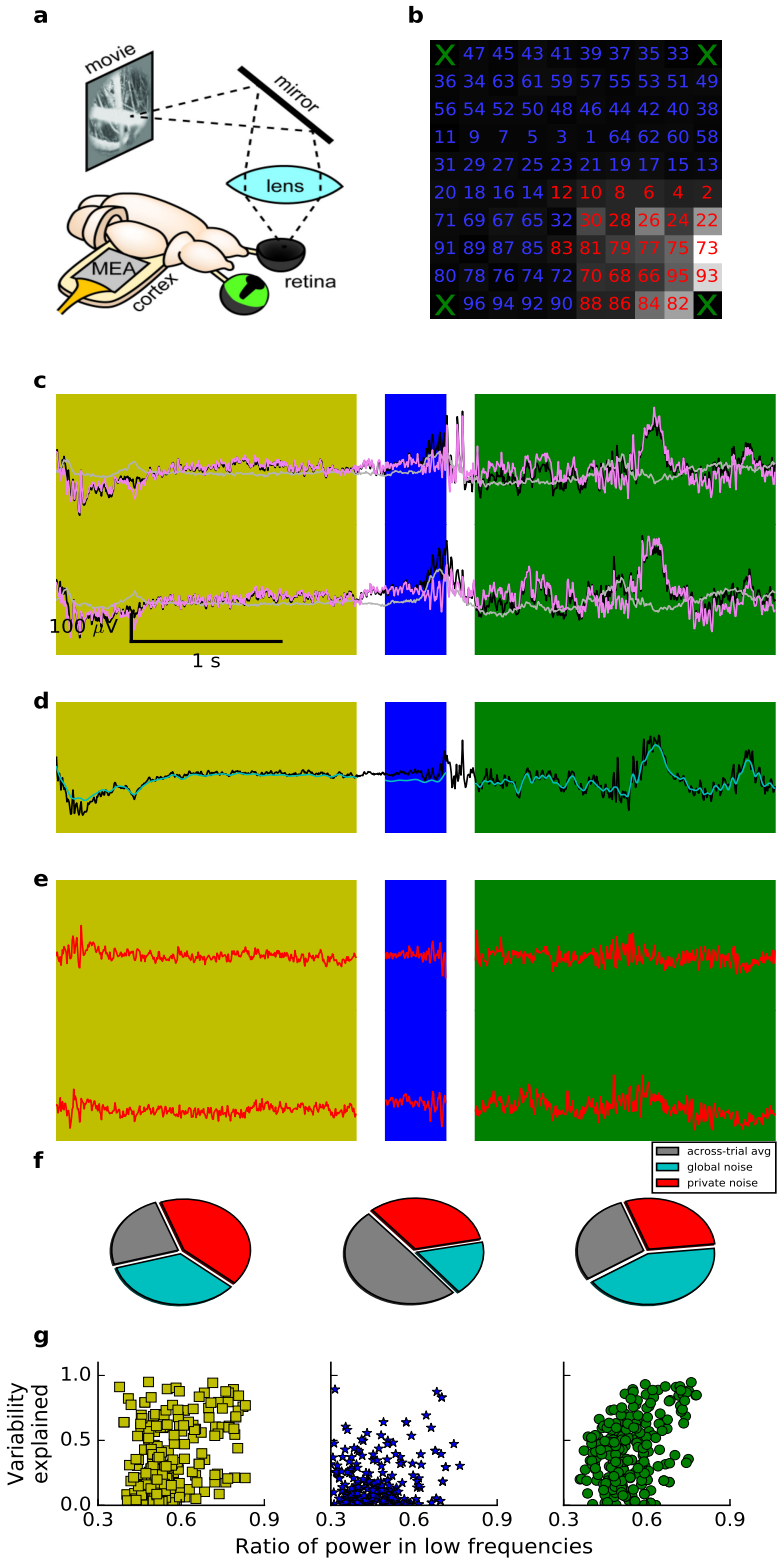
a
movie
mirror
lens
MEA
cortex
retina
b
X 47 45 43 41 39 37 35 33 X
36 34 63 61 59 57 55 53 51 49
56 54 52 50 48 46 44 42 40 38
11 9 7 5 3 1 64 62 60 58
31 29 27 25 23 21 19 17 15 13
20 18 16 14 12 10 8 6 4 2
71 69 67 65 32 30 28 26 24 22
91 89 87 85 83 81 79 77 75 73
80 78 76 74 72 70 68 66 95 93
X 96 94 92 90 88 86 84 82 X
c
100 μV
1 s
d
e
f
across-trial avg
global noise
private noise
g
Variability explained
1.0
0.5
0.0
0.3
0.6
0.9
Ratio of power in low frequencies

Figure 5.1: **Variability in the transient epoch has a different nature than ongoing and steady-state.** (a) Our experimental set up for experiments done with a monitor and mirror. The visual stimuli are presented on a monitor. The image reflects off a mirror and through a lens to project on the retina of the turtle's hemisected eye. The MEA is placed in the unfolded cortex. (b) Visual responsiveness across the MEA. Each square represents an electrode. The background color for each square indicates the visual responsiveness with black being 0 and white being 1. The electrodes labeled in red have a visual responsiveness above the threshold, 0.75, to be included in analyses. Electrodes labeled in blue showed weak responses and excluded from later analyses. (c) Single-trial responses for two electrodes are shown (black) with their across-trial averages (gray) and their difference as residuals (violet) during three epochs; ongoing (yellow), transient (blue), and steady-state (green). Across-trial average captures single-trial features during the transient epoch while averaging washes out features of the other two epochs. (d) Across-electrode average is shown (black) with shared fluctuations (cyan) estimated for the epochs. Shared fluctuation trace explains slow changes during ongoing and steady-state, while it remains almost constant during transient epoch. (e) Accounting for shared fluctuations leads to less variable signals. Shown are residuals shown in (c) after accounting for the shared component. (f) Portion of the variability explained by each component–across-trial average (gray), shared fluctuation (cyan), and private noise (red)–during the three epochs. Across-trial average explains a large fraction of the total variability during transient epoch, while shared fluctuations have a greater contribution during the other two epochs. (g) Variability explained by the shared fluctuations is related to the ratio power in low-frequency ($<$ 20 Hz) band in ongoing and steady-state(ongoing: $\rho = 0.32$, $P < 1E^{-6}$, Spearman's test; transient: $\rho = 0.03$, $P = 0.61$; steady-state: $\rho = 0.31$, $P < 1E^{-6}$).

Using the amplitude of deflections, we identified responsive channels to include in subsequent analyses (see Methods). To quantify sources of variability, we first calculated the LFP residual, which is the single-trial LFP recording from which the trial-averaged LFP time series has been subtracted (fig.5.1c). We then divided the evoked residuals into two analysis windows: the transient (200 to 600 ms after stimulus onset) and steady-state (800 to 2800 ms after stimulus onset) windows (fig.5.1c, see Methods, and see Supplementary Information 1). We used single-trial across-channel average residual LFPs to decompose neuronal activity into network-state dependent (shared) and private noise components (fig.5.1d, see Methods). We used Gaussian-process factor analysis (GPFA) model to estimate smooth, low-dimensional neural trajectory as shared noise component [245, 246, 250]. Finally, we subtract shared noise component from the residuals

(fig.5.1e) and, then, we calculated the variability explained by each component across epochs, trials, and channels (see Methods).

The analysis revealed two important features concerning the fraction of variability explained by three components–across-trial average, shared fluctuation, and private noise–in LFPs during natural vision. First, across-trial average captures a great portion of the variability during the transient epoch (fig.5.1f; ongoing: 19%, 30%, 51% for across-trial average, shared fluctuations, and private noise respectively, ANOVA, $P < 1E^{-6}$; transient: 40%, 14%, 46%, ANOVA, $P < 1E^{-5}$; steady-state: 26%, 40%, 34%, ANOVA, $P = 0.1$). It indicates that dynamics of the transient epoch can be largely explained by the statistics of the thalamic inputs to the cortex [190,202,238,251,252]. Second, stimulus-independent components mainly drive the dynamics in steady-state epoch (fig.5.1f), and, more importantly, network-state captures most of the variability in residual LFPs. This indicates that there might exist more than one state (a condition called bi- or multistability), and visual stimulation may just switch the state of the brain dynamics [205,206,253,254]. These conclusions held for 8/11 turtles and 3 types of visual stimuli (n=13 data sets; naturalistic movie and motion enhanced movies as well as its phase shuffled version; see fig.S5.1), demonstrating the generality of the observations. Furthermore, results were largely robust with respect to the choices of window sizes and gaps between windows (see fig.S5.2).

5.3.2 Accounting for the global fluctuations reduces noise correlations during ongoing and steady-state epoch

The interconnected nature of cortical circuits suggests that variability is to some extent correlated among recorded signals [191, 199, 201]. It remained to be elucidated, however, to what extent the shared variability structure was explained by the shared fluctuations. To address this question, we calculated trial-average correlation coefficient (CC) between residual LFPs, with and without correcting for global fluctuations, for each trial and window of interest, i.e., the ongoing, transient, and steady-state windows. We took into account the full frequency range (0.7 – 100 Hz; see (see Supplementary Information 2) and fig.S5.3). Population-average CCs ($\langle CC \rangle$) distributed broadly and were significantly nonzero across all epochs (0.51, 0.31, 0.62, $P < 1E^{-23}$, ANOVA; fig.5.2a; see fig.S5.4 and fig.S5.5). Moreover, they decreased significantly with the spatial separation between electrodes (fig.5.2c).

Correcting for the shared fluctuations markedly reduces the amplitude of correlations (0.05, 0.17, 0.09, $P = 0.005$, ANOVA; fig.5.2b) while they still decrease significantly with the spatial separation between electrodes (fig.5.2d). There are three noticeable features comparing CC amplitudes before and after accounting for the shared fluctuations. First, accounting for the shared fluctuations reduces CC values for all epochs. Second, ongoing and steady-state CCs are more heavily influenced due to high fraction of variance captured by the GPFA model. Third, CCs increase significantly from ongoing to transient and then decrease from transient to steady-state, in agreement with membrane potential data (see chapter 4). More importantly, correcting for the global fluctuations strengthens

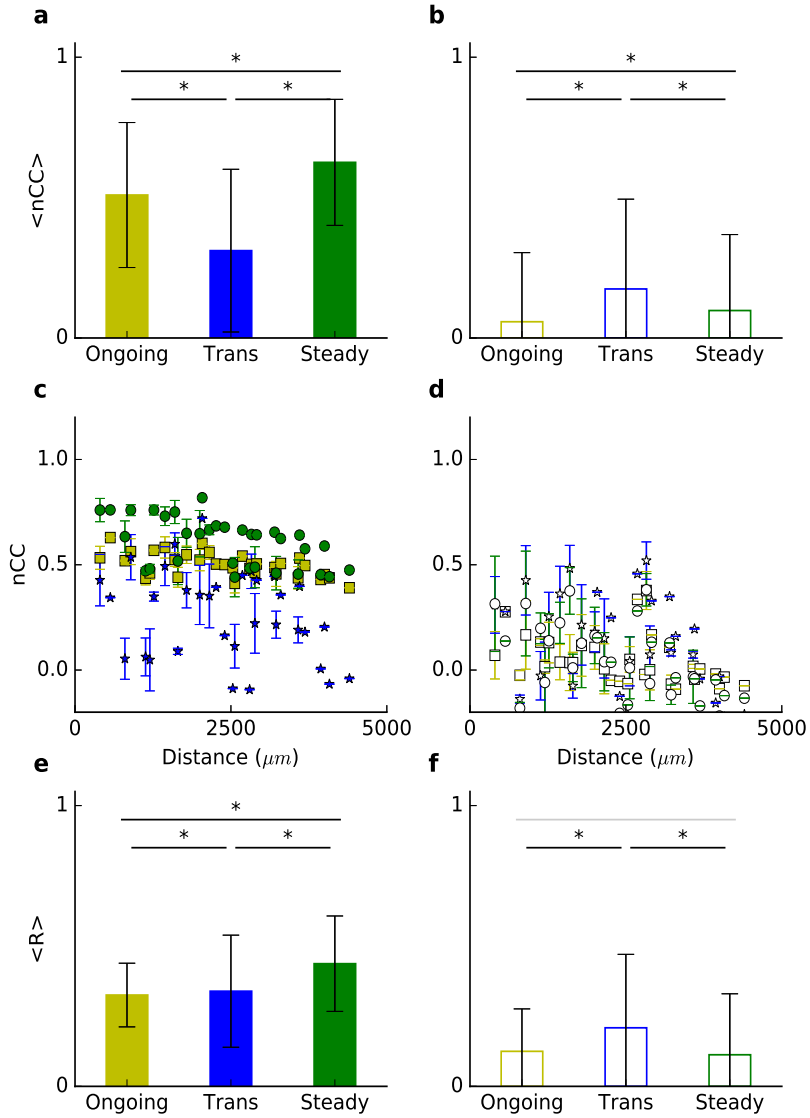

Figure 5.2: **Accounting for shared fluctuations reduces noise correlation amplitude but doesn't change its structure.** (a) Noise correlation significantly decreases from ongoing to transient and then recovers back during steady-state. (b) Noise correlation amplitudes markedly decreased after correcting for the shared fluctuations. (c) Noise correlation decreases with spatial separation between the electrodes (ongoing: $\rho = -0.43$, $P < 0.001$, Spearman's test; transient: $\rho = -0.3$, $P = 0.01$; steady-state: $\rho = -0.57$, $P << 0.001$). (d) Correcting for the shared fluctuations doesn't alter distance dependence of noise correlations (ongoing: $\rho = -0.29$, $P = 0.01$; transient: $\rho = -0.32$, $P = 0.008$; steady-state: $\rho = -0.42$, $P < 0.001$). (e) Population-averaged phase concentration roughly shows the same temporal dynamics as noise correlation. (f) Accounting for the shared fluctuations causes $\langle R \rangle$ to show a significant increase at the stimulus onset.

this observation (residual CCs: 2/16 show a transient increase; after accounting for the global fluctuations: 12/16 show a transient increase; see fig.S5.5a, b).

5.3.3 Correlated variability follows network oscillation dynamics

It has been hypothesized that the coordination between pairs of neurons might be shaped by the amount of phase synchrony as well as anatomical connectivity [190, 191, 194]. We therefore asked how well correlated variability dynamics could be explained by the network phase synchrony. For a pair of analog signal, a popular measure is the phase concentration, which is defined by the cosine of the phase difference of analog signals ([110]; see Methods and chapter 4).

We calculated cosine of phase difference between a pair of residuals, or residuals while accounting for the shared fluctuations, across epochs and frequency bands. Then trial-average phase concentration, R, is obtained by taking average over all trials and window of interest. The phase concentration takes a value of +1 for a pair of perfectly in-phase signals, -1 for perfectly out-of-phase signals, and 0 for two signals with random phase difference. Our results indicated that population-average phase concentration ($\langle R \rangle$) follows the same dynamics as $\langle CC \rangle$ for residuals (0.32, 0.33, 0.43, $P << 0.001$, ANOVA; fig.5.2e) as well as residuals corrected for global fluctuations (0.12, 0.20, 0.11, $P < 0.001$, ANOVA; fig.5.2f). Moreover, changes in CC were significantly related to changes in R for residuals (ongoing–to–transient transition: $\rho = 0.58$, $P << 0.001$ Spearman's test; transient–to–steady-state transition: $\rho = 0.54$, $P << 0.001$; see fig.S5.6a) as well as residuals corrected for global fluctuations (ongoing–to–transient transition: $\rho = 0.68$, $P << 0.001$; transient–to–steady-state transition: $\rho = 0.65$, $P << 0.001$; see fig.S5.6b).

5.3.4 Synaptic clustering mediates the nature of response variability

What biophysical mechanisms could mediate the experimentally-observed response properties (i.e., nature of variability across epochs fig.5.1f), the dynamics of correlated variability (fig.5.2a, b) and of phase concentration (fig.5.2e, f)? To address this question, we investigated a model network of 800 excitatory and 200 inhibitory leaky integrate-and-fire neurons distributed randomly over the surface of a unit sphere, with Poisson process external inputs to all neurons (see Methods). Excitatory neurons make synapses to their neighbor excitatory cells with a Gaussian distribution decaying with spatial separation between neurons, with 10% connection probability (fig.5.3a). The rest of the connections were random (fig.5.3b). Synaptic weights are drawn from a gamma distribution with a long tail [255].

An increase in the external input rate mimicked the stimulus. Synaptic currents obey alpha function dynamics with reasonable sets of rise and decay times ([52, 58]; see Methods). We implemented adaptation via short-term synaptic depression with recovery (see Methods). Defining LFPs as the summation over synaptic currents to a population of excitatory neurons, we simulated the network in response to 20 repeated stimulus presentations. Using GPFA model, we estimated the network-state across three epochs and subtracted it from the individual LFPs to get private noise traces. This network reproduces the fraction of variance explained by each component (fig.5.3c) and correlation between global fluctuation's share and low frequency power (see fig.S5.7).

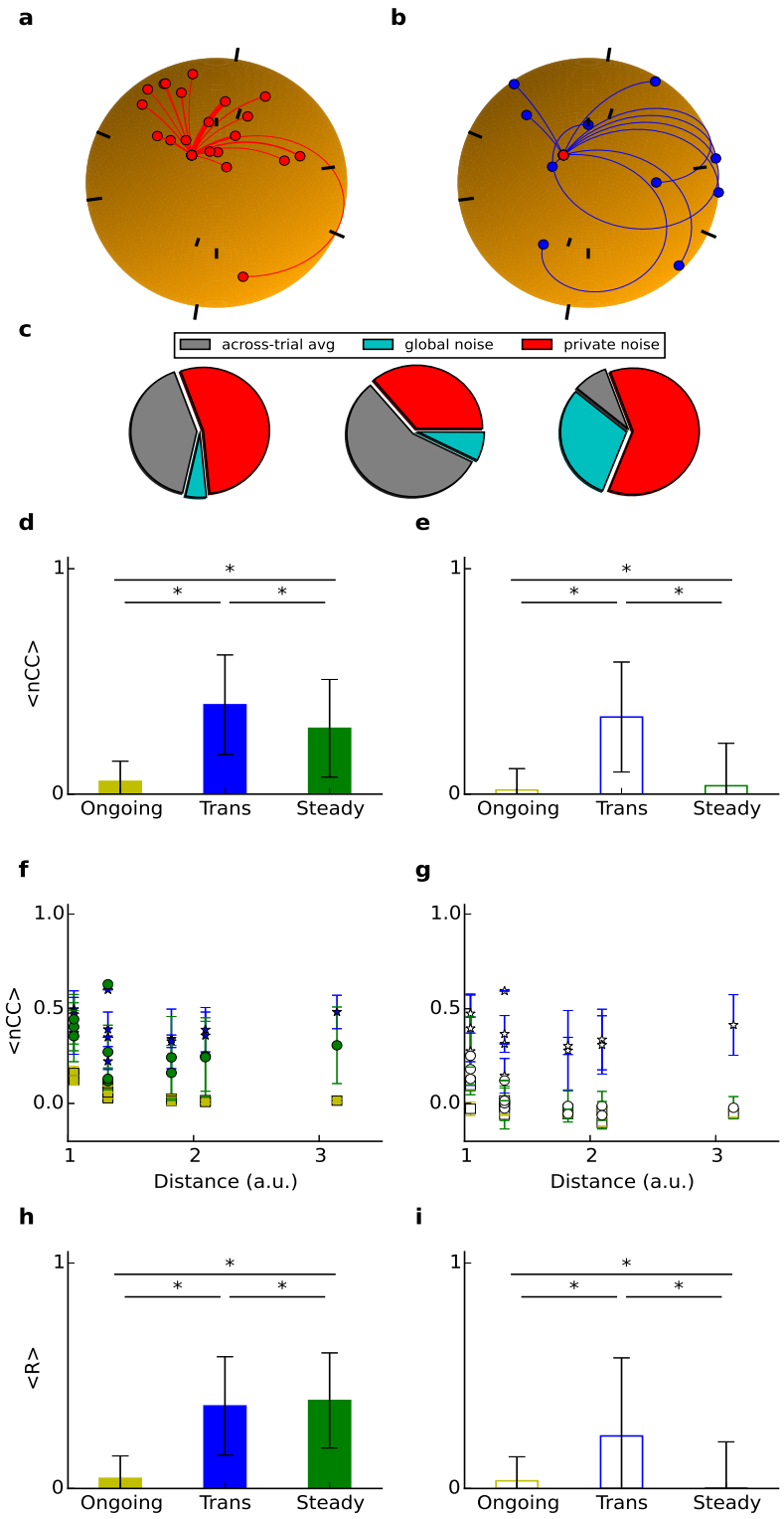
a
b
c
across-trial avg
global noise
private noise
d
e
<nCC>
1
0
*
Ongoing
Trans
Steady
f
g
1.0
0.5
0.0
Distance (a.u.)
h
i
<R>

Figure 5.3: **A network with clustered architecture reproduces experimentally-observed nature of variability and noise correlation.** (a) E-to-E connections are clustered with sporadic long-range connections. Excitatory synaptic connections to a given excitatory cell are shown with connection strength indicated in the thickness of the line. Black bars indicate the imaginary electrodes. (b) Inhibitory inputs to the excitatory cell shown in (a). I-to-E connections are homogenously random such that an inhibitory neuron can project to any excitatory cell. (c) Portion of the variability explained by each component during the three epochs. Across-trial average explains a large fraction of the total variability during transient epoch, while shared fluctuations have a greater contribution during steady-state (ongoing: 41%, 5%, 54% for across-trial average, shared fluctuations, and private noise respectively, ANOVA, $P << 0.001$; transient: 57%, 7%, 36%, ANOVA, $P << 0.001$; steady-state: 9%, 30%, 61%, ANOVA, $P << 0.001$). (d) Noise correlation significantly increased from ongoing to transient and then decays during steady-state. (e) Noise correlation amplitudes markedly decreased, especially during steady-state, after correcting for the shared fluctuations. The correction highlights transient $\langle CC \rangle$ increase with stimulus onset. (f) Noise correlation decreases with spatial separation between the electrodes (ongoing: $\rho = -0.81$, $P << 0.001$, Spearman's test; transient: $\rho = -0.14$, $P = 0.34$; steady-state: $\rho = -0.20$, $P = 0.17$). (g) Correcting for the shared fluctuations doesn't alter distance dependence of noise correlations (ongoing: $\rho = -0.49$, $P < 0.001$; transient: $\rho = -0.08$, $P = 0.59$; steady-state: $\rho = -0.53$, $P < 0.001$). (h) Population-averaged phase concentration roughly shows the same temporal dynamics as $\langle CC \rangle$ in (d). (i) Accounting for the shared fluctuations reduces $\langle R \rangle$ during steady-state and causes $\langle R \rangle$ to show a significant increase with the stimulus onset.

Our investigations, in line with our previous study (see chapter 4), indicated that experimental observations could be reproduced if network has the following features. First, excitation and inhibition should have different time course. When synaptic time constants for excitation and inhibition were chosen not to be identical, the lag between excitation and inhibition provides a window of opportunity in which synaptic input correlations could be manifested in pairs of recordings [84, 190]. This causes an increase in noise correlation as well as phase concentration (fig.5.3d, e, h, and i). Changes in noise correlation are tightly related to the changes in phase concentration (see fig.S5.6a, b). Second, two factors are responsible for the significant $\langle CC \rangle$ decrease from transient to steady-state epoch, synaptic depression and clustering structure. Synaptic depression diminishes network activity level by weakening interactions, which yields that coherent oscillations occur within one or a few clusters during steady-state epoch (see chapter 4). Clustering

architecture of the network, together with synaptic depression, abolishes oscillations in the network and causes a decrease in $\langle CC \rangle$ values via the following mechanism. Stimulus onset triggers oscillations that invade the whole network and that has two impacts, (i) causes an upward modulation in $\langle CC \rangle$ since oscillations are coherent and (ii) causes across-trial average to capture a large fraction of variability during transient epoch since this amplification is consistent across trials. Moreover, clustering architecture introduces a spatial dimension into the network and reproduces distance dependence of CCs (fig.5.3f, g). Consistent with this view, a homogenous random network was able to explain the different nature of response variability but not the dynamics of $\langle CC \rangle$ or $\langle R \rangle$ (see fig.S5.8). Third, gamma distribution of the synaptic weights doesn't change any of the results except the amount of variability seen in $\langle CC \rangle$ and $\langle R \rangle$. In other words, a similar network with uniform distribution of weights, but still with clustered architecture, was able to reproduce the results.

In conclusion, model investigations strengthen the hypothesis that thalamocortical oscillation are the key factor in reproducing experimental observations and, more importantly, clustering architecture shapes spatiotemporal dynamics of neural responses. Correlated variability follows network oscillation dynamics, such that constraining network model to produce realistic temporal dynamics of oscillations yields to transient increase in $\langle CC \rangle$. Therefore, synaptic time constants, synaptic clustering, and synaptic depression are intrinsic parameters relevant in reproducing experimental data.

5.4 Discussion

Neural responses in visual cortex markedly vary from trial to trial under similar stimulus condition. To study the source of the trial-to-trial variability and the extent to which it is shared between neurons, we recorded ongoing and visually-evoked activity in turtle eye-attached whole-brain *ex-vivo* preparations. Our analysis showed that the nature of variability is different between "early" and "late" responses. Immediately after stimulus onset, across-trial average is good estimator of individual single-trial LFP signals, while single-trial LFP of both ongoing and late evoked responses for continued visual stimulation can be better explained by across-channel average of that trial. This study provides a crucial evidence to strengthen the hypothesis that cortex may have more than one stable state, and visual stimulation may just perturb it while intracortical interactions shape neural responses [205, 206, 253, 254]. Furthermore, in a computational model, we identified minimal network parameters–synaptic time constants, synaptic clustering, and synaptic depression–necessary to reproduce the key aspects of the experiment.

Neural responses are typically studied by taking across-trial averages. However, this approach fails if the neural responses are more a reflection of internal processing rather than sensory stimulus drive. From this viewpoint, internal state of the brain modulates single-trial neural responses in a similar manner and leads to the emergence of shared fluctuations. To estimate the global fluctuations, a latent variable method (GPFA) has shown to be greatly useful [250]. This analysis is particularly helpful in reconciling the apparent controversy about the amplitude of correlated variability. Strikingly different results for correlated variability has been reported [195, 200, 222, 256–259], which cannot be explained with differences in firing rate (e.g. see Smith and Kohn, 2008; Ecker et al., 2010).

Moreover, LFP has proven as a powerful indicator of the network-wide fluctuations that can pave the way for spike-train factorization into stimulus-dependent and independent components [245]. Estimation of network-state is more accurate in our study relative to previous work [245] by using a more sophisticated model and, importantly, by including the full grid of LFP signals. Our results demonstrate that GPFA model can extract the hidden information in the LFP to decouple these components (fig.5.1c, d) and provides the opportunity to quantify the contribution of each component in the trial-to-trial variability of the responses (fig.5.1f). We found that across-trial average explains a large fraction of variability during early part of the response while shared fluctuation captures a larger ratio of the variability for both ongoing activity and late responses (fig.5.1e).

How does shared fluctuation impact the amplitude and structure of correlated variability? There exists a long-standing controversy about the amplitude of noise correlation during wakefulness and anesthesia. Noise correlation amplitude during anesthesia is an order of magnitude larger than wakefulness [256, 260], even for the studies conducted in the same preparation under similar stimulus condition [256, 259]. Accounting for shared fluctuations alters noise correlation amplitude but not structure and alleviates the striking differences between the level of noise correlation during wakefulness and anesthesia [246]. Ecker and colleagues reported that accounting for the shared fluctuations reconciles this. Not surprisingly, our results indicate a significant decrease in amplitude by accounting for shared fluctuations (fig.5.2a, b), while correlation structure remains unchanged (fig.5.2c, d). While the raw correlation shows a significant increase with stimulus onset, accounting for shared fluctuations strengthens this trend (fig.5.2a, b). Moreover, our findings indicate that phase concentration was modulated similarly and, indeed, this is non-trivially related to correlation (fig.5.2e, f).

What combination of biophysical ingredients of a model network can generate the experimentally-observed features? We addressed this question by developing a network of leaky integrate-and-fire neurons. The investigation revealed that time course of the synaptic currents, synaptic depression and recovery, and network architecture are the relevant underlying variables. Reasonable synaptic time constants cause ensemble oscillations to appear through the interaction of excitatory and inhibitory neurons [52, 58]. Stimulus onset triggers coherent oscillations and it leads to the observed dynamics in both noise correlation (fig.5.3d, e) and phase concentration (fig.5.3h, i). Synaptic depression reduces activity level as well as interaction strength between the neurons. Therefore, later in time, spatially confined surge of activity happens within one or a few of the clusters. As a result, noise correlation decreases as well as phase concentration. In addition, clustering architecture of the network provides a substrate for the neurons to influence their targets within the same cluster even after the operation of synaptic depression. Having less clustered connections leads to more global oscillations during ongoing and steady-state epochs, which impairs the temporal dynamics of noise correlation and phase concentration.

Here, we focused on the nature of variability during early and late visual responses and we noticed that shared fluctuations are more prominent during late responses. This suggests a crucial role for intracortical connectivity during this phase of the response. Therefore, it is reasonable to ask whether accounting for the shared component can either improve or impair discriminability of stimuli. Future experiments can be designed to address this question while, for the simulated network, a linear decoder seems suitable [196] to quantify the change in information due to amplitude change in noise correlation by accounting for the shared fluctuations.

5.5 Methods

5.5.1 Ex vivo eye-attached whole-brain preparation

All procedures were approved by the Institutional Animal Care and Use Committees of both Washington University and University of Arkansas, and conform to the guidelines of the National Institutes of Health on the Care and Use of Laboratory Animals. Adult red-eared sliders (Trachemys scripta elegans, 150 – 1000 g weight, 12 – 15 cm carapace length) were studied. First turtles were anesthetized with Propofol (2 mg Propofol/kg), then decapitated and the brain was removed surgically from the skull with eyes and optic nerve intact. Right eye was hemisected to expose the retina and bathed in cold extracellular saline (in mM, 85 NaCl, 2 KCl, 2 $MgCl_2 * 6H_2O$, 20 Dextrose, 3 $CaCl_2 - 2H_2O$, 45 $NaHCO_3$, bubbled with 95% O_2 and 5% CO_2). Two cuts were made to make unfold the cortex, thus facilitate the subsequent insertion of the microelectrode array. Recordings began 2 – 3 h after induction of anesthesia.

5.5.2 Microelectrode array measurements

Wideband (0.7 Hz – 15 kHz) extracellular voltages are recorded at 30 kHz sample rate (Blackrock Microsystems, Cerebus) using two different electrode arrays. The first was a 96-channel MEA (1010 square grid, 400 μm inter-electrode spacing, 500 μm electrode length, no corner electrodes, Blackrock Microsystems). This array was inserted to a depth of 250 – 500 μm using a micromanipulator (Sutter, MP-285) with the plane of electrodes parallel to the dorsal surface of the cortex. The second array was a three-dimensional (3D)

grid of electrodes (448 grid, 16 shanks, 8 electrodes per shank, 300 μm inter-shank spacing, 100 μm inter-electrode spacing on each shank, Neuronexus) and was inserted to a depth such that electrodes spanned the cortex from the ventricular to the dorsal surface. We analyzed data from maximum of one electrode per shank. With post-processing filtering (bandpass 5 – 100 Hz) we extracted the local field potential (LFP).

5.5.3 Visual stimuli

Visual stimuli were delivered with either a video projector (Aaxa Technologies, P4X Pico Projector) or an LCD monitor (Samsung 19", $1,440 \times 900$ pixels, contrast ratio=20,000:1, response time = 2 ms) to the retina (fig.5.1a). Visual stimuli are: a naturalistic movie ("CatCam"), a motion-enhanced movie (courtesy Jack Gallant), black moving dots on a white background, and uniform black to gray transition. The mean irradiance at the retina was 1 W/m^2 for the projector and 20 mW/m^2 for the monitor. In all cases, the stimulus was triggered using a custom Labview program (National Instruments).

5.5.4 Identifying responsive channels

To identify responsive channels and include them in analyses, we quantify the level of spontaneous activity on each electrode by averaging over a 4 s time window preceding to stimulus onset. Then we take responses over a 4 s window immediately following the onset of the stimulus, and we define the normalized difference of these two quantities as a measure of responsiveness. We classify an electrode as visually responsive if the ratio is greater than 0.75 (fig.5.1b).

5.5.5 Gaussian-Process Factor Analysis

Gaussian-Process Factor Analysis (GPFA) has been proposed as a method to extract smooth, low dimensional neural trajectories in single-trial simultaneously recorded spike trains19. This low-dimensional trajectory reflects slow time evolution of the internal state of the network and, therefore, it captures a portion of the variability that is shared among many of the neurons. GPFA has several advantages over existing dimensionality reduction methods that have been used to extract neural trajectories (e.g. principle component analysis [261, 262]). The main advantage, in our opinion, is that GPFA has a noise model embodied and thus can distinguish between spiking noise and neural state variability (for a complete discussion see Yu et al. 2009).

GPFA models the neural data with a low-dimensional Gaussian distribution corrupted with private noise.

$$Y_j^{trial}(t) =< Y_j^{trial}(t) >_{trial} + C_j.X^{trial}(t) + \eta_j^{trial}(t) \tag{5.1}$$

where $Y_j^{trial}(t)$ is the single-trial response recorded for neuron j, $< Y_j^{trial}(t) >_{trial}$ is across-trial average as a stimulus impact estimate on each, $X^{trial}(t)$ is the network state, C_j is the coefficient that determines the strength of network state impact on each neuron, and η_j^{trial} is the private noise signal. The network states at different time points are related through Gaussian processes, $X^{trial} \sim N(0, Q^{trial})$ with Q^{trial} as covariance matrix, which implies that the network state trajectories should be smooth. The parameters of the GPFA model can be fit using expectation-maximization (EM) algorithm in such a way that it maximizes the probability of the observed data [250], $Y_j^{trial}(t)$.

LFP traces can be used to estimate global network fluctuations [245]. However, since LFP has a significant component of activity due to stimulus presentation, we subtracted the mean LFP across repeated trials from each trial's data to obtain residuals and then use residuals to compute the network state.

5.5.6 Explained variability

Variability explained by across-trial average response is given by [263, 264]

$$VE = 1 - \frac{var(Y_j^{trial} - < Y_j^{trial} >_{trial})}{var(Y_j^{trial})} \tag{5.2}$$

In similar manner variability explained by the global noise component is defined by

$$VE = 1 - \frac{var(Y_j^{trial} - C_j.X^{trial})}{var(Y_j^{trial})} \tag{5.3}$$

5.5.7 Correlated variability Analysis

As mentioned above, for each single-trial LFP, the residual (or deviation from the average activity) calculated by subtracting the across-trial average time series from the single-trial time series. Network state is estimated using the residuals and were subtracted from residuals to get the private noise signals, $\eta_j^{trial}(t)$. Traces were then separated into three epochs: the ongoing epoch (defined to be the two seconds prior to the onset of visual stimulation), the transient epoch (200 to 600 ms after stimulus onset), and the steady-state epoch (800 to 2800 ms after stimulus onset). Then Pearson correlation between pairs of

responsive channels was calculated for each epoch and trial. The results were averaged across all trials, resulting in the trial-averaged correlated variability (CC) for each pair and epoch. The significance of CC values for a given pair and epoch was determined by either one-sided or two-sided t-test.

5.5.8 Phase Concentration Analysis

For each trial and cell, we extracted a 5.8 s window of residuals and residuals with network state subtracted. To avoid filtering artifacts at the beginning and end of the signal we padded it with two 500 ms traces and later on dropped it. For each trace, we performed wavelet analysis in Matlab using software provided by C. Torrence and G. Compo [107] (available at URL: http://paos.colorado.edu/research/wavelets/). This resulted in a series for the phase of each signal as a function of time and frequency. We then averaged over the entire frequency range (0.7 – 100 Hz) to obtain the phase time series for each trace, $\phi_i(t)$. For each pair, we calculated the cosine of the phase difference, and averaged over each epoch to obtain the "phase concentration" for each epoch and trial: $R^{trial}_{epoch} =< cos[\phi_1(t) - \phi_2(t)] >^{trial}_{epoch}$. We then averaged over all trials and analyzed the results for pairwise and population trends using the same methods as those described for CC values. The phase concentration varies between -1 and +1 with +1 for a pair of perfectly in-phase signals, -1 for perfectly out-of-phase signals, and 0 for two signals with random phase difference.

5.5.9 Computational model

We simulated a two-dimensional model network of 800 excitatory and 200 inhibitory LIF neurons. All neurons are distributed randomly on the surface of a unit sphere (in order to have periodic boundary condition). Excitatory-to-excitatory projections were made between nearby neurons with a probability that has 0.1 maximum and decay like a Gaussian with spatial separation of the neurons. All other connections were established randomly without any spatial constraint. Synaptic weights are drawn from a gamma distribution with a very long tail [58]. The dynamics of the membrane potential (V_i) of each neuron evolved according to

$$\tau_m \frac{dV_i(t)}{dt} = -g_L[V_i(t) - E_L] + I_{syn}(t) \tag{5.4}$$

where the membrane time constant τ_m = 100 ms (excitatory neurons), 50 ms (inhibitory), and the leak conductance g_L = 10 nS (excitatory), 5 (inhibitory). The leak reversal potential E_L for each neuron was a random value between -70 and -60 mV, drawn from a Gaussian distribution. The reversal potentials for the synaptic current $I_{syn}(t)$ were E_{GABA} = -68 mV, and E_{AMPA} = 50 mV. The spike threshold for each neuron was -40 mV. A neuron reset to -59 mV after spiking, and was refractory for 2 ms (excitatory) and 1 ms (inhibitory).

The synaptic current is given by $I_{syn}^{YX}(t) = g_{YX}.S_{YX}(t)(V(t) - E_{syn})$, where g_{YX} is the maximum conductance and gating variable, $S(t)$, following a presynaptic spike at time 0 is described by

$$S_{YX}(t) = \frac{\tau_m}{(\tau_{DYX} - \tau_{RYX})}[exp(-(t - \tau_{LX})/\tau_{DYX}) - exp(-(t - \tau_{LX})/\tau_{RYX})] \tag{5.5}$$

Where for each synapse type (between presynaptic neurons of type X and postsynaptic neurons of type Y) had three relevant time course parameters: delay (τ_{LX}, that is, the lag between presynaptic spike time and beginning of conductance waveform), rise time (τ_{RYX}), and decay time (τ_{DYX}). Values are listed in table 1. In response to a presynaptic

Table 5.1: Network parameters

	Delay(ms)	Rise(ms)	Decay(ms)	Max conduc.(nS)
E-to-E	1.5	0.2	1.0	1.0
E-to-I	1.5	0.2	1.0	30.0
I-to-E	1.5	1.5	6.0	6.0
I-to-I	1.5	1.5	6.0	30.0

spike, the weight (W_{YX}) of a synapse depressed and recovered according to

$$\frac{dW_{YX}(t)}{dt} = -\frac{W_{YX}(t)}{\tau_{depress}}\delta(t - t_X^{sp}) + \frac{W_{YX}^0 - W_{YX}(t)}{\tau_{recover}} \tag{5.6}$$

With depression time constant $\tau_{depress}$ = 30 ms and recovery time constant $\tau_{recover}$ = 1.5 s.

External Poissonian inputs are fed into the all excitatory. During "ongoing" activity, the external input rate to each neuron was 175 Hz. The stimulus was modeled as a sudden increase to 875 Hz at stimulus onset time. The gating variables for external inputs had the same parameters as for E-to-E connections, and maximum conductances were g_E = 4 nS. Each trial was 5.8 s in duration, with stimulus onset at 2.7 s, and the time step was 0.05 ms. The ongoing epoch was defined to be 2.2 s to 0.2 s before stimulus onset, the transient epoch 0 s to 0.4 s after stimulus onset, and the steady-state epoch 0.6 s to 2.6 s after stimulus onset. The additional half a second at the beginning and end of each trial ensured there were no wavelet filtering artifacts in the ongoing and steady-state epochs.

5.6 Supplementary Materials

5.6.1 Supplementary Information 1: windows of activity chosen for analysis

We motivated our choice of windows based on the results of a previous study of population activity performed on the same data set [225]. In this previous work, the absolute value of LFP signals was divided by its standard deviation and network activity were defined as the summation of these traces from responsive electrodes. All trials were overlaid, the 90th percentile envelope was calculated. The transient epoch was defined to be the full-width at half-max of this envelope and steady-state was defined to start at the end of the transient epoch. The transient epoch was calculated on a prep-by-prep basis, and across all nine preparations (total of 13 datasets), lasted 423 ± 202 ms ($mean \pm SD$).

Since noise correlation distributions depend on window size, therefore, for this study the three epochs should be of comparable duration. A 2 s ongoing window before stimulus onset, a transient epoch of around 400 ms, and a 2 s steady-state epoch were chosen. Due to the observed variability in the previous study, epochs were separated by 200 ms in such a way that the end of the ongoing epoch coinciding with stimulus onset. We test the robustness of our results by performing the analysis for three 1 s windows for all epochs with and without gaps (see fig.S5.2). The transient increase in correlated variability and phase concentration is independent of the window size and they actually reflect the internal dynamics of the cortex during visual processing.

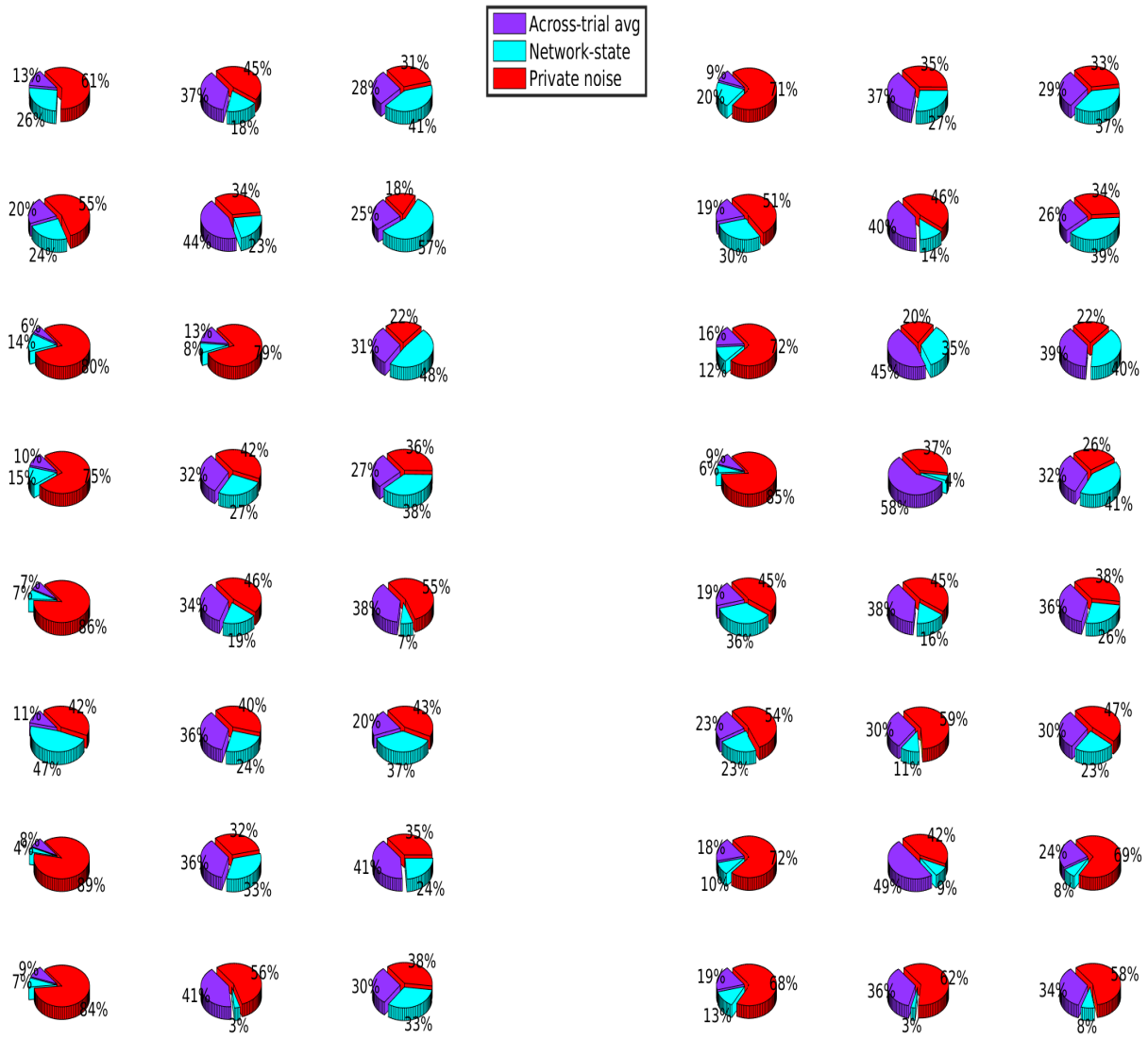

Figure S5.1: **Stimulus explains a higher fraction of response variability during transient epoch across 13 data sets out of 16 total.** Data sets are organized into two columns each with 8 rows. Each column has three sub-columns for representing three epochs; i.e. ongoing, transient, and steady-state. Overall, across-trial average captures larger portion of the variability during transient, while network state is a more important source of variability during steady-state.

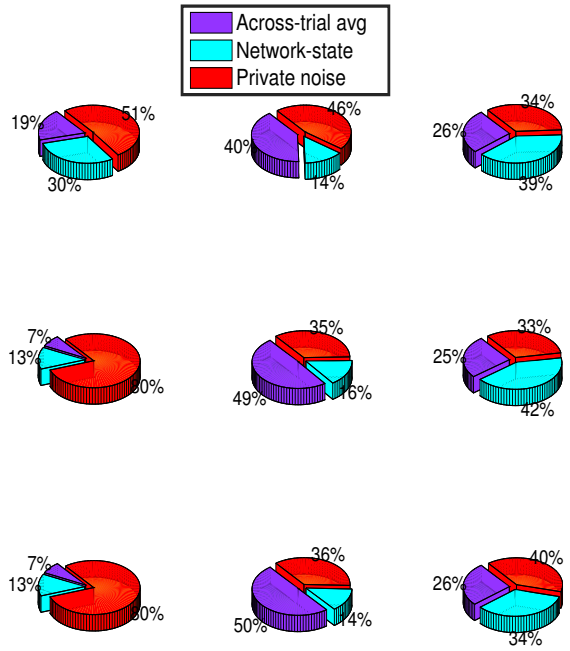

Figure S5.2: **Variability explained by different components is robust with the choice of gap and window size.** Top row is shown in fig.5.1f for the 2 s, 400 ms, and 2 s window sizes for ongoing, transient and steady-state with 200 ms gaps in between. Second row is pie charts for the windows with equal size (1 s) with 200 ms gaps in between. Third row is for equal 1 s windows without any gap in between. Across all the cases transient owe a large fraction of its variability to across-trial average and network-state plays a significant role during the steady-state. Overall results are robust to the choice of window size and gap.

5.6.2 Supplementary Information 2: frequency bands chosen for analysis

We separated the full (0.7 – 100 Hz) range into low-frequency (0.7 – 20 Hz) and high-frequency (20 – 100 Hz) bands because of two primary motivations. First, a common point of view in neuroscience community is that different frequency bands accomplish different tasks in the brain [11, 31, 125, 230]. This suggests that it is more reasonable to analyze low- and high-frequency bands separately. Second, it has been hypothesized that

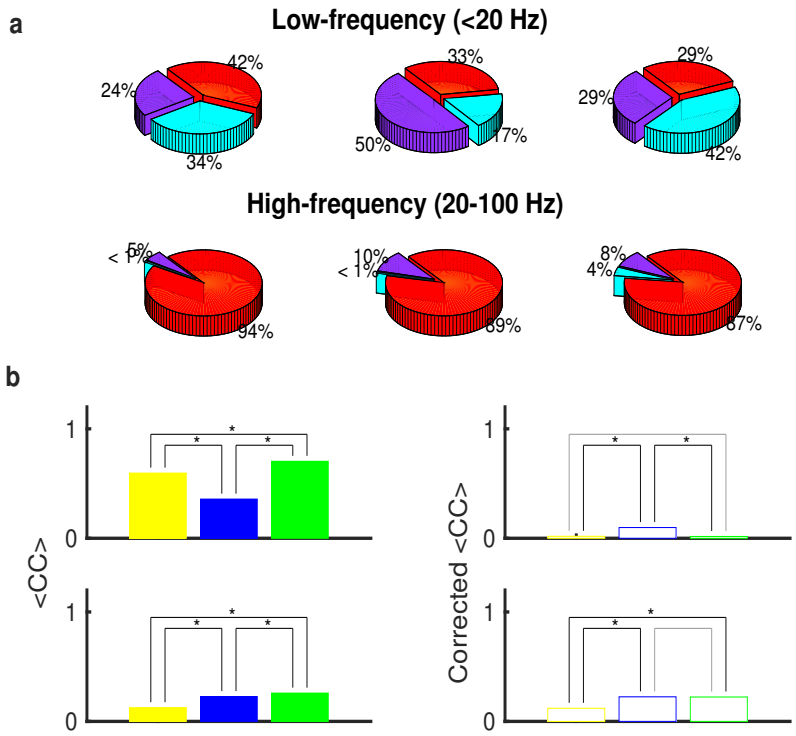

Figure S5.3: **Splitting frequency range into two separate low- and high-frequency bands.** (a) Variability explained by each component during epochs for two different frequency bands. Results presented in the main text is still valid for the low-frequency band but not for the high-frequency band. (b) $\langle CC \rangle$ in low (top) and high-frequency (bottom) bands before (left) and after (right) accounting for the network-state. Low-frequency $\langle CC \rangle$ changes dramatically by correcting for the network-state while high-frequency $\langle CC \rangle$ is insensitive to that.

correlated variability of V-LFPs in primate visual cortex in low-frequency band is stimulus dependent while high-frequency component is independent of the stimulus presentation [201]. However, we found that low-frequency results closely resemble results presented in fig.5.1 and fig.5.2, and $\langle CC \rangle$ amplitudes dramatically reduced by the impact of network-state. Moreover, high-frequency $\langle CC \rangle$ values do not decrease significantly with accounting for the network-state.

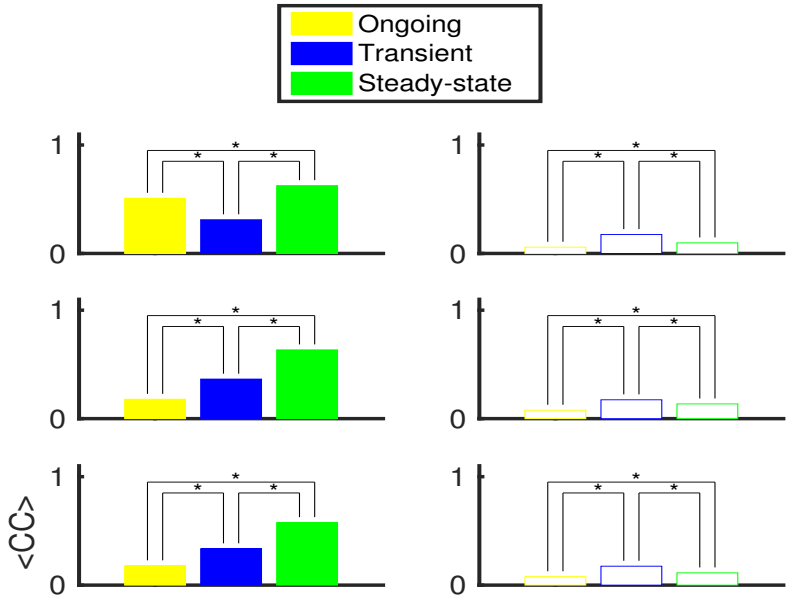

Figure S5.4: **Noise correlation dynamics is robust with respect to the choice of window size and gap.** Top row is shown in fig.5.2a, before (left) and after (right) correcting for the network-state, for 2 s, 400 ms, and 2 s window sizes for ongoing, transient and steady-state with 200 ms gaps in between. Second row is for the windows with equal size (1 s) with 200 ms gaps in between. Third row is for equal 1 s windows without any gap in between. Dramatic decrease in ongoing $\langle CC \rangle$ before correcting for the network-state with the choice of window size and gap (row one and two; left column) is because burst of activity is excluded and, meanwhile, an indication that network-state correction is necessary.

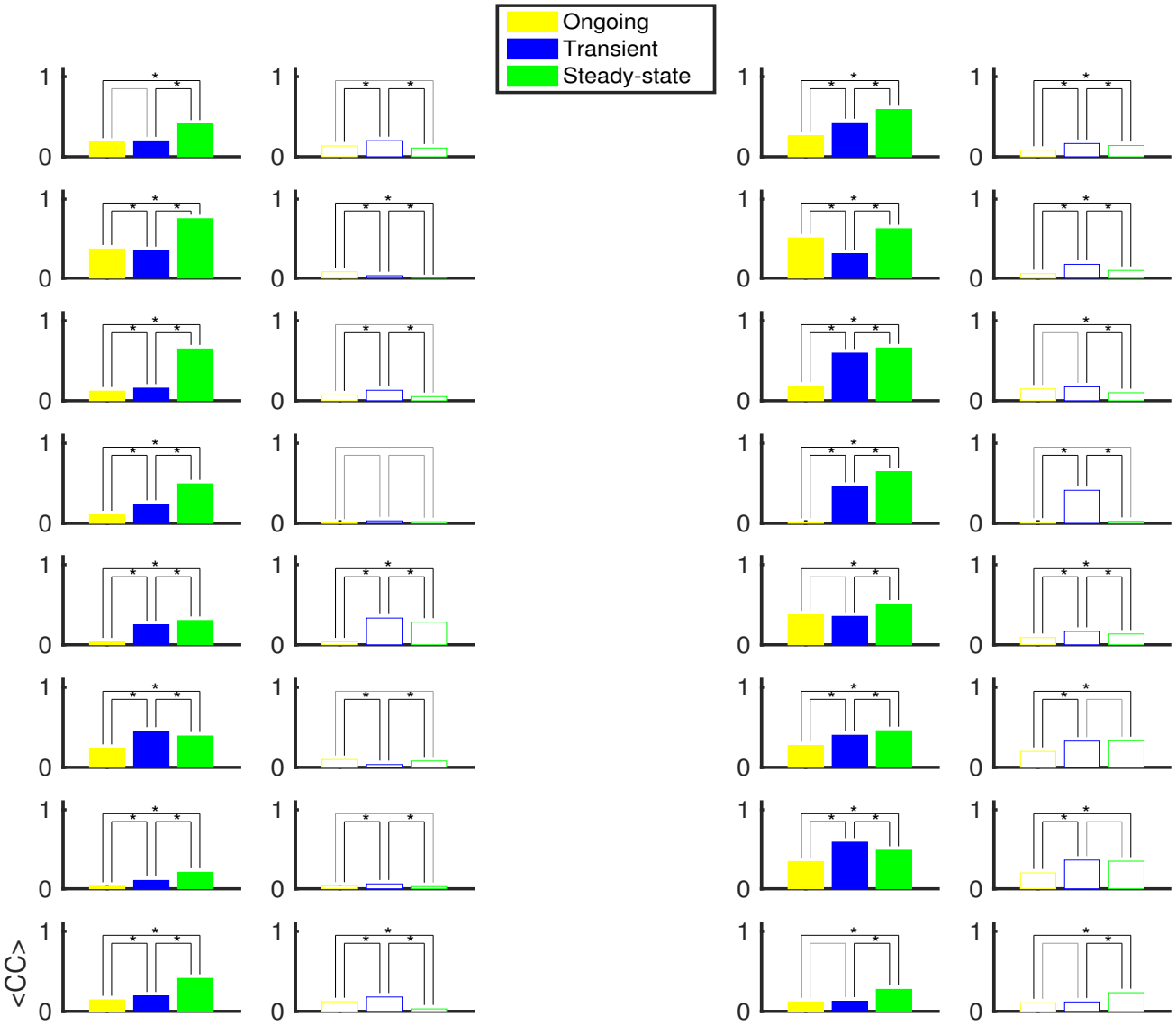

Figure S5.5: **Accounting for the global fluctuations highlight the transient increase in noise correlation.** All 16 data sets are arranged in two columns with 8 rows. On the left of each column (filled bars) $\langle CC \rangle$ is shown before network-state correction and on the right (empty bars) for after accounting for the network-state. Before correction only 2 data sets show transient increase, while after correction 12 data sets show the transient increase.

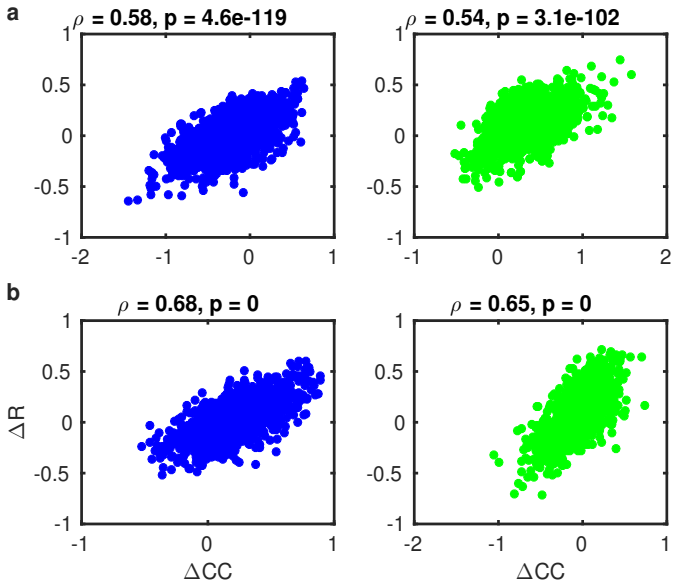

Figure S5.6: **Changes in correlated variability were significantly related to changes in phase concentration in both experiment and simulated network.** (a) Change in noise correlation versus phase concentration from ongoing to transient (left) and transient to steady-state (right) with their Spearman's ρ and its p-value. (b) The format is the same as in (a) for simulated data.

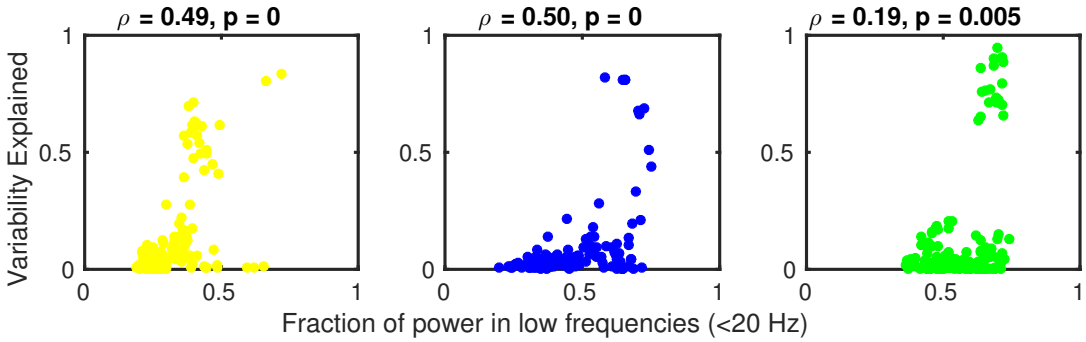

Figure S5.7: **Variability explained by the shared fluctuations is correlated with the fraction of power at low frequencies.** Variability explained versus fraction of power at low frequencies for ongoing (left), transient (middle), and steady-state (right) shows a significant correlation.

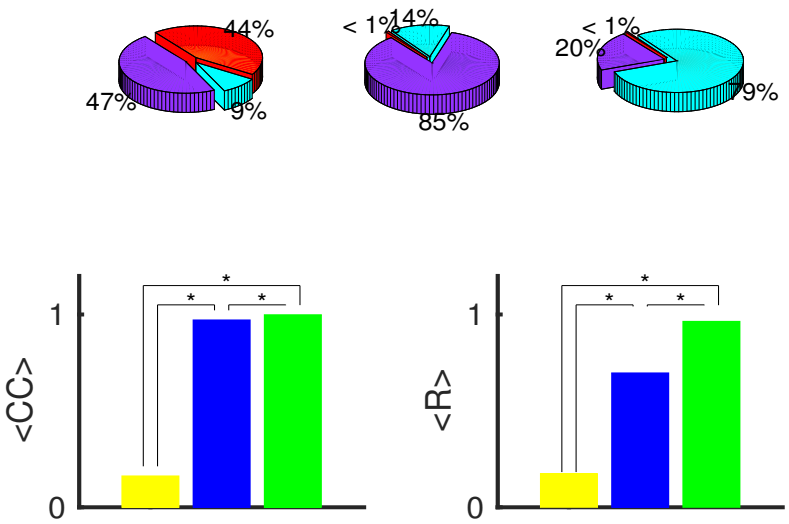

Figure S5.8: **A homogenous random network reproduce response variability results but not $\langle CC \rangle$ or $\langle R \rangle$.** Variability explained by each component during the three epochs is show at the top. Note the absolute domination of different components across epochs. $\langle CC \rangle$ (bottom left) and $\langle R \rangle$ (bottom right) indicate vary large amplitudes during transient and steady-state epochs. The only difference between this model and the model presented in fig.5.3 is that E-to-E connections are completely rewired here to obtain a homogenous random architecture.

Chapter 6

Open questions and additional topics

6.1 Introduction

I believe a scientific research is a collection of small items coming together and neatly fitting like the pieces of a puzzle. This line of research typically starts with a big question and achieved knowledge is squeezed in the frame of the question. However, sometimes researchers come across pieces that they don't know where they belong to. Those unknowns, though hinder our understanding progress, may help us identify new phenomena and might spike new discoveries. Like any other graduate student, I've struggled to identify and pursue some of these leads but at the time of writing this draft, I still am clueless where they can take us. Therefore, I try to address some of those ideas in this chapter. Whats presented in this chapter is a collection of "cool stuff" that could be connected together and/or to our current knowledge to see what the underlying picture is.

6.2 Whcih LFP frequencies are more informative?

6.2.1 Motivation

Local field potential (LFP) origin is a long-standing debate [265]. LFPs are thought to reflect population synaptic potentials [266,267], and other types of slow activity unrelated to synaptic events, such as spike afterpotential [268,269], and voltage-dependent membrane oscillations [270]. LFPs consist of a range of frequencies that may originate from distinct neural processes [271, 272] and can be related to various cognitive processes [273, 274]. However, our knowledge about which frequency components of LFP are most important for encoding sensory stimuli is very limited [98,265,271,275]. To address this question, we measure the amount of information conveyed by changes in power of LFPs at different frequencies [275], and then determine which frequencies carry independent (redundant) information and may originate from distinct (similar) neural processes.

6.2.2 Methods

Signals recorded from primary visual cortex of turtle eye-attached whole brain *ex-vivo* preparations are preprocessed (filtered and denoised). Three 1 s windows are identified (see chapter 4 for more information) as ongoing (before stimulus onset), transient (immediately after stimulus onset), and steady-state (seconds after stimulus onset). Now each epoch is divided to 4 non-overlapping windows of length 250 ms. The neural signals in each window is considered to be elicited by what has shown on the screen up to that time and, therefore, each window is considered the response to a different "stimulus" [275].

Then we use *Chronux* toolbox in MatLab to assess the power spectrum r_f at each frequency f, independently for each trial and responsive channel. The power spectrum is obtained using multi-taper method [276] with default settings.

Now the amount of information conveyed by the change in power of neural signals at different frequencies, r_f, can be calculated using Shannon mutual information (MI)

$$I(S;R_f) = \Sigma_s P(s) \Sigma_{r_f} P(r_f|s) log_2(\frac{P(r_f|s)}{P(r_f)}) \tag{6.1}$$

in which $P(s)$ is the probability of showing stimulus s and is equal to the inverse of number of stimuli (4 in our case), $P(r_f|s)$ is the probability of observing power r at frequency f for a given stimulus s, and $P(r_f) = \Sigma_s P(r_f|s)$. $I(S;R_f)$ is the amount of information in bits gained about stimulus from observing response in a single-trial of one channel.

6.2.3 Results

Mutual information is computed separately for each epoch across different frequencies (fig.6.1). Here's a series of remarks obtained from fig.6.1. First, most of the preparations show a decay of MI with frequency. it indicates that low frequencies convey more information than gamma-band frequencies. Second, since during ongoing epoch no stimulus is shown, MI should be zero. Actually we obtained very small MI for most of the preparations 19/24. I expect that correcting MI for biases will lead to insignificant MI for all the preparations. Third, transient epoch explains stimulus much better than steady-state for 17 preparations out of 24. This conclusion is consistent with what presented in chapter 5, where we should that stimulus captures a larger portion of signal variability during transient epoch. Fourth, there is a large variability across preparations unlike monkey

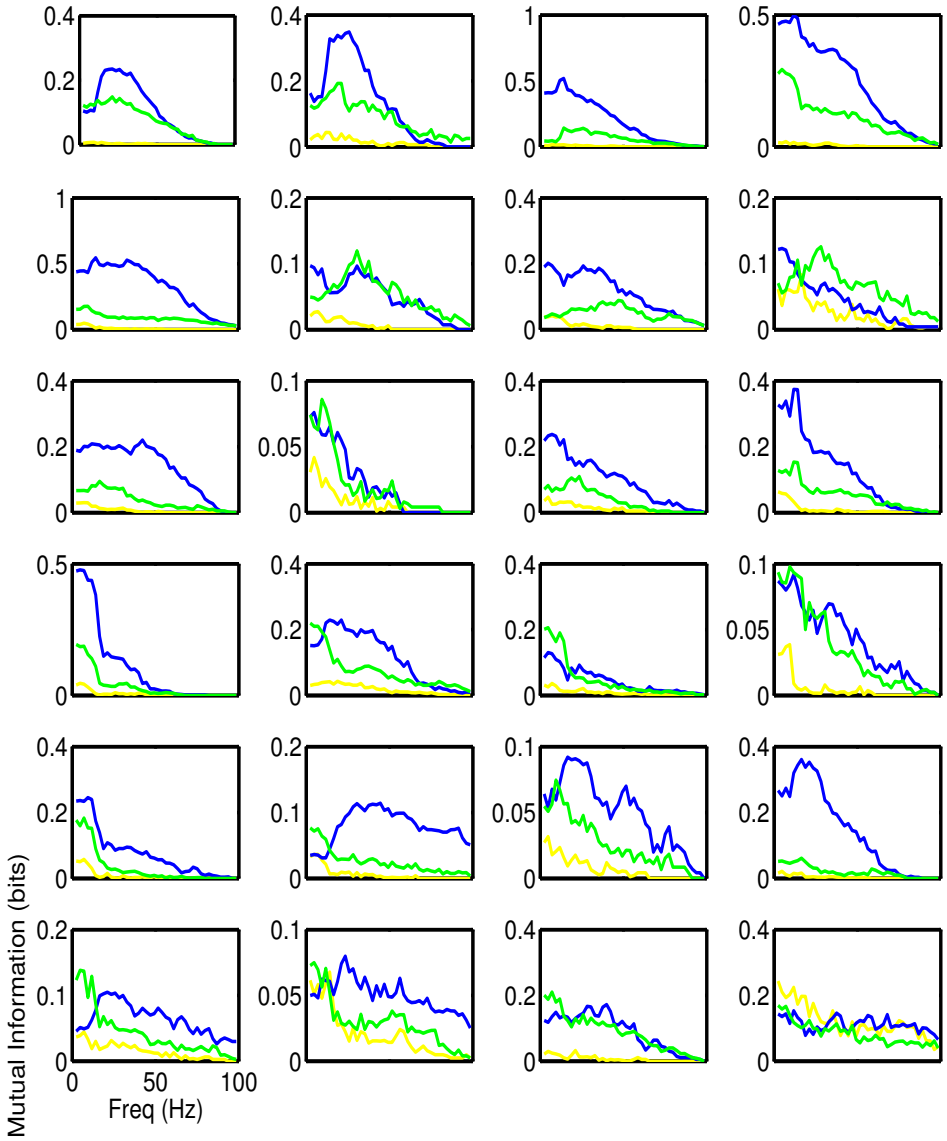

Figure 6.1: **Transient epoch carries more information across all frequencies especially $>$ 30 Hz.** Shown are MI across three epochs (yellow: ongoing, blue: transient, and green: steady-state) from 24 preparations. MI for most of the cases, 19/24, are larger during transient epochs than steady-state across whole frequency range. There is a large variability across preparations. Two preparations show a large peak at low frequencies with a very steep decay, four of them show a clear peak at around $\sim$ 30 Hz with a gentle decrease as frequency increases, and for the reset of the cases MI shows a gentle decrease in the whole frequency range.

data [275]. Two preparations show a large peak at low frequencies with a very steep decay, four of them show a clear peak at around ~ 30 Hz with a gentle decrease as frequency increases, and for the reset of the cases MI shows a gentle decrease in the whole frequency range.

What remains to investigate is the potential relationship between this variable MI patterns and any measure of variability in neural activity, persumably coefficient of variation [275]. Another route to pursue is to compute the information content of signals (across-trial average trace) and/or noises (deviations from across-trial average) and compare them against (fig.6.1) to see if any pattern emerges. Significance of the MI can be obtained by shuffling trials and channels and it helps to determine the confidence level of our conclusions.

6.3 The joint information carried by two different LFP frequencies

6.3.1 Methods

We showed that single-frequency MI have a variable behavior. Now this arises several exciting questions. To what extent information content of different frequency bands are redundant? Do we gain less uncertainty when combining together the power r_{f_1} and r_{f_2} at two different frequencies? The MI analysis can simply extended using joint probability

of the powers r_{f_1} and r_{f_2} :

$$I(S; R_{f_1}, R_{f_2} = \Sigma_s P(s) \Sigma_{r_{f_1}, r_{f_2}} P(r_{f_1}, r_{f_2}|s) log_2(\frac{P(r_{f_1}, r_{f_2}|s)}{P(r_{f_1}, r_{f_2})}) \tag{6.2}$$

where $P(r_{f_1}, r_{f_2}|s)$ is the probability of observing powers r_{f_1} and r_{f_2} at frequencies f_1 and f_2 for a given stimulus s; and $P(r_{f_1}, r_{f_2}) = \Sigma_s P(r_{f_1}, r_{f_2}|s)$.

6.3.2 Results

We computed power spectrum of the signals across epochs, channels, trials, and non-overlapping time windows, then we quantified joint MI (fig.6.2) across epochs (columns) for 6 of the preparations (rows). Here's a list of conclusions we reach from fig.6.2. First, intuitively, joint MI shows a very small value during ongoing epoch. Second, joint MI shows negative values for various combination of frequencies. I suspect that this is due to bias in our procedure and can be corrected using different techniques [277]. Third, gamma-band frequencies, $\sim 30 - 100$ Hz have a high joint MI amplitude, which indicates that individual frequencies carry independent information. However, I think this happens due to higher information content of individual component and, therefore a correction with that element in mind seems necessary. Fourth, two frequency bands separated by $\sim 30 - 40$ Hz show a small joint MI (off-diagonal elements) which implies that the two frequency bands are strongly correlated. Fifth, most importantly near-diagonal elements show modular patterns which persist through all of our recordings. Bias correction might lead to similar module with an indication that frequencies within a module are generated through similar neural processes.

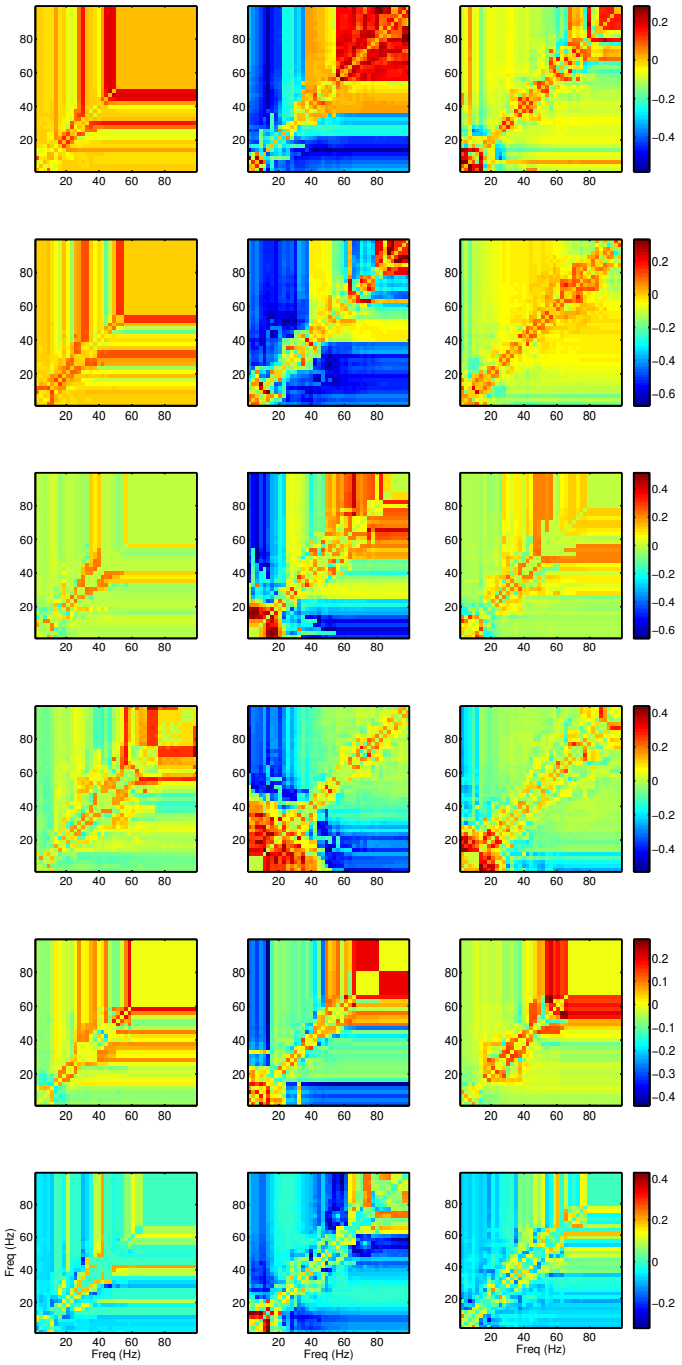

Figure 6.2: **Joint MI reveals underlying neural processes for different frequencies.** Joint MI across epochs (columns) for 6 of the preparations (rows). Ongoing epoch has a small joint MI in comparison to the other two epochs. Near-diagonal modules indicate that those frequencies may be generated through similar neural processes. Other structures reveal how correlated the frequency bands are.

6.4 Does critical state of avalanches explain coordination dynamics?

6.4.1 Introduction

Variability has been shown, both theoretically and experimentally, to be maximized while network is operating near critical state [278, 279]. Critical state is characterized by scale free probability distributions of neuronal avalanches under various preparations and conditions [280–282]. In chapters 4 and 5, we found that noise correlation, in both LFPs and $V_m s$, show a transient increase with stimulus onset. An unanswered question is whether this dynamics can be related to the state of the cortex at each epoch. In other words, does supercriticality indicate a higher coordination relative to critical or subcritical states? Do global coherent oscillations triggered at stimulus onset, which invade the whole network, cause a transient increase in noise correlation? What are the roles of synaptic adaptation in organizing the network into a critical state with more spatially confined oscillations?

6.4.2 Methods

To address this question we used the two-dimensional model network presented in chapter 5. Briefly, neurons are distributed randomly on the surface of a unit sphere with local excitatory-to-excitatory projections while all other connections are established randomly without any spatial constraint. Synaptic weights are drawn from a gamma distribution with a very long tail. The synaptic currents are given by an alpha function with their time

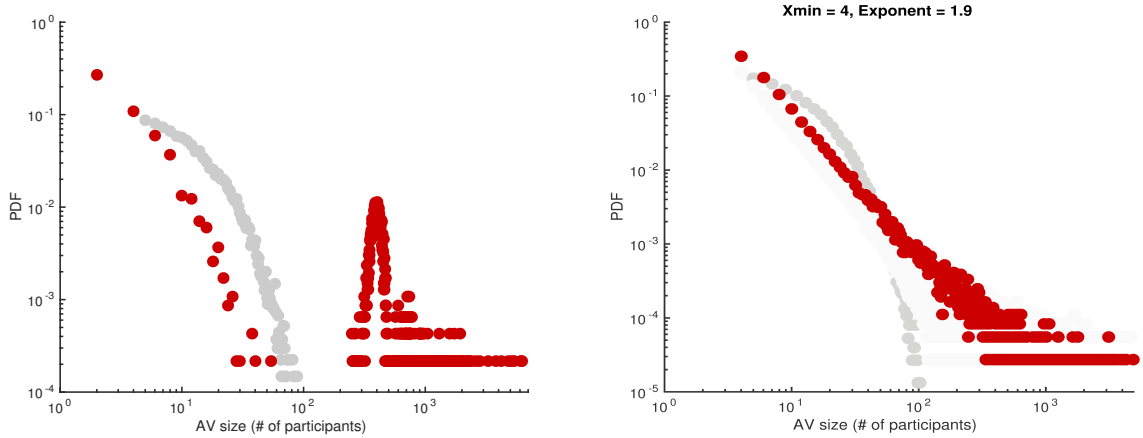

Figure 6.3: **Criticality state may explain coordination amplitude in the network.** Transient epoch shows a super-critical distribution of avalanche sizes while steady-state epoch demonestrates a powe-law distribution with $x_{min} = 4$ and $\alpha = 1.9$. White dots are generated with a hypothetical power-law distribution with given parameters. Gray distribution in both panels is for shuffled spike trains.

constants based on experimental studies. In response to a presynaptic spike, the weight of a synapse depresses and recoveres exponentially.

External Poissonian inputs are fed into the all excitatory. The stimulus was modeled as a sudden increase at stimulus onset time. The transient epoch was defined as a 1-s window immediately after stimulus onset, and the steady-state epoch as a 1-s window after transient epoch. Then, we quantified probability distribution of avalanche sizes and durations for each epoch separately to see if they demonestrate any power-law behaviour.

6.4.3 Results

We ran the clustered network for many trials (~ 200) and for each trial we quantified size of the avalanches started during transient and steady-state epochs, and then we plotted the distribution function of them (fig.6.3). Fig.6.3 left indicates that transient epoch frequently has very large avalanches, an indication of super-critical network. On the other

hand, fig.6.3 right demonestrate a power-law distribution during steady-state epoch, an critical network signature. Moreover, noise correlation shows a significantly larger value during transient epoch, therefore it is tempting to tie state of the network to coordination dynamics. However, more careful approaches show be taken to show that they don't just jointly emerge, but rather are correlated. Also, our model provides an opportunity to explore to what extent network parameters are relevant. For example, is the gamma distribution of synaptic weights necessary for the network to exhibit this behaviour? or how strength and size of the clusters impact our results?

Epilogue

In this thesis, we studied characteristic features of cortical oscillation in primary visual cortex of turtle eye-attached *ex vivo* preparations. We showed that intermittent oscillations arise from an interconnected ensemble of pyramidals and two types of inhibitory cells. Our investigations revealed that oscillations are the core mechanism in sculpting the coordination among a population of neurons, and moreover, a leaky integrate-and-fire network with clustered architecture is able to reproduce experimentally-observed dynamics with a biophysically plausible set of parameters. Last but not least, we showed that correcting for the global "noise" reduces the amplitude of correlations but doesn't affect its structure.

In chapter 2 we found that cortical oscillations occure by short episodes in time, and each episode has a different dominant frequency and lasts for a variable duration. We also showed that within each episode phase doesn't expand linearly with time. All of this implies that oscillations aren't reliable enough to be used as a "clock" signal and enable communication between remote brain regions. However, further investigation revealed that oscillations, though variable, are coherent among distant regions in the presence of even weak interconnection. Therefore, they are still imaginable to be used as a communication tool. Chapter 3 suggested that all the features, especially intermittency, is achievable in a network with two types of fast and slow inhibitory populations.

Spatio-temporal dynamics of coordination has gained widespread interest in neuroscience community as a framework for understanding the nature and underlying mechanisms of population coding in the brain. In chapter 4 we uncover the temporal coordination dynamics in membrane potential recordings. Stimulus onset induces a transient increase in noise correlation among cell's membrane potentials. More time into the stimulus, noise correlation declines to an intermediate value which is still significantly larger than ongoing epoch. Our modeling investigation revealed that two factors seem to a play an essential role in this dynamics; synaptic adaptation and network structure. Synaptic adaptation reduces the level of activity in the network and clustered architecture prevent network from having global oscillations. Oscillations are confined to spatially restricted clusters and, therefore, noise correlation amplitude decreases.

Finally, in chapter 5 we studied sources of trial-to-trial variability in neural responses. We found that across-trial average captures a large fraction of the variability in early part of the responses while across-electrode average is a better estimator of both ongoing activity and late part of the responses. In addition, recordings show a strong noise correlation that transiently increases with the stimulus onset. More importantly, we found that LFPs have a strong, shared fluctuation that accounting for them markedly reduces the amplitude of noise correlation. Our model investigations indicated that intracortical adaptation self-organizes cortical circuits towards a balanced regime at which network dynamically subdivides into clusters that leads to experimentally-observed variability and an intermediate coordination level.

Overall, while offering a profound insight on the interaction of oscillations and coordination in neural networks, we believe that this line of scientific inquiry is capable of

inducing a promising approache in studying both oscillations and temporal coordinatio. Hopefully, future investigations will help us better understand information coding schemes in the brain.

References

[1] G. G. Yener and E. Baar, "Brain oscillations as biomarkers in neuropsychiatric disorders," in *Dialogues in Clinical Neuroscience*, vol. 15, pp. 343–363, 2013.

[2] P. Fries, "A mechanism for cognitive dynamics: neuronal communication through neuronal coherence," *Trends in Cognitive Sciences*, vol. 9, pp. 474–480, oct 2005.

[3] P. Fries, D. Nikolić, and W. Singer, "The gamma cycle.," *Trends in Neurosciences*, vol. 30, pp. 309–16, jul 2007.

[4] C. M. Gray, A. K. Engel, P. König, and W. Singer, "Synchronization of oscillatory neuronal responses in cat striate cortex: temporal properties," *Visual Neuroscience*, vol. 8, no. 04, pp. 337–347, 1992.

[5] A. Destexhe, D. Contreras, and M. Steriade, "Spatiotemporal analysis of local field potentials and unit discharges in cat cerebral cortex during natural wake and sleep states.," *Journal of Neuroscience*, vol. 19, pp. 4595–608, jun 1999.

[6] A. Destexhe and T. Sejnowski, "Interactions between membrane conductances underlying thalamocortical slow-wave oscillations," *Physiological reviews*, vol. 83, no. 4, pp. 1401–1453, 2003.

[7] M. Steriade, D. A. McCormick, and T. J. Sejnowski, "Thalamocortical oscillations in the sleeping and aroused brain," *SCIENCE-NEW YORK THEN WASHINGTON-*, vol. 262, pp. 679–679, 1993.

[8] W. R. Softky and C. Koch, "The highly irregular firing of cortical cells is inconsistent with temporal integration of random epsps.," *Journal of Neuroscience*, vol. 13, no. 1, pp. 334–350, 1993.

[9] M. N. Shadlen and W. T. Newsome, "Noise, neural codes and cortical organization," *Current opinion in Neurobiology*, vol. 4, no. 4, pp. 569–579, 1994.

[10] A. M. Bastos, J. Vezoli, and P. Fries, "Communication through coherence with interareal delays," apr 2015.

[11] X.-j. Wang, "Neurophysiological and computational principles of cortical rhythms in cognition.," *Physiological reviews*, vol. 90, pp. 1195–268, jul 2010.

[12] A. Destexhe, S. W. Hughes, M. Rudolph, and V. Crunelli, "Are corticothalamic up-states fragments of wakefulness?," *Trends in Neurosciences*, vol. 30, no. 7, pp. 334–342, 2007.

[13] J. Born, B. Rasch, and S. Gais, "Sleep to remember," *The Neuroscientist*, vol. 12, no. 5, pp. 410–424, 2006.

[14] R. Stickgold and M. P. Walker, "Sleep-dependent memory consolidation and reconsolidation," *Sleep medicine*, vol. 8, no. 4, pp. 331–343, 2007.

[15] D. Contreras, I. Timofeev, and M. Steriade, "Mechanisms of long-lasting hyperpolarizations underlying slow sleep oscillations in cat corticothalamic networks.," *The Journal of Physiology*, vol. 494, no. Pt 1, p. 251, 1996.

[16] O. Jensen and C. D. Tesche, "Frontal theta activity in humans increases with memory load in a working memory task," *European journal of Neuroscience*, vol. 15, no. 8, pp. 1395–1399, 2002.

[17] J. A. Meltzer, H. P. Zaveri, I. I. Goncharova, M. M. Distasio, X. Papademetris, S. S. Spencer, D. D. Spencer, and R. T. Constable, "Effects of working memory load on oscillatory power in human intracranial eeg," *Cerebral Cortex*, vol. 18, no. 8, pp. 1843–1855, 2008.

[18] M. E. Hasselmo, "What is the function of hippocampal theta rhythm?linking behavioral data to phasic properties of field potential and unit recording data," *Hippocampus*, vol. 15, no. 7, pp. 936–949, 2005.

[19] H. Jasper and W. Penfield, "Electrocorticograms in man: Effect of voluntary movement upon the electrical activity of the precentral gyrus," *Archiv for Psychiatrie und Nervenkrankheiten*, vol. 183, no. 1-2, pp. 163–174, 1949.

[20] V. N. Murthy and E. E. Fetz, "Coherent 25-to 35-hz oscillations in the sensorimotor cortex of awake behaving monkeys.," *Proceedings of the National Academy of Sciences*, vol. 89, no. 12, pp. 5670–5674, 1992.

[21] T. J. Buschman and E. K. Miller, "Top-down versus bottom-up control of attention in the prefrontal and posterior parietal cortices," *science*, vol. 315, no. 5820, pp. 1860–1862, 2007.

[22] A. Bragin, G. Jandó, Z. Nádasdy, J. Hetke, K. Wise, and G. Buzsáki, "Gamma (40-100 hz) oscillation in the hippocampus of the behaving rat," *The Journal of Neuroscience*, vol. 15, no. 1, pp. 47–60, 1995.

[23] C. M. Gray and G. V. Di Prisco, "Stimulus-dependent neuronal oscillations and local synchronization in striate cortex of the alert cat," *The Journal of Neuroscience*, vol. 17, no. 9, pp. 3239–3253, 1997.

[24] P. E. Maldonado, S. Friedman-Hill, and C. M. Gray, "Dynamics of striate cortical activity in the alert macaque: Ii. fast time scale synchronization," *Cerebral Cortex*, vol. 10, no. 11, pp. 1117–1131, 2000.

[25] P. Fries, J. H. Reynolds, A. E. Rorie, and R. Desimone, "Modulation of oscillatory neuronal synchronization by selective visual attention," *Science*, vol. 291, no. 5508, pp. 1560–1563, 2001.

[26] P. Fries, "Neuronal gamma-band synchronization as a fundamental process in cortical computation," *Annual review of neuroscience*, vol. 32, pp. 209–224, 2009.

[27] J. J. Bouyer, M. F. Montaron, and A. Rougeul, "Fast fronto-parietal rhythms during combined focused attentive behaviour and immobility in cat: cortical and thalamic localizations.," *Electroencephalography and clinical neurophysiology*, vol. 51, pp. 244–52, mar 1981.

[28] W. Singer and C. M. Gray, "Visual feature integration and the temporal correlation hypothesis.," *Annual review of neuroscience*, vol. 18, pp. 555–86, jan 1995.

[29] C. M. Gray, "Synchronous oscillations in neuronal systems: mechanisms and functions," *Journal of Computational Neuroscience*, vol. 1, no. 1-2, pp. 11–38, 1994.

[30] E. Adrian, "Discharge frequencies in the cerebral and cerebellar cortex," in *Proc Phys Soc*, vol. 83, pp. 32–33, 1935.

[31] G. Buzsaki, K. Wise, *et al.*, "High-frequency network oscillation in the hippocampus," *Science*, vol. 256, no. 5059, p. 1025, 1992.

[32] R. T. Canolty, E. Edwards, S. S. Dalal, M. Soltani, S. S. Nagarajan, H. E. Kirsch, M. S. Berger, N. M. Barbaro, and R. T. Knight, "High gamma power is phase-locked to theta oscillations in human neocortex," *science*, vol. 313, no. 5793, pp. 1626–1628, 2006.

[33] K. Deisseroth, G. Feng, A. K. Majewska, G. Miesenböck, A. Ting, and M. J. Schnitzer, "Next-generation optical technologies for illuminating genetically targeted brain circuits," *The Journal of Neuroscience*, vol. 26, no. 41, pp. 10380–10386, 2006.

[34] L. Luo, E. M. Callaway, and K. Svoboda, "Genetic dissection of neural circuits," *Neuron*, vol. 57, no. 5, pp. 634–660, 2008.

[35] R. Traub and R. Miles, "Neuronal networks of the hippocampus. cambridge, uk," *Cambridge Univ. Press. Treue, S., & Martinez Trujillo, JC (1999). Feature-based attention influences motion processing Gain in macaque visual cortex. Nature*, vol. 399, p. 575579, 1991.

[36] X.-J. Wang and J. Rinzel, "Alternating and synchronous rhythms in reciprocally inhibitory model neurons," *Neural Computation*, vol. 4, pp. 84–97, jan 1992.

[37] X.-J. Wang and J. Rinzel, "Spindle rhythmicity in the reticularis thalami nucleus: Synchronization among mutually inhibitory neurons," *Neuroscience*, vol. 53, pp. 899–904, apr 1993.

[38] H. R. Wilson and J. D. Cowan, "Excitatory and inhibitory interactions in localized populations of model neurons," *Biophysical journal*, vol. 12, no. 1, p. 1, 1972.

[39] D. Hansel, G. Mato, and C. Meunier, "Synchrony in excitatory neural networks," *Neural Computation*, vol. 7, no. 2, pp. 307–337, 1995.

[40] E. Brown, J. Moehlis, and P. Holmes, "On the phase reduction and response dynamics of neural oscillator populations," *Neural Computation*, vol. 16, no. 4, pp. 673–715, 2004.

[41] B. Ermentrout, "Type i membranes, phase resetting curves, and synchrony," *Neural Computation*, vol. 8, no. 5, pp. 979–1001, 1996.

[42] X.-J. Wang and G. Buzsáki, "Gamma oscillation by synaptic inhibition in a hippocampal interneuronal network model," *The journal of Neuroscience*, vol. 16, no. 20, pp. 6402–6413, 1996.

[43] M. L. Bourdeau, F. Morin, C. E. Laurent, M. Azzi, and J.-C. Lacaille, "Kv4. 3-mediated a-type k+ currents underlie rhythmic activity in hippocampal interneurons," *The Journal of Neuroscience*, vol. 27, no. 8, pp. 1942–1953, 2007.

[44] Y. Gutfreund, I. Segev, *et al.*, "Subthreshold oscillations and resonant frequency in guinea-pig cortical neurons: physiology and modelling.," *The Journal of Physiology*, vol. 483, no. 3, pp. 621–640, 1995.

[45] D. Desmaisons, J.-D. Vincent, and P.-M. Lledo, "Control of action potential timing by intrinsic subthreshold oscillations in olfactory bulb output neurons," *The Journal of Neuroscience*, vol. 19, no. 24, pp. 10727–10737, 1999.

[46] W. A. Coetzee, Y. Amarillo, J. Chiu, A. Chow, D. Lau, T. McCormack, H. Morena, M. S. Nadal, A. Ozaita, D. Pountney, *et al.*, "Molecular diversity of k+ channels," *Annals of the New York Academy of Sciences*, vol. 868, no. 1, pp. 233–255, 1999.

[47] B. Hutcheon and Y. Yarom, "Resonance, oscillation and the intrinsic frequency preferences of neurons," *Trends in Neurosciences*, vol. 23, no. 5, pp. 216–222, 2000.

[48] I. Lampl and Y. Yarom, "Subthreshold oscillations and resonant behavior: two manifestations of the same mechanism," *Neuroscience*, vol. 78, no. 2, pp. 325–341, 1997.

[49] F. G. Pike, R. S. Goddard, J. M. Suckling, P. Ganter, N. Kasthuri, and O. Paulsen, "Distinct frequency preferences of different types of rat hippocampal neurones in response to oscillatory input currents," *The Journal of Physiology*, vol. 529, no. 1, pp. 205–213, 2000.

[50] G. B. Ermentrout and N. Kopell, "Multiple pulse interactions and averaging in systems of coupled neural oscillators," *Journal of Mathematical Biology*, vol. 29, no. 3, pp. 195–217, 1991.

[51] S. M. Crook, G. B. Ermentrout, and J. M. Bower, "Spike frequency adaptation affects the synchronization properties of networks of cortical oscillators," *Neural Computation*, vol. 10, no. 4, pp. 837–854, 1998.

[52] N. Brunel and X.-J. Wang, "What determines the frequency of fast network oscillations with irregular neural discharges? i. synaptic dynamics and excitation-inhibition balance.," *Journal of Neurophysiology*, vol. 90, pp. 415–30, jul 2003.

[53] R. D. Traub, R. Miles, and G. Buzsáki, "Computer simulation of carbachol-driven rhythmic population oscillations in the ca3 region of the in vitro rat hippocampus.," *The Journal of Physiology*, vol. 451, no. 1, pp. 653–672, 1992.

[54] R. D. Traub, M. A. Whittington, S. B. Colling, G. Buzsáki, and J. G. Jefferys, "Analysis of gamma rhythms in the rat hippocampus in vitro and in vivo.," *The Journal of Physiology*, vol. 493, pp. 471–484, jun 1996.

[55] M. A. Whittington, R. D. Traub, and J. G. Jefferys, "Synchronized oscillations in interneuron networks driven by metabotropic glutamate receptor activation.," *Nature*, vol. 373, pp. 612–5, feb 1995.

[56] P. Dayan and L. F. Abbott, *Theoretical neuroscience*, vol. 10. Cambridge, MA: MIT Press, 2001.

[57] F. K. Skinner, N. Kopell, and E. Marder, "Mechanisms for oscillation and frequency control in reciprocally inhibitory model neural networks," *Journal of Computational Neuroscience*, vol. 1, pp. 69–87, jun 1994.

[58] X.-J. Wang, "Synaptic basis of cortical persistent activity: the importance of nmda receptors to working memory.," *Journal of Neuroscience*, vol. 19, no. 21, pp. 9587–9603, 1999.

[59] D. Hansel and G. Mato, "Asynchronous states and the emergence of synchrony in large networks of interacting excitatory and inhibitory neurons," *Neural Computation*, vol. 15, no. 1, pp. 1–56, 2003.

[60] M. Wilson and J. M. Bower, "Cortical oscillations and temporal interactions in a computer simulation of piriform cortex," *Journal of Neurophysiology*, vol. 67, no. 4, pp. 981–995, 1992.

[61] P. Tiesinga and T. J. Sejnowski, "Cortical enlightenment: are attentional gamma oscillations driven by ing or ping?," *Neuron*, vol. 63, no. 6, pp. 727–732, 2009.

[62] D. Hansel and G. Mato, "Existence and stability of persistent states in large neuronal networks," *Physical Review Letters*, vol. 86, no. 18, p. 4175, 2001.

[63] R. C. Mureşan, O. F. Jurjuţ, V. V. Moca, W. Singer, and D. Nikolić, "The oscillation score: an efficient method for estimating oscillation strength in neuronal activity," *Journal of Neurophysiology*, vol. 99, no. 3, pp. 1333–1353, 2008.

[64] A. Compte, R. Reig, V. F. Descalzo, M. A. Harvey, G. D. Puccini, and M. V. Sanchez-Vives, "Spontaneous high-frequency (10–80 hz) oscillations during up states in the cerebral cortex in vitro," *The Journal of Neuroscience*, vol. 28, no. 51, pp. 13828–13844, 2008.

[65] J. Csicsvari, H. Hirase, A. Czurko, A. Mamiya, and G. Buzsáki, "Oscillatory coupling of hippocampal pyramidal cells and interneurons in the behaving rat," *J. Neurosci.*, vol. 19, pp. 274–287, jan 1999.

[66] J. Csicsvari, B. Jamieson, K. D. Wise, and G. Buzsáki, "Mechanisms of gamma oscillations in the hippocampus of the behaving rat.," *Neuron*, vol. 37, pp. 311–22, jan 2003.

[67] M. Jarvis and P. Mitra, "Sampling properties of the spectrum and coherency of sequences of action potentials," *Neural Computation*, vol. 13, no. 4, pp. 717–749, 2001.

[68] D. Xing, C.-I. Yeh, and R. M. Shapley, "Spatial spread of the local field potential and its laminar variation in visual cortex," *The Journal of Neuroscience*, vol. 29, no. 37, pp. 11540–11549, 2009.

[69] U. Mitzdorf *et al.*, *Current source-density method and application in cat cerebral cortex: investigation of evoked potentials and EEG phenomena*. American Physiological Society, 1985.

[70] A. Rauch, G. Rainer, and N. K. Logothetis, "The effect of a serotonin-induced dissociation between spiking and perisynaptic activity on bold functional mri," *Proceedings of the National Academy of Sciences*, vol. 105, no. 18, pp. 6759–6764, 2008.

[71] L. Avitan, M. Teicher, and M. Abeles, "Eeg generatora model of potentials in a volume conductor," *Journal of Neurophysiology*, vol. 102, no. 5, pp. 3046–3059, 2009.

[72] F. A. Khawaja, J. M. Tsui, and C. C. Pack, "Pattern motion selectivity of spiking outputs and local field potentials in macaque visual cortex," *The Journal of Neuroscience*, vol. 29, no. 43, pp. 13702–13709, 2009.

[73] M. J. Richardson, N. Brunel, and V. Hakim, "From subthreshold to firing-rate resonance," *Journal of Neurophysiology*, vol. 89, no. 5, pp. 2538–2554, 2003.

[74] N. Brunel and V. Hakim, "Fast global oscillations in networks of integrate-and-fire neurons with low firing rates.," *Neural Computation*, vol. 11, pp. 1621–1671, apr 1999.

[75] N. Brunel, "Dynamics of sparsely connected networks of excitatory and inhibitory spiking neurons.," *Journal of Computational Neuroscience*, vol. 8, no. 3, pp. 183–208, 2000.

[76] N. Fourcaud-Trocmé, D. Hansel, C. Van Vreeswijk, and N. Brunel, "How spike generation mechanisms determine the neuronal response to fluctuating inputs," *The Journal of Neuroscience*, vol. 23, no. 37, pp. 11628–11640, 2003.

[77] B. Doiron, B. Lindner, A. Longtin, L. Maler, and J. Bastian, "Oscillatory activity in electrosensory neurons increases with the spatial correlation of the stochastic input stimulus," *Physical Review Letters*, vol. 93, no. 4, p. 048101, 2004.

[78] B. Lindner, B. Doiron, and A. Longtin, "Theory of oscillatory firing induced by spatially correlated noise and delayed inhibitory feedback," *Physical Review E*, vol. 72, no. 6, p. 061919, 2005.

[79] C. Geisler, N. Brunel, and X.-J. Wang, "Contributions of intrinsic membrane dynamics to fast network oscillations with irregular neuronal discharges.," *Journal of Neurophysiology*, vol. 94, pp. 4344–61, dec 2005.

[80] E. K. Miller and T. J. Buschman, "Cortical circuits for the control of attention," *Current opinion in Neurobiology*, vol. 23, no. 2, pp. 216–222, 2013.

[81] D. Nikolić, P. Fries, and W. Singer, "Gamma oscillations: precise temporal coordination without a metronome," *Trends in Cognitive Sciences*, vol. 17, pp. 54–55, feb 2013.

[82] M. J. Roberts, E. Lowet, N. Brunet, M. TerWal, P. Tiesinga, P. Fries, and P. DeWeerd, "Robust gamma coherence between macaque v1 and v2 by dynamic frequency matching," *Neuron*, vol. 78, no. 3, pp. 523–536, 2013.

[83] E. Salinas and T. J. Sejnowski, "Correlated neuronal activity and the flow of neural information," *Nature Reviews Neuroscience*, vol. 2, no. 8, pp. 539–550, 2001.

[84] B. Doiron, A. Litwin-Kumar, R. Rosenbaum, G. K. Ocker, and K. Josić, "The mechanics of state-dependent neural correlations," *Nature Neuroscience*, vol. 19, pp. 383–393, feb 2016.

[85] A. Litwin-Kumar, A.-M. M. Oswald, N. N. Urban, and B. Doiron, "Balanced synaptic input shapes the correlation between neural spike trains," *PLoS Computational Biology*, vol. 7, p. e1002305, dec 2011.

[86] T. P. Vogels and L. Abbott, "Gating multiple signals through detailed balance of excitation and inhibition in spiking networks," *Nature Neuroscience*, vol. 12, no. 4, pp. 483–491, 2009.

[87] M. N. Franowicz and D. S. Barth, "Comparison of evoked potentials and high-frequency (gamma-band) oscillating potentials in rat auditory cortex," *J Neurophysiol*, vol. 74, pp. 96–112, jul 1995.

[88] E. Adrian, "The electrical activity of the mammalian olfactory bulb," *Electroencephalography and Clinical Neurophysiology*, vol. 2, pp. 377–388, jan 1950.

[89] S. Friedman-Hill, P. E. Maldonado, and C. M. Gray, "Dynamics of striate cortical activity in the alert macaque: I. incidence and stimulus-dependence of gamma-band neuronal oscillations," *Cerebral Cortex*, vol. 10, no. 11, pp. 1105–1116, 2000.

[90] M. Brosch, E. Budinger, and H. Scheich, "Stimulus-related gamma oscillations in primate auditory cortex," *Journal of Neurophysiology*, vol. 87, no. 6, pp. 2715–2725, 2002.

[91] R. Miles and J. C. Poncer, "Metabotropic glutamate receptors mediate a post-tetanic excitation of guinea-pig hippocampal inhibitory neurones.," *The Journal of physiology*, vol. 463, pp. 461–73, apr 1993.

[92] J. a. Cardin, M. Carlén, K. Meletis, U. Knoblich, F. Zhang, K. Deisseroth, L.-H. Tsai, and C. I. Moore, "Driving fast-spiking cells induces gamma rhythm and controls sensory responses.," *Nature*, vol. 459, pp. 663–7, jun 2009.

[93] C. M. Gray and W. Singer, "33stimulus-specific neuronal oscillations in orientation columns of cat visual cortex.," *Proceedings of the National Academy of Sciences of the United States of America*, vol. 86, no. 5, pp. 1698–1702, 1989.

[94] J. Lisman and M. Idiart, "Storage of 7 +/- 2 short-term memories in oscillatory subcycles," *Science*, vol. 267, pp. 1512–1515, mar 1995.

[95] G. Buzsáki and A. Draguhn, "Neuronal oscillations in cortical networks.," *Science*, vol. 304, pp. 1926–9, jun 2004.

[96] P. Lakatos, C. M. Chen, M. N. O'Connell, A. Mills, and C. E. Schroeder, "Neuronal oscillations and multisensory interaction in primary auditory cortex," *Neuron*, vol. 53, pp. 279–292, jan 2007.

[97] R. Eckhorn, R. Bauer, W. Jordan, M. Brosch, W. Kruse, M. H. Munk, and H. J. Reitboeck, "Coherent oscillations: A mechanism of feature linking in the visual cortex?," *Biological Cybernetics*, vol. 60, pp. 121–130, dec 1988.

[98] J. A. Henrie and R. Shapley, "Lfp power spectra in v1 cortex: the graded effect of stimulus contrast.," *Journal of Neurophysiology*, vol. 94, pp. 479–90, jul 2005.

[99] J.-M. Schoffelen, "Neuronal coherence as a mechanism of effective corticospinal interaction," *Science*, vol. 308, pp. 111–113, apr 2005.

[100] A. A. Ghazanfar, C. Chandrasekaran, and N. K. Logothetis, "Interactions between the superior temporal sulcus and auditory cortex mediate dynamic face/voice integration in rhesus monkeys.," *Journal of Neuroscience*, vol. 28, pp. 4457–69, apr 2008.

[101] B. Lima, W. Singer, N.-H. Chen, and S. Neuenschwander, "Synchronization dynamics in response to plaid stimuli in monkey v1.," *Cerebral cortex (New York, N.Y. : 1991)*, vol. 20, pp. 1556–73, jul 2010.

[102] M. A. Gieselmann and A. Thiele, "Comparison of spatial integration and surround suppression characteristics in spiking activity and the local field potential in macaque v1.," *The European journal of neuroscience*, vol. 28, pp. 447–59, aug 2008.

[103] X. Jia, S. Tanabe, and A. Kohn, "γ and the coordination of spiking activity in early visual cortex.," *Neuron*, vol. 77, pp. 762–74, feb 2013.

[104] P. H. Delano, E. Pavez, L. Robles, and P. E. Maldonado, "Stimulus-dependent oscillations and evoked potentials in chinchilla auditory cortex.," *Journal of comparative physiology. A, Neuroethology, sensory, neural, and behavioral physiology*, vol. 194, pp. 693–700, aug 2008.

[105] D. Xing, Y. Shen, S. P. Burns, C.-I. Yeh, R. Shapley, and W. Li, "Stochastic generation of gamma-band activity in primary visual cortex of awake and anesthetized monkeys," *Journal of Neuroscience*, vol. 32, pp. 13873–13880a, oct 2012.

[106] M. S. Ziolo and M. F. Bertelsen, "Effects of propofol administered via the supravertebral sinus in red-eared sliders.," *Journal of the American Veterinary Medical Association*, vol. 234, pp. 390–3, feb 2009.

[107] C. Torrence and G. P. Compo, "A practical guide to wavelet analysis," *Bulletin of the American Meteorological Society*, vol. 79, pp. 61–78, jan 1998.

[108] S. P. Burns, D. Xing, M. Shelley, and R. Shapley, "Searching for autocoherence in the cortical network with a time-frequency analysis of the local field potential," *Journal of Neuroscience*, vol. 30, pp. 4033–4047, mar 2010.

[109] M. S. Hoseini and R. Wessel, "Coherent and intermittent ensemble oscillations emerge from networks of irregular spiking neurons," *Journal of Neurophysiology*, p. jn.00578.2015, nov 2015.

[110] H. Yang, W. Shew, R. Roy, and D. Plenz, "Maximal variability of phase synchrony in cortical networks with neuronal avalanches," *Journal of Neuroscience*, vol. 32, pp. 1061–1072, jan 2012.

[111] S. P. Burns, D. Xing, and R. Shapley, "Is gamma-band activity in the local field potential of v1 cortex a 'clock' or filtered noise?," *Journal of Neuroscience*, vol. 31, pp. 9658–9664, jun 2011.

[112] S. M. Montgomery and G. Buzsáki, "Gamma oscillations dynamically couple hippocampal ca3 and ca1 regions during memory task performance.," *Proceedings of the National Academy of Sciences of the United States of America*, vol. 104, pp. 14495–500, sep 2007.

[113] S. M. Montgomery, A. Sirota, and G. Buzsáki, "Theta and gamma coordination of hippocampal networks during waking and rapid eye movement sleep.," *Journal of Neuroscience*, vol. 28, pp. 6731–41, jun 2008.

[114] P. Fries, P. R. Roelfsema, A. K. Engel, P. Konig, and W. Singer, "Synchronization of oscillatory responses in visual cortex correlates with perception in interocular rivalry," *Proceedings of the National Academy of Sciences*, vol. 94, pp. 12699–12704, nov 1997.

[115] A. K. Engel, P. Konig, C. M. Gray, and W. Singer, "Stimulus-dependent neuronal oscillations in cat visual cortex: Inter-columnar interaction as determined by cross-correlation analysis," *European Journal of Neuroscience*, vol. 2, pp. 588–606, jul 1990.

[116] X.-J. Wang, D. Golomb, and J. Rinzel, "Emergent spindle oscillations and intermittent burst firing in a thalamic model: specific neuronal mechanisms.," *Proceedings of the National Academy of Sciences of the United States of America*, vol. 92, pp. 5577–81, jun 1995.

[117] N. Kopell, B. Ermentrout, M. A. Whittington, and R. D. Traub, "Gamma rhythms and beta rhythms have different synchronization properties," *Proceedings of the National Academy of Sciences*, vol. 97, pp. 1867–1872, feb 2000.

[118] P. Tiesinga, J. M. Fellous, J. V. José, and T. J. Sejnowski, "Computational model of carbachol-induced delta, theta, and gamma oscillations in the hippocampus.," *Hippocampus*, vol. 11, pp. 251–74, jan 2001.

[119] R. R. Llinas, A. A. Grace, and Y. Yarom, "In vitro neurons in mammalian cortical layer 4 exhibit intrinsic oscillatory activity in the 10- to 50-hz frequency range.," *Proceedings of the National Academy of Sciences*, vol. 88, pp. 897–901, feb 1991.

[120] N. Hoogenboom, J.-M. Schoffelen, R. Oostenveld, L. M. Parkes, and P. Fries, "Localizing human visual gamma-band activity in frequency, time and space.," *NeuroImage*, vol. 29, pp. 764–73, feb 2006.

[121] B. V. Atallah and M. Scanziani, "Instantaneous modulation of gamma oscillation frequency by balancing excitation with inhibition.," *Neuron*, vol. 62, pp. 566–77, may 2009.

[122] S. D. Muthukumaraswamy, K. D. Singh, J. B. Swettenham, and D. K. Jones, "Visual gamma oscillations and evoked responses: variability, repeatability and structural mri correlates.," *NeuroImage*, vol. 49, pp. 3349–57, feb 2010.

[123] C. Buia and P. Tiesinga, "Attentional modulation of firing rate and synchrony in a model cortical network.," *Journal of Computational Neuroscience*, vol. 20, pp. 247–64, jun 2006.

[124] E. Baar, C. Baar-Eroglu, S. Karaka, and M. Schürmann, "Gamma, alpha, delta, and theta oscillations govern cognitive processes.," *International Journal of Psychophysiology*, vol. 39, pp. 241–8, jan 2001.

[125] L. M. Ward, "Synchronous neural oscillations and cognitive processes," *Trends in Cognitive Sciences*, vol. 7, pp. 553–559, dec 2003.

[126] C. S. Herrmann, M. H. Munk, and A. K. Engel, "Cognitive functions of gamma-band activity: memory match and utilization," *Trends in Cognitive Sciences*, vol. 8, pp. 347–355, aug 2004.

[127] G. Buzsáki and J. J. Chrobak, "Temporal structure in spatially organized neuronal ensembles: a role for interneuronal networks," *Current Opinion in Neurobiology*, vol. 5, pp. 504–510, aug 1995.

[128] C. D. Harvey, F. Collman, D. A. Dombeck, and D. W. Tank, "Intracellular dynamics of hippocampal place cells during virtual navigation.," *Nature*, vol. 461, pp. 941–6, oct 2009.

[129] T. Womelsdorf, J.-M. Schoffelen, R. Oostenveld, W. Singer, R. Desimone, A. K. Engel, and P. Fries, "Modulation of neuronal interactions through neuronal synchronization," *Science*, vol. 316, pp. 1609–1612, jun 2007.

[130] C. A. Bosman, J.-M. Schoffelen, N. Brunet, R. Oostenveld, A. M. Bastos, T. Womelsdorf, B. Rubehn, T. Stieglitz, P. De Weerd, and P. Fries, "Attentional stimulus selection through selective synchronization between monkey visual areas.," *Neuron*, vol. 75, pp. 875–88, sep 2012.

[131] I. Grothe, S. D. Neitzel, S. Mandon, and A. K. Kreiter, "Switching neuronal inputs by differential modulations of gamma-band phase-coherence.," *Journal of Neuroscience*, vol. 32, pp. 16172–16180, nov 2012.

[132] K. Kang, M. Shelley, J. A. Henrie, and R. Shapley, "Lfp spectral peaks in v1 cortex: network resonance and cortico-cortical feedback," *Journal of Computational Neuroscience*, vol. 29, pp. 495–507, dec 2010.

[133] U. Rutishauser, A. Kotowicz, and G. Laurent, "A method for closed-loop presentation of sensory stimuli conditional on the internal brain-state of awake animals," *Journal of Neuroscience Methods*, vol. 215, pp. 139–155, apr 2013.

[134] G. Buzsáki and X.-J. Wang, "Mechanisms of gamma oscillations," *Annual Review of Neuroscience*, vol. 35, pp. 203–225, jul 2012.

[135] H. Lindén, T. Tetzlaff, T. C. Potjans, K. H. Pettersen, S. Grün, M. Diesmann, and G. T. Einevoll, "Modeling the spatial reach of the lfp.," *Neuron*, vol. 72, pp. 859–72, dec 2011.

[136] G. Buzsáki, N. Logothetis, and W. Singer, "Scaling brain size, keeping timing: evolutionary preservation of brain rhythms," *Neuron*, vol. 80, no. 3, pp. 751–764, 2013.

[137] O. Jensen, J. Kaiser, and J.-P. Lachaux, "Human gamma-frequency oscillations associated with attention and memory," *Trends in Neurosciences*, vol. 30, no. 7, pp. 317–324, 2007.

[138] J. C. Prechtl, "Visual motion induces synchronous oscillations in turtle visual cortex," *Proceedings of the National Academy of Sciences*, vol. 91, no. 26, pp. 12467–12471, 1994.

[139] S. R. Lehky, T. J. Sejnowski, and R. Desimone, "Selectivity and sparseness in the responses of striate complex cells.," *Vision Research*, vol. 45, pp. 57–73, jan 2005.

[140] E. T. Rolls, N. C. Aggelopoulos, L. Franco, and A. Treves, "Information encoding in the inferior temporal visual cortex: contributions of the firing rates and the correlations between the firing of neurons," *Biological Cybernetics*, vol. 90, no. 1, pp. 19–32, 2004.

[141] E. T. Rolls, L. Franco, N. C. Aggelopoulos, and J. M. Jerez, "Information in the first spike, the order of spikes, and the number of spikes provided by neurons in the inferior temporal visual cortex," *Vision Research*, vol. 46, no. 25, pp. 4193–4205, 2006.

[142] A. Treves, S. Panzeri, E. T. Rolls, M. Booth, and E. A. Wakeman, "Firing rate distributions and efficiency of information transmission of inferior temporal cortex neurons to natural visual stimuli," *Neural Computation*, vol. 11, no. 3, pp. 601–631, 1998.

[143] F. Barbieri, A. Mazzoni, N. K. Logothetis, S. Panzeri, and N. Brunel, "Stimulus dependence of local field potential spectra: experiment versus theory," *The Journal of Neuroscience*, vol. 34, no. 44, pp. 14589–14605, 2014.

[144] X. Jia, M. A. Smith, and A. Kohn, "Stimulus selectivity and spatial coherence of gamma components of the local field potential," *The Journal of Neuroscience*, vol. 31, no. 25, pp. 9390–9403, 2011.

[145] M. Bartos, I. Vida, and P. Jonas, "Synaptic mechanisms of synchronized gamma oscillations in inhibitory interneuron networks," *Nature Reviews Neuroscience*, vol. 8, no. 1, pp. 45–56, 2007.

[146] R. D. Traub and M. A. Whittington, *Cortical oscillations in health and disease*. Oxford University Press, USA, 2010.

[147] M. S. Caudill, S. F. Brandt, Z. Nussinov, and R. Wessel, "Intricate phase diagram of a prevalent visual circuit reveals universal dynamics, phase transitions, and resonances," *Physical Review E*, vol. 80, no. 5, p. 051923, 2009.

[148] M. I. Banks, J. a. White, and R. a. Pearce, "Interactions between distinct gaba(a) circuits in hippocampus.," *Neuron*, vol. 25, pp. 449–57, feb 2000.

[149] J. H. Goldberg and R. Yuste, "Space matters: Local and global dendritic ca2+ compartmentalization in cortical interneurons," *Trends in Neurosciences*, vol. 28, pp. 158–167, mar 2005.

[150] G. Silberberg and H. Markram, "Disynaptic inhibition between neocortical pyramidal cells mediated by martinotti cells.," *Neuron*, vol. 53, pp. 735–46, mar 2007.

[151] M. Beierlein, J. R. Gibson, and B. W. Connors, "Two dynamically distinct inhibitory networks in layer 4 of the neocortex," *Journal of Neurophysiology*, vol. 90, no. 5, pp. 2987–3000, 2003.

[152] C. Kapfer, L. L. Glickfeld, B. V. Atallah, and M. Scanziani, "Supralinear increase of recurrent inhibition during sparse activity in the somatosensory cortex.," *Nature Neuroscience*, vol. 10, pp. 743–53, jun 2007.

[153] M. C. Angulo, J. Rossier, and E. Audinat, "Postsynaptic glutamate receptors and integrative properties of fast-spiking interneurons in the rat neocortex," *Journal of Neurophysiology*, vol. 82, no. 3, pp. 1295–1302, 1999.

[154] M. Bartos, I. Vida, M. Frotscher, J. R. Geiger, and P. Jonas, "Rapid signaling at inhibitory synapses in a dentate gyrus interneuron network," *The Journal of Neuroscience*, vol. 21, no. 8, pp. 2687–2698, 2001.

[155] A. Gupta, Y. Wang, and H. Markram, "Organizing principles for a diversity of gabaergic interneurons and synapses in the neocortex," *Science*, vol. 287, no. 5451, pp. 273–278, 2000.

[156] Z. Xiang, J. R. Huguenard, and D. A. Prince, "Gabaa receptor-mediated currents in interneurons and pyramidal cells of rat visual cortex," *The Journal of Physiology*, vol. 506, no. 3, pp. 715–730, 1998.

[157] F.-M. Zhou and J. J. Hablitz, "Ampa receptor-mediated epscs in rat neocortical layer ii/iii interneurons have rapid kinetics," *Brain Research*, vol. 780, no. 1, pp. 166–169, 1998.

[158] E. Buhl, G. Tamas, T. Szilagyi, C. Stricker, O. Paulsen, and P. Somogyi, "Effect, number and location of synapses made by single pyramidal cells onto aspiny interneurones of cat visual cortex.," *The Journal of Physiology*, vol. 500, no. Pt 3, p. 689, 1997.

[159] H. Markram, J. Lübke, M. Frotscher, A. Roth, and B. Sakmann, "Physiology and anatomy of synaptic connections between thick tufted pyramidal neurones in the developing rat neocortex.," *The Journal of physiology*, vol. 500, no. Pt 2, p. 409, 1997.

[160] I. Ginzburg and H. Sompolinsky, "Theory of correlations in stochastic neural networks," *Physical review E*, vol. 50, no. 4, p. 3171, 1994.

[161] D. Hansel and H. Sompolinsky, "Synchronization and computation in a chaotic neural network," *Physical Review Letters*, vol. 68, no. 5, p. 718, 1992.

[162] D. Golomb, A. Shedmi, R. Curtu, and G. B. Ermentrout, "Persistent synchronized bursting activity in cortical tissues with low magnesium concentration: a modeling study," *Journal of Neurophysiology*, vol. 95, no. 2, pp. 1049–1067, 2006.

[163] P. P. Mitra and B. Pesaran, "Analysis of dynamic brain imaging data.," *Biophysical journal*, vol. 76, pp. 691–708, feb 1999.

[164] S. Mallat, "A wavelet tour of signal processing 2nd edn (new york: Academic)," 1999.

[165] K. V. Mardia, "Statistics of directional data," *Journal of the Royal Statistical Society. Series B (Methodological)*, pp. 349–393, 1975.

[166] C. Börgers and N. Kopell, "Effects of noisy drive on rhythms in networks of excitatory and inhibitory neurons," *Neural Computation*, vol. 17, pp. 557–608, mar 2005.

[167] E. O. Mann and O. Paulsen, "Role of gabaergic inhibition in hippocampal network oscillations," *Trends in Neurosciences*, vol. 30, no. 7, pp. 343–349, 2007.

[168] Z. P. Kilpatrick and B. Ermentrout, "Sparse gamma rhythms arising through clustering in adapting neuronal networks.," *PLoS computational biology*, vol. 7, p. e1002281, nov 2011.

[169] K. Kotani, I. Yamaguchi, L. Yoshida, Y. Jimbo, and B. Ermentrout, "Population dynamics of the modified theta model: macroscopic phase reduction and bifurcation analysis link microscopic neuronal interactions to macroscopic gamma oscillation," *Journal of The Royal Society Interface*, vol. 11, pp. 20140058–20140058, mar 2014.

[170] M. Krupa, S. Gielen, and B. Gutkin, "Adaptation and shunting inhibition leads to pyramidal/interneuron gamma with sparse firing of pyramidal cells," *Journal of Computational Neuroscience*, vol. 37, pp. 357–376, oct 2014.

[171] L. L. McMahon, J. H. Williams, and J. A. Kauer, "Functionally distinct groups of interneurons identified during rhythmic carbachol oscillations in hippocampus in vitro," *The Journal of Neuroscience*, vol. 18, no. 15, pp. 5640–5651, 1998.

[172] R. D. Traub, A. Bibbig, F. E. LeBeau, E. H. Buhl, and M. A. Whittington, "Cellular mechanisms of neuronal population oscillations in the hippocampus in vitro," *Annu. Rev. Neurosci.*, vol. 27, pp. 247–278, 2004.

[173] D. Vierling-Claassen, J. A. Cardin, C. I. Moore, and S. R. Jones, "Computational modeling of distinct neocortical oscillations driven by cell-type selective optogenetic drive: separable resonant circuits controlled by low-threshold spiking and fast-spiking interneurons.," *Frontiers in human neuroscience*, vol. 4, p. 198, jan 2010.

[174] R.-M. Memmesheimer, "Quantitative prediction of intermittent high-frequency oscillations in neural networks with supralinear dendritic interactions," *Proceedings of the National Academy of Sciences*, vol. 107, pp. 11092–11097, jun 2010.

[175] S. Gasparini, "State-dependent dendritic computation in hippocampal ca1 pyramidal neurons," *Journal of Neuroscience*, vol. 26, pp. 2088–2100, feb 2006.

[176] T. Nevian, M. E. Larkum, A. Polsky, and J. Schiller, "Properties of basal dendrites of layer 5 pyramidal neurons: a direct patch-clamp recording study," *Nature Neuroscience*, vol. 10, no. 2, pp. 206–214, 2007.

[177] A. a. Prinz, D. Bucher, and E. Marder, "Similar network activity from disparate circuit parameters.," *Nature Neuroscience*, vol. 7, no. 12, pp. 1345–1352, 2004.

[178] B. Bathellier, A. Carleton, and W. Gerstner, "Gamma oscillations in a nonlinear regime: a minimal model approach using heterogeneous integrate-and-fire networks.," *Neural Computation*, vol. 20, pp. 2973–3002, dec 2008.

[179] W. Gerstner and J. L. van Hemmen, "Coherence and incoherence in a globally coupled ensemble of pulse-emitting units," *Physical Review Letters*, vol. 71, no. 3, p. 312, 1993.

[180] C. Van Vreeswijk, L. F. Abbott, and B. Ermentrout, "When inhibition not excitation synchronizes neural firing.," *Journal of Computational Neuroscience*, vol. 1, pp. 313–21, dec 1994.

[181] E. M. Izhikevich, "Polychronization: computation with spikes.," *Neural Computation*, vol. 18, pp. 245–82, feb 2006.

[182] A. Litwin-Kumar and B. Doiron, "Slow dynamics and high variability in balanced cortical networks with clustered connections.," *Nature Neuroscience*, vol. 15, pp. 1498–505, nov 2012.

[183] M. Goodfellow, K. Schindler, and G. Baier, "Intermittent spike-wave dynamics in a heterogeneous, spatially extended neural mass model.," *NeuroImage*, vol. 55, pp. 920–32, apr 2011.

[184] X. Jia, D. Xing, and A. Kohn, "No consistent relationship between gamma power and peak frequency in macaque primary visual cortex," *Journal of Neuroscience*, vol. 33, pp. 17–25, jan 2013.

[185] F. L. Da Silva, A. Van Rotterdam, P. Barts, E. Van Heusden, and W. Burr, "Models of neuronal populations: the basic mechanisms of rhythmicity," *Progress in brain research*, vol. 45, pp. 281–308, 1976.

[186] F. Wendling, F. Bartolomei, J. Bellanger, and P. Chauvel, "Epileptic fast activity can be explained by a model of impaired gabaergic dendritic inhibition," *European Journal of Neuroscience*, vol. 15, no. 9, pp. 1499–1508, 2002.

[187] R. Miles, K. Toth, A. I. Gulyas, N. Hajos, and T. F. Freund, "Differences between somatic and dendritic inhibition in the hippocampus," *Neuron*, vol. 16, no. 4, pp. 815–823, 1996.

[188] S. Panzeri, N. Brunel, N. K. Logothetis, and C. Kayser, "Sensory neural codes using multiplexed temporal scales," *Trends in Neurosciences*, vol. 33, no. 3, pp. 111–120, 2010.

[189] I. E. Ohiorhenuan, F. Mechler, K. P. Purpura, A. M. Schmid, Q. Hu, and J. D. Victor, "Sparse coding and high-order correlations in fine-scale cortical networks," *Nature*, vol. 466, no. 7306, pp. 617–621, 2010.

[190] A. Renart, J. de la Rocha, P. Bartho, L. Hollender, N. Parga, A. Reyes, and K. D. Harris, "The asynchronous state in cortical circuits," *Science*, vol. 327, pp. 587–590, jan 2010.

[191] M. L. Scholvinck, a. B. Saleem, A. Benucci, K. D. Harris, and M. Carandini, "Cortical state determines global variability and correlations in visual cortex," *Journal of Neuroscience*, vol. 35, pp. 170–178, jan 2015.

[192] M. Okun, N. a. Steinmetz, L. Cossell, M. F. Iacaruso, H. Ko, Barth, T. Moore, S. B. Hofer, T. D. Mrsic-Flogel, M. Carandini, and K. D. Harris, "Diverse coupling of neurons to populations in sensory cortex," *Nature*, vol. 521, pp. 511–515, apr 2015.

[193] J. F. Poulet and C. C. Petersen, "Internal brain state regulates membrane potential synchrony in barrel cortex of behaving mice," *Nature*, vol. 454, no. 7206, pp. 881–885, 2008.

[194] B. Haider, D. P. Schulz, M. Häusser, and M. Carandini, "Millisecond coupling of local field potentials to synaptic currents in the awake visual cortex," *Neuron*, vol. 90, pp. 35–42, apr 2016.

[195] E. Zohary, M. N. Shadlen, and W. T. Newsome, "Correlated neuronal discharge rate and its implications for psychophysical performance.," jul 1994.

[196] R. Moreno-Bote, J. Beck, I. Kanitscheider, X. Pitkow, P. E. Latham, and A. Pouget, "Information-limiting correlations," *Nature Neuroscience*, vol. 17, pp. 1410–1417, sep 2014.

[197] B. B. Averbeck, P. E. Latham, and A. Pouget, "Neural correlations, population coding and computation," *Nature Reviews Neuroscience*, vol. 7, pp. 358–366, may 2006.

[198] B. B. Averbeck and D. Lee, "Coding and transmission of information by neural ensembles," *Trends in Neurosciences*, vol. 27, pp. 225–230, apr 2004.

[199] M. R. Cohen and A. Kohn, "Measuring and interpreting neuronal correlations," *Nature Neuroscience*, vol. 14, pp. 811–819, jun 2011.

[200] B. J. Hansen, M. I. Chelaru, and V. Dragoi, "Correlated variability in laminar cortical circuits," *Neuron*, vol. 76, no. 3, pp. 590–602, 2012.

[201] A. Y. Y. Tan, Y. Chen, B. Scholl, E. Seidemann, and N. J. Priebe, "Sensory stimulation shifts visual cortex from synchronous to asynchronous states," *Nature*, vol. 509, pp. 226–229, mar 2014.

[202] J. De La Rocha, B. Doiron, E. Shea-Brown, K. Josić, and A. Reyes, "Correlation between neural spike trains increases with firing rate," *Nature*, vol. 448, pp. 802–806, aug 2007.

[203] D. P. Schulz, M. Sahani, and M. Carandini, "Five key factors determining pairwise correlations in visual cortex," *Journal of Neurophysiology*, vol. 114, no. 2, pp. 1022–1033, 2015.

[204] B. Haider and D. A. McCormick, "Rapid neocortical dynamics: cellular and network mechanisms," *Neuron*, vol. 62, no. 2, pp. 171–189, 2009.

[205] J. N. MacLean, B. O. Watson, G. B. Aaron, and R. Yuste, "Internal dynamics determine the cortical response to thalamic stimulation," *Neuron*, vol. 48, no. 5, pp. 811–823, 2005.

[206] A. Luczak, P. Barthó, and K. D. Harris, "Spontaneous events outline the realm of possible sensory responses in neocortical populations," *Neuron*, vol. 62, no. 3, pp. 413–425, 2009.

[207] S. Shoham, D. H. OConnor, and R. Segev, "How silent is the brain: is there a dark matter problem in neuroscience?," *Journal of Comparative Physiology A*, vol. 192, no. 8, pp. 777–784, 2006.

[208] J. Yu and D. Ferster, "Membrane potential synchrony in primary visual cortex during sensory stimulation," *Neuron*, vol. 68, pp. 1187–1201, dec 2010.

[209] M. Carandini, "Amplification of trial-to-trial response variability by neurons in visual cortex," *PLoS Biology*, vol. 2, no. 9, 2004.

[210] D. R. Lyamzin, S. J. Barnes, R. Donato, J. A. Garcia-Lazaro, T. Keck, and N. A. Lesica, "Nonlinear transfer of signal and noise correlations in cortical networks," *The Journal of Neuroscience*, vol. 35, no. 21, pp. 8065–8080, 2015.

[211] K. Mulligan and P. Ulinski, "Organization of geniculocortical projections in turtles: Isoazimuth lamellae in the visual cortex," *Journal of Comparative Neurology*, vol. 296, no. 4, pp. 531–547, 1990.

[212] H. Finger and P. König, "Phase synchrony facilitates binding and segmentation of natural images in a coupled neural oscillator network," *Correlated neuronal activity and its relationship to coding, dynamics and network architecture*, p. 44, 2014.

[213] D. L. Ringach, "Spontaneous and driven cortical activity: implications for computation," *Current opinion in Neurobiology*, vol. 19, no. 4, pp. 439–444, 2009.

[214] T. Tetzlaff, M. Helias, G. T. Einevoll, and M. Diesmann, "Decorrelation of neural-network activity by inhibitory feedback," *PLoS Comput Biol*, vol. 8, no. 8, p. e1002596, 2012.

[215] A. Bernacchia and X.-J. Wang, "Decorrelation by recurrent inhibition in heterogeneous neural circuits," *Neural Computation*, vol. 25, no. 7, pp. 1732–1767, 2013.

[216] Q. Wang, R. M. Webber, and G. B. Stanley, "Thalamic synchrony and the adaptive gating of information flow to cortex," *Nature Neuroscience*, vol. 13, no. 12, pp. 1534–1541, 2010.

[217] D. R. Ollerenshaw, H. J. Zheng, D. C. Millard, Q. Wang, and G. B. Stanley, "The adaptive trade-off between detection and discrimination in cortical representations and behavior," *Neuron*, vol. 81, no. 5, pp. 1152–1164, 2014.

[218] J. E. Heiss, Y. Katz, E. Ganmor, and I. Lampl, "Shift in the balance between excitation and inhibition during sensory adaptation of s1 neurons," *The Journal of Neuroscience*, vol. 28, no. 49, pp. 13320–13330, 2008.

[219] a. F. Bujan, A. Aertsen, and A. Kumar, "Role of input correlations in shaping the variability and noise correlations of evoked activity in the neocortex," *Journal of Neuroscience*, vol. 35, pp. 8611–8625, jun 2015.

[220] C. J. Whitmire, C. Waiblinger, C. Schwarz, and G. B. Stanley, "Information coding through adaptive gating of synchronized thalamic bursting," *Cell reports*, vol. 14, no. 4, pp. 795–807, 2016.

[221] D. A. Ruff and M. R. Cohen, "Attention can either increase or decrease spike count correlations in visual cortex," *Nature Neuroscience*, vol. 17, no. 11, pp. 1591–1597, 2014.

[222] M. R. Cohen and J. H. R. Maunsell, "Attention improves performance primarily by reducing interneuronal correlations," *Nature Neuroscience*, vol. 12, pp. 1594–1600, dec 2009.

[223] T. Crockett, N. Wright, S. Thornquist, M. Ariel, and R. Wessel, "Turtle dorsal cortex pyramidal neurons comprise two distinct cell types with indistinguishable visual responses," *PloS one*, vol. 10, no. 12, p. e0144012, 2015.

[224] D. Saha, D. Morton, M. Ariel, and R. Wessel, "Response properties of visual neurons in the turtle nucleus isthmi," *Journal of Comparative Physiology A*, vol. 197, no. 2, pp. 153–165, 2011.

[225] W. L. Shew, W. P. Clawson, J. Pobst, Y. Karimipanah, N. C. Wright, and R. Wessel, "Adaptation to sensory input tunes visual cortex to criticality," *Nature Physics*, vol. 11, no. 8, pp. 659–663, 2015.

[226] D. M. Senseman and K. A. Robbins, "High-speed vsd imaging of visually evoked cortical waves: decomposition into intra-and intercortical wave motions," *Journal of Neurophysiology*, vol. 87, no. 3, pp. 1499–1514, 2002.

[227] D. M. Senseman, "Spatiotemporal structure of depolarization spread in cortical pyramidal cell populations evoked by diffuse retinal light flashes.," *Visual neuroscience*, vol. 16, no. 1, pp. 65–79, 1999.

[228] D. J. Watts and S. H. Strogatz, "Collective dynamics of 'small-world' networks.," *Nature*, vol. 393, pp. 440–2, jun 1998.

[229] A. Mazzoni, S. Panzeri, N. K. Logothetis, and N. Brunel, "Encoding of naturalistic stimuli by local field potential spectra in networks of excitatory and inhibitory neurons.," *PLoS computational biology*, vol. 4, p. e1000239, dec 2008.

[230] G. Buzsaki, *Rhythms of the Brain*. Oxford University Press, 2006.

[231] P. L. Marchiafava, "An antagonistic surround facilitates central responses by retinal ganglion cells," *Vision Research*, vol. 23, no. 10, pp. 1097–1099, 1983.

[232] L. Larson-Prior, P. Ulinski, and N. Slater, "Excitatory amino acid receptor-mediated transmission in geniculocortical and intracortical pathways within visual cortex," *Journal of Neurophysiology*, vol. 66, no. 1, pp. 293–306, 1991.

[233] I. Oren, E. O. Mann, O. Paulsen, and N. Hájos, "Synaptic currents in anatomically identified ca3 neurons during hippocampal gamma oscillations in vitro," *The Journal of Neuroscience*, vol. 26, no. 39, pp. 9923–9934, 2006.

[234] A. Hasenstaub, Y. Shu, B. Haider, U. Kraushaar, A. Duque, and D. a. McCormick, "Inhibitory postsynaptic potentials carry synchronized frequency information in active cortical networks.," *Neuron*, vol. 47, pp. 423–35, aug 2005.

[235] D. J. Tolhurst, J. A. Movshon, and A. F. Dean, "The statistical reliability of signals in single neurons in cat and monkey visual cortex," *Vision Research*, vol. 23, no. 8, pp. 775–785, 1983.

[236] R. Vogels, W. Spileers, and G. A. Orban, "The response variability of striate cortical neurons in the behaving monkey," *Experimental brain research*, vol. 77, no. 2, pp. 432–436, 1989.

[237] Z. F. Mainen and T. J. Sejnowski, "Reliability of spike timing in neocortical neurons," *Science*, vol. 268, no. 5216, p. 1503, 1995.

[238] M. N. Shadlen and W. T. Newsome, "The variable discharge of cortical neurons: implications for connectivity, computation, and information coding," *The Journal of Neuroscience*, vol. 18, no. 10, pp. 3870–3896, 1998.

[239] W. Maass and P. Orponen, "On the effect of analog noise in discrete-time analog computations," *Neural Computation*, vol. 10, no. 5, pp. 1071–1095, 1998.

[240] S. Dakin and U. Frith, "Vagaries of visual perception in autism," *Neuron*, vol. 48, no. 3, pp. 497–507, 2005.

[241] S. Sadagopan and D. Ferster, "Feedforward origins of response variability underlying contrast invariant orientation tuning in cat visual cortex," *Neuron*, vol. 74, no. 5, pp. 911–923, 2012.

[242] N. J. Priebe and D. Ferster, "Mechanisms of neuronal computation in mammalian visual cortex," *Neuron*, vol. 75, no. 2, pp. 194–208, 2012.

[243] R. L. Goris, J. A. Movshon, and E. P. Simoncelli, "Partitioning neuronal variability," *Nature Neuroscience*, vol. 17, no. 6, pp. 858–865, 2014.

[244] A. A. Faisal, L. P. Selen, and D. M. Wolpert, "Noise in the nervous system," *Nature Reviews Neuroscience*, vol. 9, no. 4, pp. 292–303, 2008.

[245] R. C. Kelly, M. A. Smith, R. E. Kass, and T. S. Lee, "Local field potentials indicate network state and account for neuronal response variability," *Journal of Computational Neuroscience*, vol. 29, no. 3, pp. 567–579, 2010.

[246] A. S. Ecker and A. S. Tolias, "Is there signal in the noise?," *Nature Neuroscience*, vol. 17, pp. 750–751, may 2014.

[247] C. Curto, S. Sakata, S. Marguet, V. Itskov, and K. D. Harris, "A simple model of cortical dynamics explains variability and state dependence of sensory responses in urethane-anesthetized auditory cortex," *Journal of Neuroscience*, vol. 29, pp. 10600–10612, aug 2009.

[248] K. D. Harris and A. Thiele, "Cortical state and attention," *Nature Reviews Neuroscience*, vol. 12, pp. 509–523, aug 2011.

[249] A. Kohn, A. Zandvakili, and M. a. Smith, "Correlations and brain states: from electrophysiology to functional imaging," *Current Opinion in Neurobiology*, vol. 19, pp. 434–438, aug 2009.

[250] M. Y. Byron, J. P. Cunningham, G. Santhanam, S. I. Ryu, K. V. Shenoy, and M. Sahani, "Gaussian-process factor analysis for low-dimensional single-trial analysis of neural population activity," in *Advances in neural information processing systems*, pp. 1881–1888, 2009.

[251] E. Salinas and T. J. Sejnowski, "Impact of correlated synaptic input on output firing rate and variability in simple neuronal models," *The Journal of Neuroscience*, vol. 20, no. 16, pp. 6193–6209, 2000.

[252] R. J. Rosenbaum, "Pooling and correlated neural activity," *Frontiers in Computational Neuroscience*, vol. 4, p. 9, jan 2010.

[253] K. Briggman and W. Kristan Jr, "Multifunctional pattern-generating circuits," *Annu. Rev. Neurosci.*, vol. 31, pp. 271–294, 2008.

[254] G. Deco and V. K. Jirsa, "Ongoing cortical activity at rest: criticality, multistability, and ghost attractors," *The Journal of Neuroscience*, vol. 32, no. 10, pp. 3366–3375, 2012.

[255] L. Cossell, M. F. Iacaruso, D. R. Muir, R. Houlton, E. N. Sader, H. Ko, S. B. Hofer, and T. D. Mrsic-Flogel, "Functional organization of excitatory synaptic strength in primary visual cortex," *Nature*, vol. 518, pp. 399–403, feb 2015.

[256] M. A. Smith and A. Kohn, "Spatial and temporal scales of neuronal correlation in primary visual cortex," *The Journal of Neuroscience*, vol. 28, no. 48, pp. 12591–12603, 2008.

[257] D. a. Gutnisky and V. Dragoi, "Adaptive coding of visual information in neural populations," *Nature*, vol. 452, pp. 220–224, mar 2008.

[258] J. L. Herrero, M. A. Gieselmann, M. Sanayei, and A. Thiele, "Attention-induced variance and noise correlation reduction in macaque v1 is mediated by nmda receptors," *Neuron*, vol. 78, no. 4, pp. 729–739, 2013.

[259] A. S. Ecker, P. Berens, G. A. Keliris, M. Bethge, N. K. Logothetis, and A. S. Tolias, "Decorrelated neuronal firing in cortical microcircuits," *science*, vol. 327, no. 5965, pp. 584–587, 2010.

[260] A. Kohn, "Stimulus dependence of neuronal correlation in primary visual cortex of the macaque," *Journal of Neuroscience*, vol. 25, pp. 3661–3673, apr 2005.

[261] R. Levi, P. Varona, Y. I. Arshavsky, M. I. Rabinovich, and A. I. Selverston, "The role of sensory network dynamics in generating a motor program," *The Journal of Neuroscience*, vol. 25, no. 42, pp. 9807–9815, 2005.

[262] O. Mazor and G. Laurent, "Transient dynamics versus fixed points in odor representations by locust antennal lobe projection neurons," *Neuron*, vol. 48, no. 4, pp. 661–673, 2005.

[263] R. M. Haefner and B. G. Cumming, "An improved estimator of variance explained in the presence of noise," in *Advances in neural information processing systems*, pp. 585–592, 2009.

[264] S. V. David and J. L. Gallant, "Predicting neuronal responses during natural vision," *Network: Computation in Neural Systems*, vol. 16, no. 2-3, pp. 239–260, 2005.

[265] G. T. Einevoll, C. Kayser, N. K. Logothetis, and S. Panzeri, "Modelling and analysis of local field potentials for studying the function of cortical circuits," *Nature Reviews Neuroscience*, vol. 14, no. 11, pp. 770–785, 2013.

[266] U. Mitzdorf, "Properties of the evoked potential generators: current source-density analysis of visually evoked potentials in the cat cortex," *International Journal of Neuroscience*, vol. 33, no. 1-2, pp. 33–59, 1987.

[267] E. Juergens, A. Guettler, and R. Eckhorn, "Visual stimulation elicits locked and induced gamma oscillations in monkey intracortical-and eeg-potentials, but not in human eeg," *Experimental Brain Research*, vol. 129, no. 2, pp. 247–259, 1999.

[268] G. Buzsáki and A. Kandel, "Somadendritic backpropagation of action potentials in cortical pyramidal cells of the awake rat," *Journal of Neurophysiology*, vol. 79, no. 3, pp. 1587–1591, 1998.

[269] G. Buzsáki, "Theta oscillations in the hippocampus," *Neuron*, vol. 33, no. 3, pp. 325–340, 2002.

[270] A. Kamondi, L. Acsády, X.-J. Wang, and G. Buzsáki, "Theta oscillations in somata and dendrites of hippocampal pyramidal cells in vivo: Activity-dependent phase-precession of action potentials," *Hippocampus*, vol. 8, no. 3, pp. 244–261, 1998.

[271] C. Kayser and P. König, "Stimulus locking and feature selectivity prevail in complementary frequency ranges of v1 local field potentials," *European Journal of Neuroscience*, vol. 19, no. 2, pp. 485–489, 2004.

[272] J. Liu and W. T. Newsome, "Local field potential in cortical area mt: stimulus tuning and behavioral correlations.," *Journal of Neuroscience*, vol. 26, pp. 7779–90, jul 2006.

[273] E. Başar, *EEG-brain dynamics: relation between EEG and brain evoked potentials*. Elsevier-North-Holland Biomedical Press, 1980.

[274] M. Steriade, "Alertness, quiet sleep, dreaming," in *Normal and Altered States of Function*, pp. 279–357, Springer, 1991.

[275] A. Belitski, A. Gretton, C. Magri, Y. Murayama, M. a. Montemurro, N. K. Logothetis, and S. Panzeri, "Low-frequency local field potentials and spikes in primary visual cortex convey independent visual information," *Journal of Neuroscience*, vol. 28, pp. 5696–5709, may 2008.

[276] D. Percival and A. Walden, "Spectral analysis for physical applications: multitaper and conventional univariate techniques, 583 pp," *Cambridge Univ. Press, New York*, 1993.

[277] S. P. Strong, R. Koberle, R. R. d. R. van Steveninck, and W. Bialek, "Entropy and information in neural spike trains," *Physical Review Letters*, vol. 80, no. 1, p. 197, 1998.

[278] C. Haldeman and J. M. Beggs, "Critical branching captures activity in living neural networks and maximizes the number of metastable states," *Physical Review Letters*, vol. 94, no. 5, p. 058101, 2005.

[279] W. L. Shew, H. Yang, S. Yu, R. Roy, and D. Plenz, "Information capacity and transmission are maximized in balanced cortical networks with neuronal avalanches," *The Journal of Neuroscience*, vol. 31, no. 1, pp. 55–63, 2011.

[280] D. L. Gilden, "Cognitive emissions of 1/f noise.," *Psychological review*, vol. 108, no. 1, p. 33, 2001.

[281] J. M. Beggs and D. Plenz, "Neuronal avalanches in neocortical circuits," *The Journal of Neuroscience*, vol. 23, no. 35, pp. 11167–11177, 2003.

[282] T. Petermann, T. C. Thiagarajan, M. A. Lebedev, M. A. Nicolelis, D. R. Chialvo, and D. Plenz, "Spontaneous cortical activity in awake monkeys composed of neuronal avalanches," *Proceedings of the National Academy of Sciences*, vol. 106, no. 37, pp. 15921–15926, 2009.

Vita

Mahmood Hoseini

RESEARCH INTERESTS

My research has been mostly focused on modeling coordinated activity and data analysis of intra- and extracellular recordings from the perspective of oscillations. The highlights of my study are: i) gamma band oscillations modulate coordination, and ii) how does network architecture play a role in neural coordination. My future goal is to uncover how oscillations and coordinated activity work together in information processing in the brain.

EDUCATION

Doctor of Philosophy, **Neurophysics, Neuroscience** **2011-Present**
Washington University in St. Louis (wustl), Saint Louis, MO 63130,USA
Thesis: *The Dynamic Brain in Action: Cortical Oscillations and Coordination Dynamics*
Advisors: Prof. Ralf Wessel

Master of Science, **Physics, Complex systems** **2008**
Sharif University of Technology (SUT), Tehran, Iran
Thesis: *Time-frequency analysis of epileptic patients EEG*
Advisors: Prof. Mohammad Reza Rahimi Tabar

Bachelor of Science, **Physics** **2008**
Isfahan University, Isfahan, Iran

HONORS AND AWARDS

- University Fellowship, Washington University in St. Louis **2012**
- Summer Hughes Fellowship, Physics Department, wustl **2012**
- M.Sc Fellowship, Sharif University of Technology, **2008-2010**
- Ranked **20**th in national entrance exam among ≈10,000 participants **2008**

- Ranked **8**th in 13th National Olympiad in Physics **2008**

SKILLS AND EXPERTISE

- Programming Languages & Softwares : C/C++, Python, MATLAB, NEURON, R, Code Skulpter
- Experimental Methods: Electrophysiology
- Computational Methods : Molecular Dynamics, Wavelet, Monte Carlo, GPU parallelization
- Experienced with using information theoretic measures, statistics and machine learning

PUBLICATIONS

- Nathaniel Wright, **Mahmood S. Hoseini**, Ralf Wessel. *Adaptation reduces the correlated variability of cortical membrane potential visual responses*. In preparation.
- **Mahmood S. Hoseini**, Nathaniel Wright, Jeff Pobst, Wesley Clawson, Woodrow Shew, Ralf Wessel. *State-dependent variability in local field potentials*. In preparation.
- **Mahmood S. Hoseini**, Jeff Pobst, Nathaniel Wright, Wesley Clawson, Woodrow Shew, Ralf Wessel. *Stimulus-induced oscillations are variable in duration and frequency but still coherent in visual cortex*. In preparation.
- **Mahmood S. Hoseini**, Ralf Wessel (2016). *Coherent and intermittent ensemble oscillations emerge from networks of irregular spiking neurons*. Journal of neurophysiology 115.1: 457-469.

PRESENTATIONS
INVITED TALKS

- *Network structure and temporal coordination dynamics in primary visual cortex*, Department of Neuroscience, University of California, San Fransisco **June 2016**

- *Network structure and temporal coordination dynamics in primary visual cortex*, Department of cellular and molecular biology, Harvard University **July 2016**
- *Coherent and intermittent ensemble oscillations emerge from networks of irregular spiking neurons*, Research Center of Theoretical Physics & Mathematics, Tehran **July 2016**

ORAL PRESENTATIONS

- *Coherent and intermittent ensemble oscillations emerge from networks of irregular spiking neurons*, Graduate Seminar, wustl **March 2015**

POSTER PRESENTATIONS

- **Mahmood S. Hoseini**, Nathaniel Wright, Wesley Clawson, Woodrow Shew, Ralf Wessel. *A model network with clustered connections reproduces the observed dynamics of correlated variability in visual cortex*. SfN 2016, San Diego (Nov. 2016).
- Nathaniel Wright, **Mahmood S. Hoseini**, Ralf Wessel. *Dynamics of "population coupling" between synaptic inputs and local cortical activity during visual processing*. SfN 2016, San Diego (Nov. 2016).
- James K. Johnson, Nathaniel Wright, **Mahmood S. Hoseini**, Ralf Wessel. *Evaluating network criticality with membrane potentials*. SfN 2016, San Diego (Nov. 2016).
- **Mahmood S. Hoseini**, Jeff Pobst, Wesley Clawson, Woodrow Shew, Ralf Wessel. *Intermittent ensemble oscillations emerge dynamically from cortical circuits of irregular spiking neurons*. SfN 2015, Chicago (Nov. 2015).
- Nathaniel Wright, **Mahmood S. Hoseini**, Jeff Pobst, Wesley Clawson, Woodrow Shew, Ralf Wessel. *Dynamics of cortical noise correlation during vision*. SfN 2015, Chicago (Nov. 2015).
- **Mahmood S. Hoseini**, Jeff Pobst, Wesley Clawson, Woodrow Shew, Ralf Wessel. *Characterization an proposed mechanisms of intermittent oscillations in cerebral cortex*. SAND7 2015, Pittsburgh, US (May 2015).

- **Mahmood S. Hoseini**, Jeff Pobst, Wesley Clawson, Woodrow Shew, Ralf Wessel. *Characterization and proposed mechanisms of intermittent oscillations in cerebral cortex*. SfN 2014, Washington DC (Nov. 2014).
- Nathaniel Wright, **Mahmood S. Hoseini**, Thomas Crockett, Jeff Pobst, Wesley Clawson, Woodrow Shew, Ralf Wessel. *Dynamics of cortical correlation during visual processing*. SfN 2014, Washington DC (Nov. 2014).
- **Mahmood S. Hoseini**, Jeff Pobst, Wesley Clawson, Woodrow Shew, Ralf Wessel. *Characterization and proposed mechanisms of intermittent oscillations in cerebral cortex*. Annual Neuroscience Retreat, Grafton, IL (Sept. 2014).

RESEARCH RELATED EXPERINECE

- **M.Sc. Thesis** **SUT 08/09 - 12/10**
  analyzed electrocorticogram (ECG) data from 21 epileptic patients to determine transition in PDF using a method originally developed for complex hierarchical system analysis. Determined the conduction velocity for neural impulses using cross correlation function and synchronization patterns. Evaluated information content of signals to find most informative frequency bands during seizure.
  Advisor: Prof. M. R. RahimiTabar
- **Time Series Workshop** **SUT 07/10**
  Involved in signal processing techniques for detrending and predicting the behavior of a noisy signal, worked with signal processing toolbox in MATLAB®, developed a neural network to distinguish different digits.
- **Lectures in Lipid and Membrane** **SUT 08/09 - 12/09**
  Ref : Biomembrane Frontiers: Nanostructures, Models, and the Design of Life, Roland Faller, volume2, Springer 2009
  Instructor: Prof. M. R. RahimiTabar
- **Lectures in Quantum Molecular Dynamics** **SUT 08/10 - 12/10**
  Ref : Theory and Application of Quantum Molecular Dynamics, John Z. H. Zhang, World scientific publishing co.1999 Instructor : Prof. M. R. RahimiTabar

TEACHING EXPERIENCE

- Undergraduate Mechanics TA, Physics department, WUSTL **Spring 2016**

- Non-linear dynamical systems TA, Physics department, WUSTL **Fall 2015**
- Adv Math Methods for Physicists&Engineers II TA, Physics department, WUSTL **Spring 2015**
- Intro physics lab TA, Physics department, WUSTL **Fall 2012 & Spring 2013**
- Intro physics I and quantum mechanics I instructor, Payam Noor University, Boroujen, Iran **Fall 2011**
- Intro physics I TA, Physics department, Sharif University of Technology, Tehran, Iran **Fall 2010**
- Middle school project supervisor, Omid school, Isfahan, Iran **2006 - 2008**
- Electromagnetism I TA, Physics department, Isfahan University, Isfahan, Iran **Fall 2007**

PROFESSIONAL SOCIETY MEMBERSHIPS

- Society for Neuroscience
- American Physical Society

REFERENCES

- Ralf Wessel, Washington University in St. Louis
  Phone: (314) 935-7765, Email: rw@physics.wustl.edu
- Woodrow Shew, University of Arkansas
  Phone: (479) 575-5693, Email: shew@uark.edu
- Anders Carlsson, Washington University in Saint Louis
  Phone: (314) 935-5739, Email: aec@physics.wustl.edu
- Mohammad Reza Rahimi Tabar, Carl-von-Ossietzky University
  Phone: +49-15110374155, Email: mohammed.r.rahimi.tabar@uni-oldenburg.de